Mechanical and Functional Study of Cell Physiology at the Nanoscale

THÈSE N^{O} 6999 (2016)

PRÉSENTÉE LE 7 SEPTEMBRE 2016

À LA FACULTÉ DES SCIENCES ET TECHNIQUES DE L'INGÉNIEUR
LABORATOIRE DE BIO- ET NANO-INSTRUMENTATION
PROGRAMME DOCTORAL EN BIOTECHNOLOGIE ET GÉNIE BIOLOGIQUE

ÉCOLE POLYTECHNIQUE FÉDÉRALE DE LAUSANNE

POUR L'OBTENTION DU GRADE DE DOCTEUR ÈS SCIENCES

PAR

Pascal Damian ODERMATT

acceptée sur proposition du jury:

Prof. A. Radenovic, présidente du jury
Prof. G. Fantner, directeur de thèse
Dr R. Jungmann, rapporteur
Dr P.-E. Milhiet, rapporteur
Prof. J. McKinney, rapporteur

ÉCOLE POLYTECHNIQUE
FÉDÉRALE DE LAUSANNE

Suisse
2016

Acknowledgements

A very eventful time and project is coming to an end. Scientifically as well as personally, many challenges were waiting for me. Seeing how much everything changed during the time I was here, makes me feel that it is the right time to submit this work. Not only my hair gets apparently a little greyer, the lab was growing up as well. Projects started from scratch turned into fantastic technological and scientific advancements. I am truly happy that I could work in this lab at this school. Such interdisciplinary, such fantastic collaborators, such inspiring ideas and people everywhere! To be among them taught me how to tackle challenges, how to think further, how to ask and how to answer scientific questions.

First I want to thank my wonderful dear love and soulmate Silvia and all my family. Spending time with the most important people in my life always helped me shift the focus away from work and instead shift it towards a lot of fun moments and fantastic memories. Your unstoppable love, affection, and support helped me enormously and reinforced my feeling that I was doing the right thing at all times!

To put my focus back to work wasn't difficult either. I am very lucky to have had the opportunity and the trust to participate in such amazing projects. I turned from a data gatherer into a critically thinking scientist. And the main person to indicate the right directions was Georg Fantner. A great mind always on the go, always new ideas, new projects, who not only made sure my work was done, but was never forgetting the human being behind a person. I am very grateful not only for what you helped me achieve scientifically (thanks to a lot of advice, patience, trust and hope on your side into my work), but for your sympathy and support during the periods I needed time off-work!

Then I'd like to thank Aleksandra Radenović and John McKinney, who are both enormously passionate scientists in a positively contagious way with infectious ideas and inspirations. It was truly a great experience to collaborate with you!

Special thanks go to Dr. Pierre-Emmanuel Milhiet and Dr. Ralf Jungmann who generously agreed to be on the jury of the private defence. Thank you!

I was very warmly welcomed by Jonathan Adams and Blake Erickson from the first day I started in the lab. Besides all their scientific advice Jonathan taught me that not all the problems can be solved by yesterday, while Blake showed me that many baby steps con go a long way. Many thanks!

My thanks go to all the people in the lab! Everyone was helping me out whenever I asked for something and needed to discuss some experiments. More than that thank you for sharing meetings, beers, lunchtimes, experimental failures, experimental success, coffee, skiing days, lab

dinners, barbeque and so on. Namely Maja Đukić Pjanić, Oliver Peric, Nahid Hosseini, Adrian Nievergelt, Alex Eskandarian, Soma Biswas, Tamina Sissoko, Ruth Fiaux, Joëlle Ven, Chen Yang, Mélanie Hannebelle, Santiago Andany, and many of the people who frequented our lab. You are the heart and the soul of this a vibrant lab!

Lastly, to all my collaborators who came with fantastically crazy ideas or whom I could go to ask a favor. This includes Hendrik Deschout, Arun Shivanandan, Craig Nowell and Paolo Jacob, as well as the BIOP and the mechanical workshop and many others.

Thank you all!

Pascal Odermatt

Lausanne, 04 April 2016

Zusammenfassung

Live-Cell-Imaging biologischer Proben kann dynamische zelluläre Prozesse auflösen. Fluoreszenzmikroskopie (FM) sowie Rasterkraftmikroskopie (AFM) sind beide in der Lage lebende Zellen abzubilden. Durch Kombination dieser Techniken können strukturelle als auch funktionelle Informationen derselben biologischen Probe gemessen werden. Während die Dynamik von spezifischen Proteinen durch FM abgebildet wird, liefert das AFM den strukturellen Kontext. Um zu untersuchen, wie intrazelluläre Prozesse die Mechanik, Struktur und Kinetik biologischer Zellen im Nanobereich beeinflussen, kombinierten wir ein hochgeschwindigkeits-AFM (HS-AFM) mit einem invertiertem Mikroskop (OM) in ein Gerät. Mit diesem System werden zellphysiologische Prozesse auf unterschiedlichen Zeitskalen abgebildet. Migration von Säugetierzellen innerhalb von Minuten wird beobachtet mittles korrelierter superauflösender Mikroskopie und HS-AFM. Bakterielle Zellteilung innerhalb von wenigen Millisekunden als auch das Bakterienwachstum über mehrere Generationen hinweg wird untersucht. Ausserdem wird auch die Möglichkeit des AFM zur quantitativen Messung mechanischer Eigenschaften von Geweben in Kombination mit FM auf Augenhornhautgewebe von Mäusen genutzt.

Im Unterschied zu den meisten anderen stäbchenförmige Bakterien bei denen Zellteilung durch Verengung der Zellwand in der Zellmitte erfolgt, bleibt die Form der äußeren Zellhülle bei Mykobakterien unverändert. Die Scheidewand wird durch Abzweigen von Peptidoglykan von der äußeren Zellhülle gebildet, welche die Zelle in zwei Schwesternkammern aufteilt. Nano-Messungen zeigen, daß nach dem Beginn der Septierung die Steifigkeit am Septum signifikant ansteigt. Zeitlich hoch aufgelöste Messungen der folgenden bakteriellen Zellteilung zeigte, dass sich die Geschwisterzellen innerhalb weniger Millisekunden trennen. Die Verbindung der äußeren Zellhülle am Septum reisst auseinander was auf einen mechanische Bruch hinweist. Der Zeitpunkt der Zelltrennung wird durch die Zugspannung am Septum und der Reißfestigkeit des Zellwandmaterials reguliert.

Die Stellen, an denen diese Trennungen auftreten, sind eng mit morphologischen Merkmalen auf der wellenförmigen Zelloberfläche assoziiert. Diese Merkmale werden an den Zellpolen gebildet und wandern in Richtung Zellmitte während die Zelle wächst. Interessanterweise, kommen Zellteilungen nur im zentralsten Wellentrog vor, womit diese Merkmale die ersten morphologischen Hinweise auf eine örtlich definierte Zellteilung sind. Experimente mit mutanten Bakterien zeigen, dass auch asymmetrische Zellteilungen in Wellentälern passieren, was die Wichtigkeit ihrer Rolle in der Auswahl der Zellteilungsposition unterstreicht.

Eine chronische Entzündung kann eine Erhöhung der Steifigkeit des Augenhornhautgewebes auslösen, welche gleichzeitig mit drastischen Veränderungen in der Zusammensetzung des Gewebes einhergeht. Migration von Stammzellen entlang dieser Gewebeschicht erhöhter Steifigkeit löst eine erhöhte Aktivierung von Mechanotransduktion Kaskaden aus. Dies führt

schließlich zu einem hautähnlichen, anstatt einem kornea-artigen Charakter dieser regenrativen Stammzellen. Es zeigt sich, dass die Steifigkeit des Gewebes und damit Mechanotransduktion Kaskaden entscheidend an der Differenzierung von Stammzellen beteiligt sind.

Stichwörter

Rasterkraftmikroskopie, Einzelmolekül-Lokalisationsmikroskopie, Live-Cell-Imaging, bakterielle Zellteilung, Mykobakterien, nanomechanische Charakterisierung, Stammzelldifferenzierung, chronische Entzündung, korreliert Mikroskopie, Hochgeschwindigkeits-AFM, Mechanotransduktion, Mechanobiologie

Abstract

By live-cell imaging of biological samples dynamic cellular processes can be resolved. Fluorescence microscopy (FM) and atomic force microscopy (AFM) are both capable of imaging live cells. By combining these techniques structural as well as functional information of the same biological samples are measured. While the dynamics of specific proteins can be imaged by FM, the AFM provides the structural context. To study how intracellular processes affect the mechanics, structure and kinetics of cells at the nanoscale we combined a high-speed AFM (HS-AFM) and an inverted optical microscope (OM) into one instrument. With this system cell physiological processes at different time scales are imaged. Mammalian cell migration happening at minute time scales is studied by correlated super-resolution microscopy and HS-AFM. Bacterial cell separation happening within 10s of milliseconds is characterized as well as bacterial growth over multiple generations. Additionally to imaging, the capability of the AFM to quantitatively measure mechanical properties of tissues is deployed in combination with FM on mouse corneal tissues.

Different to most other rod-shaped bacteria where division happens through constriction of the cell wall at midcell, *mycobacteria* keep the shape of their outer cell envelope unchanged during septation. The septal wall is formed by peptidoglycan branching off from the outer cell envelop eventually splitting the cell into two sister compartments. Nanomechanical measurements show that from the initiation of septation the stiffness at the septum increases significantly. High-temporal resolution imaging of the following bacterial separation process indicated that the sibling cells separate within tens of milliseconds. The connection of the outer cell envelop at the former septum is broken apart suggesting a mechanical break. The timing of the cell separation is regulated by the tensile stress at the septum and the ultimate tensile strength of the cell wall material.

The positions where these separations occur are closely associated with morphological features on the undulating cell surface. These features are formed at the poles and migrate towards midcell as the cell grows. Interestingly, sibling cell separation is restricted to the center-most wave-trough making these features the first characteristic associated with division site placement. Experiments with mutant strains show that even asymmetric divisions occur within wave-troughs emphasizing their role in division site placement.

Chronic inflammation induces an increase in the stiffness of the corneal tissue and is associated with dramatic changes in the composition of the tissue. Stem cells migrating along this tissue layer of increased stiffness experience increased activation of mechanotransduction pathways. This eventually leads to induction of a skin-like rather than corneal-like character of these regenerating stem cells. It demonstrates that the stiffness of the tissue and thus pathways involved in mechanotransduction decisively influence the stem cell fate.

Keywords

Atomic force microscopy, Single molecule localization microscopy, live-cell imaging, bacterial cell division, mycobacteria, nanomechanical characterization, stem cell differentiation, chronic inflammation, correlated microscopy, high-speed AFM, mechanotransduction, mechanobiology

Contents

List of Figures

Chapter 1 Introduction

1.1 Atomic Force Microscopy

The atomic force microscope (AFM) invented by Binnig, Quate and Gerber in 1986(*1*) is a very versatile instrument used in various biological research fields. It works inherently different to other microscopes traditionally used in biological research. Instead of light that is interacting with the sample such as in optical microscopes, the AFM can "feel" the surface. A very sharp needle with a nanometer size tip attached to a cantilever moves across the surface in a raster-scanning mode, covering every point of the sample one by one. As the needle tracks the surface at each point it adapts to height changes and follows the topography of the sample. Nanometer height changes are recorded and at the end a 3 dimensional topographical structure of the surface is provided. A schematic of the central parts of the AFM is given in Figure 1.1. It includes a probe that scans over the surface, a scanner that moves the probe accurately across the surface and a system to detect the deflection of the probe as it is in contact with the surface.

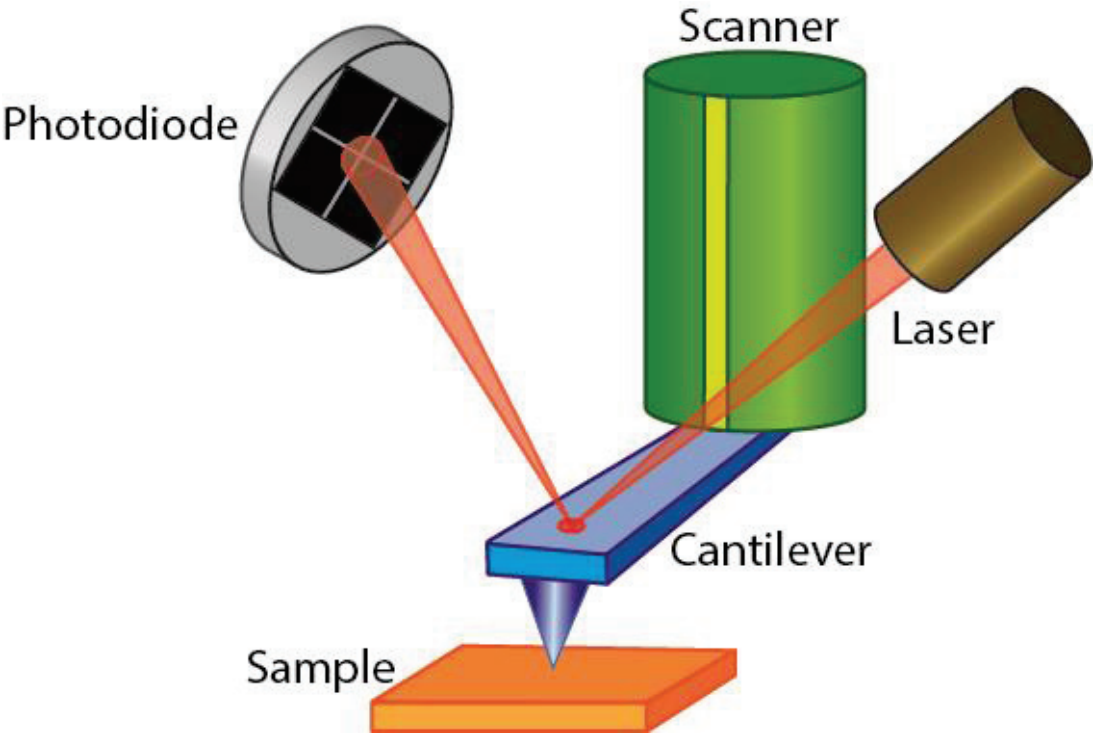

Figure 1.1 Principle of AFM. The tip at the front of the cantilever is scanned over the surface in raster-scanning mode by the motion of the scanner. A laser beam reflected off from the backside of the cantilever is detected by the photodiode. Small changes of the topography during scanning of the sample will change the deflection of the cantilever and in consequence the angle of the reflected laser beam. This in

turn changes the position of the incident laser beam on the photodiode and can then be correlated to the change in topography of the sample. The position of the cantilever can then be determined and adjusted.

The tip at the front of the cantilever is in contact with the surface such that the cantilever that acts like a spring is slightly deflected. This ensures that the tip stays in contact with the surface as it is scanned across the surface. The piezo tube is the part that moves the cantilever over the surface. As the tip is scanned over the surface and comes across a feature on the surface that is higher the cantilever would deflect more. In contrast, if there is a hole in the surface, the tip would follow it and the cantilever would deflect less. As the deflection changes according to height changes on the surface the laser beam which is reflected off the backside of the cantilever changes its angle. This changes the position at which the laser beam hits the photodiode. Therefore, by determining the position of the laserspot on the photodiode changes of the deflection can be measured which in turn reflects the changes of height on the sample surface. Besides this imaging mode where the cantilever is kept at a constant height from the surface and the deflection is directly related to changes in height, different imaging modes have emerged. In contact mode the cantilever is as well in contact with surface but the deflection rather than the height is kept constant. In this case, if there is a hole in the surface and the deflection decreases, the cantilever is moved down regulated by a feedback loop to keep the deflection constant. Thereby the movements in z direction of the cantilever as it scans the surface reflect the topography of the sample. Another popular imaging mode is called tapping mode. Different to the previous two imaging modes, in tapping mode the cantilever is oscillating close to its resonance frequency at a free amplitude specified by the user. As the cantilever approaches the surface the cantilever experiences repulsive forces and the amplitude decreases. As soon as the cantilever is close enough to the surface such that the amplitude decreased to a value set by the user the AFM starts scanning. As the height of the sample changes up and down the amplitude will change since the repulsive force will either become higher or lower. Therefore by moving the cantilever up and down, as before in the contact mode, the amplitude is kept constant regulated by a feedback loop. Here again, the up and down movements of the cantilever required to keep the amplitude constant reflect the topography of the sample. Tapping mode imaging has the advantage of being only intermittently in contact with the tip reducing the tip-sample interaction. Independent of the imaging mode, standard AFMs can measure height differences of 1 nm (about 100’000x smaller than the diameter of a human hair) and typically scan an area equal to the crossection of a human hair (100 µm x 100 µm).

Besides the high resolution the AFM can achieve, the possibility of imaging samples in fluid makes this instrument very powerful for biological research. Biomolecules, live bacteria or mammalian cells can be observed in buffer solutions that mimic physiological conditions. Biological samples however are often very fragile and it is imperative to avoid introducing damage during scanning. Therefore, the force exerted on the sample by the tip should be reduced to a minimum. Excellent force control is required for live biological samples. Recently, a scanning mode was developed that enables force control in the range of 10s of piconewtons. In this mode the cantilever is moved up and down sinusoidally, typically at a frequency between 1 - 8 kHz, instead of being dragged along in contact with the surface. During the entire sinusoidal cycle the deflection of the cantilever is recorded (Figure 1.2) as it touches the surface. If the cantilever is calibrated appropriately (i.e. spring constant and deflection sensitivity are known) the degree of

deflection can be correlated directly to a force exerted on the surface. Therefore, at each position of the sinusoidal cycle the force can be estimated by the amount of deflection.

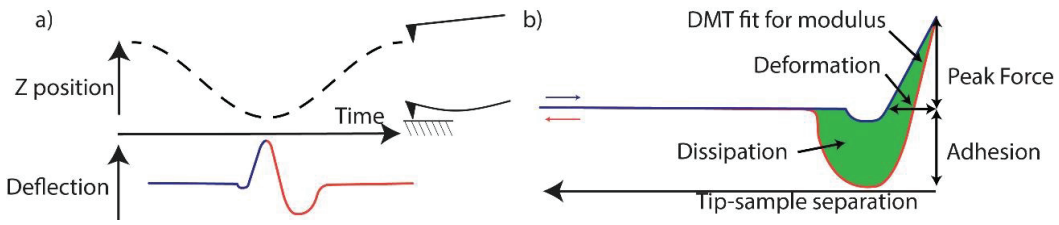

Figure 1.2 Schematic of PeakForce™ Quantitative Nanomechanical Measurement (QNM™) mode. a) The cantilever is actuated sinusoidally up and down. At each point in z the deflection can be measured in real-time, known as force-distance curves. The blue trace indicates the deflection as the cantilever is moving towards the sample. Red indicates the deflection on the retraction. b) Different regions of the force-distance curves can then be used to infer material properties of the sample.

As the cantilever approaches the surface often a snap-in to contact with the surface is observed due to attractive forces, before it starts to deflect (indicated by the dip in the approach curve (blue)). As the the cantilever moves down further the deflection, and thus the force, increases till it reaches its position closest to the sample. Then the cantilever will retract from the surface and the deflection decreases again. Now that it is known how much the peak force was, that was applied on the sample during this cycle the distance between the cantilever and the sample can be readjusted for the next cycle to match the peak force exerted on the sample to a value specified by the user. From these force-distance curves different parameters about the sample can be extracted, including the DMT modulus, deformation, adhesion or dissipation. The excellent force control, the quantitative measurements of mechanical properties, the robustness of the imaging mode as well as the reasonable speed at which these measurements can be taken make it a very convenient scanning mode for biological samples.

1.2 Diffraction Limit of Optical Microscopes and Super Resolution Techniques

Optical microscopes on the other hand provide very different information compared to the AFM. Light which interacted with the sample or photons emitted by the sample are captured on a camera. There is a vast range of optical microscopy techniques available. But all the conventional techniques share a certain resolution limit fundamental to optical microscopy which has been described by Ernst Abbe in 1873. He found that light converging to a spot will make a spot that cannot be arbitrarily small due to diffraction of light. The radius of a spot of light at a wavelength λ, in a medium with refractive index n, which converged with an angle θ will be

$$\mathrm{d} = \frac{\lambda}{2n\sin\theta}$$

where $n \sin \theta$ is called the numerical aperture (NA). This limit in spot size (diffraction limit) is a fundamental limit of the resolution of optical microscopes. Using a high NA objective lens (Figure 1.3a) with NA 1.65 and a wavelength of 488 nm the spot size limit is at around 150 nm in a diffraction limited system, hence objects which are closer together cannot be resolved.

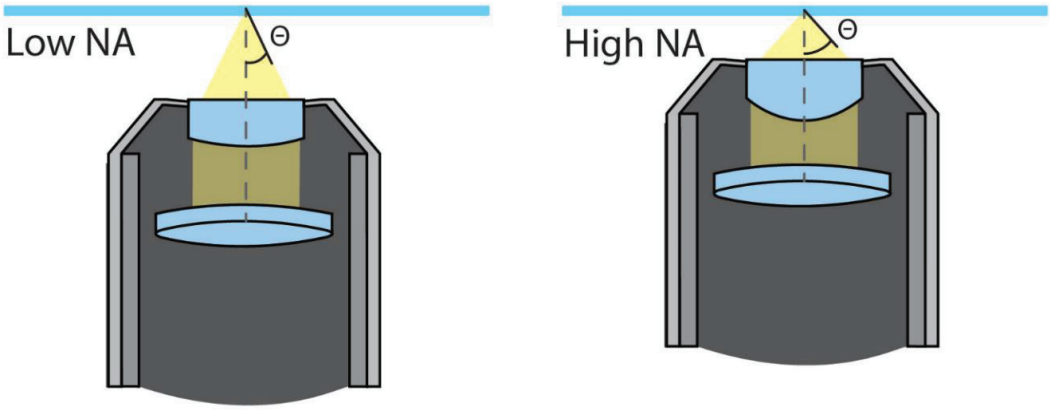

Figure 1.3 Microscope objective lenses. Resolution limit of optical microscopes depends on the numerical aperture of the system. More light is captured at higher numerical apertures.

Recent developments in fluorescence microscopy led to the invention of new techniques, single molecule localization microscopy techniques capable of resolving structures which are closer together than allowed by the diffraction limit. The basic concept of such techniques is to sequentially image only a sub set of fluorophores which are further apart from each other than the diffraction limit such that they don't overlap and can be identified as individual spots. Each of spot on the camera should then correspond to the positions of single fluorescent molecules. In order to image all the fluorescent molecules at least once with very few individual molecules in each frame, many thousand image frames have to be recorded. In a post-processing step the center of each spot in each camera frame can then be determined very precisely by a Gaussian fit, even at a resolution smaller than the size of a pixel on the camera. This can be achieved if only a subset of all fluorescent molecules are emitting photons in each image frame but during the course of the measurement all molecules can be mapped at least once. Photoactivated localization microscopy (PALM) introduced by Betzig et al.(*2*) or direct stochastic optical reconstruction microscopy (dSTORM) introduced by van de Linde et al.(*3*) are based on this concept of localizing individual fluorophores, depicted in Figure 1.4. Most of the fluorescent molecules in a sample are in an OFF state and only a subset of the molecules are in an excitable ON state and emit photons upon laser excitation. Hence if the number of molecules in an ON state is low enough such that they are far apart from each other the center of each spot and as thus the localization of these individual molecules can be determined very precisely. In the next image frame a different subset of molecules in the ON state are imaged till all the molecules in the sample are mapped. A reconstruction of the localizations of all the molecules imaged in all the image frames will provide an image with a resolution limit in the order of ~20 nm which is about one tenth of the diffraction limit. Therefore, by repeatedly localizing a small number of molecules the diffraction limit can be surpassed.

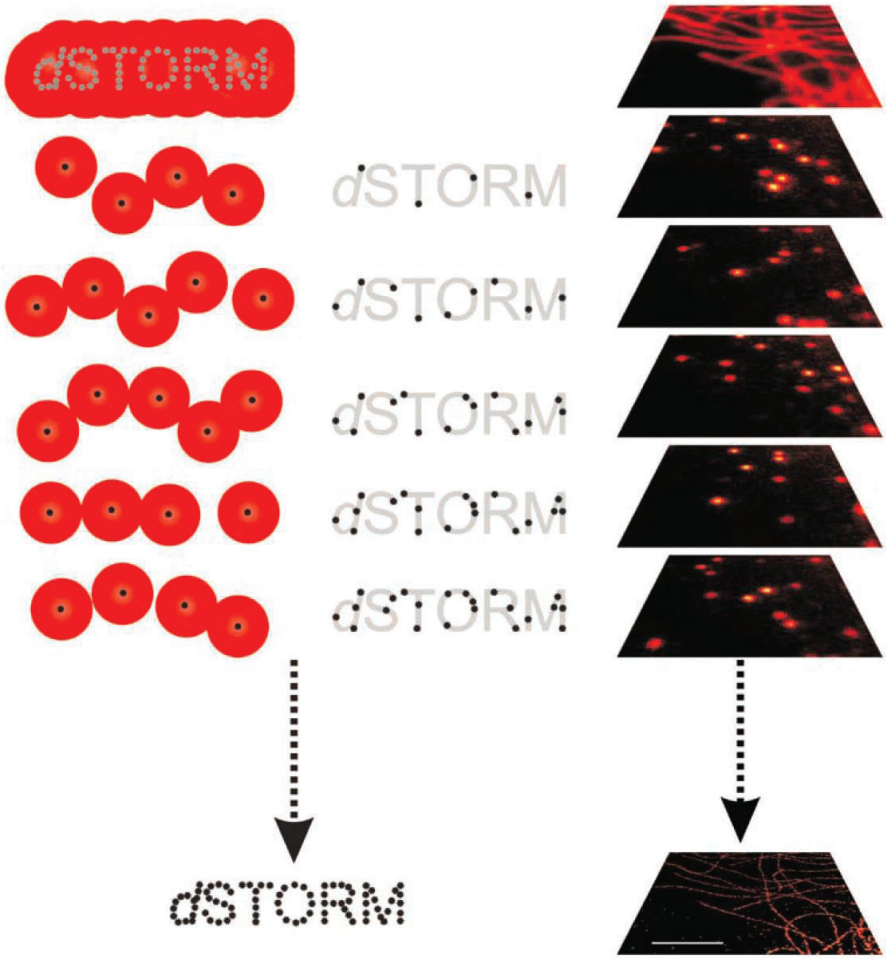

Figure 1.4 dSTORM principle. Instead of imaging all fluorescent molecules at the same time, only a subset of molecules is localized in a every image frame. Precise localization of the centers of each spot and reconstructing an image out of all the frames acquired a high resolution image can be obtained.(*3*)

Chapter 2 Stage for combined HS-AFM/FM

Contrary to the AFM, fluorescence microscopy (FM) has the capability to depict structures which are located below the surface inside the cell of a transparent biological sample. Thus, AFM and FM provide very different, complementary information about the sample. AFM provides the structural information of the surface, the FM specific structures of interest beyond the surface. A specific subset of biomolecules executing a particular biomolecular function can be imaged by simply adding a fluorescent tag to the biomolecule of choice. With the help of laser excitation and appropriate optical filters these biomolecules attributed with a biomolecular function can then be imaged. As in AFM, fluorescent imaging is as well capable of live cell imaging providing information about the distribution of biomolecules inside the cell. This allows to use the same samples for AFM and FM alike. Probing the sample with both modalities therefore renders a more complete view of the sample and helps interpreting individual images.

The integration of AFM and OM into one single instrument has been of interest for a broad community in biological research. The very different nature of the microscopes each necessitate specific requirements that have to be met to ensure correct functioning. Mechanical stability is one of the main goals that has to be achieved to reduce mechanical noise and ensure undisturbed operation of the AFM. The use of high NA objective lenses on the other hand will enable high resolution optical images. Numerous different designs have been proposed and implemented. In early designs a platform was directly mounted onto the frame of the inverted optical microscope onto which the AFM was placed (Figure 2.1a). In such a setup the mechanical stability of the AFM support is dependent on the mechanical stability of the optical microscope frame. As optical microscope frames are not designed to be integrated with AFMs the performance of such a setup is reduced compared to an AFM that is not integrated with an inverted microscope (Figure 2.1a).

By restricting the access to the sample by the AFM to the upper side, the optical inverted microscope has free access from the bottom. This allows the full use of imaging capabilities relying on illumination from the bottom as is common for many fluorescence imaging techniques. Moreover, high magnification objective lenses can then be used which require to be positioned within hundreds of micrometers from the bottom of the microscope glass coverslip due to their short working distance. They enable a specific illumination pattern commonly known as total internal reflection fluorescence (TIRF). Under such illumination conditions the excitation light instead of passing through the microscope coverslip glass, travels along the microscope coverslip glass minimizing the excitation volume to a very thin layer on the bottom of the sample. This limits out of focus background light effectively by minimizing the excitation volume, thereby increasing the contrast. This illumination condition is often used in 2D super resolution microscopy. Upon these

considerations we aimed at designing our instrument in a way that would allow us to use an inverted OM equipped with high-magnification objective lenses, enabling super-resolution microscopy techniques. On the AFM side we are using a commercially available tip-scanning high-speed AFM (HS-AFM). As the AFM can access the sample only from the top side and the OM requires the sample to be in a fixed position sample scanning AFMs can be used. The HS-AFM will allow measurements of live-cell samples in a time-resolved manner.

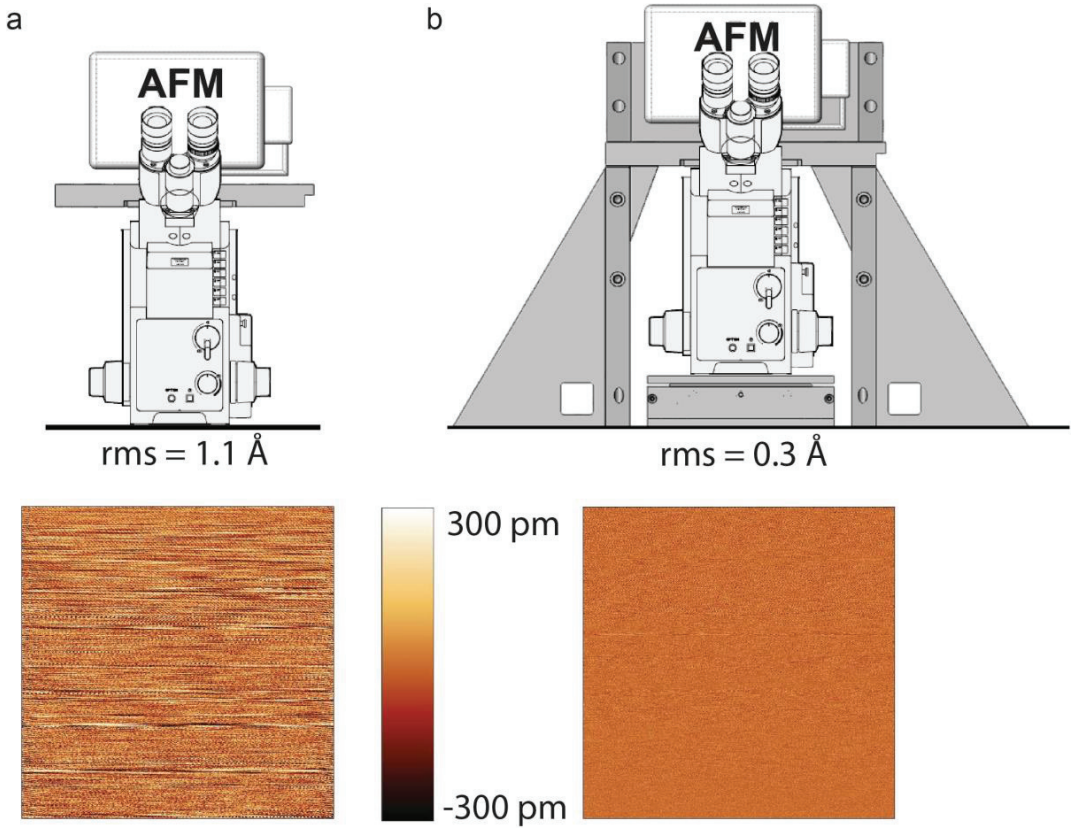

Figure 2.1 Comparison of setups to combine AFM and OM. a) In the conventional setup the AFM scanner is directly mounted on the OM frame. The noise measured is 1.1 Å RMS. The amplitude channel of the noise measurement is shown below. b) The AFM support is mechanically de-coupled from the OM. The noise measured drops to 0.3 Å RMS, with the corresponding amplitude channel of the noise measurement below.

In order to prevent the deterioration of the HS-AFM performance by solely mounting the support for the HS-AFM on the frame of the OM as described above and outlined in Figure 2.1a we aimed at developing a new design for the mechanical support. In principle, the transmission of mechanical vibrations from the frame of the OM to the HS-AFM unit and sample can be prevented by mechanically de-coupling the AFM support structure from the frame of the OM. The support structure for the AFM can instead be bolted on a vibration isolation table minimizing mechanical noise sources.

To allow space for the inverted OM to be positioned directly below the HS-AFM scan unit the shape of the support structure is an inverted U. To maximize the stability of the structure brack-

ets are used to bolt the sides of the structure to the vibration isolation table as well as to stabilize the connection between the sides and the top of the structure (Figure 1.1b). The shape and dimensions of the support structure allow the inverted OM to be positioned inside and optical accessories to be attached to the frame of the OM. The HS-AFM scanner is then mounted on a heavy metal block bolted on top of this support structure with the HS-AFM tip aligned to the centre of the field of view of the inverted optical microscope.

Noise measurements, where the amplitude of a cantilever in oscillation is measured over time at very low feedback gains are an estimation for the AFM system performance. Such measurements are shown in Figure 2.1 below. Clearly, the HS-AFM positioned on the platform that mechanically decouples it from the optical microscope performs better. It resulted in a reduction of the RMS value by a factor of more than 3, demonstrating the improvement in performance. With this system, RMS values as reported by the HS-AFM supplier measured on the original HS-AFM platform are achieved, showing that a well-designed support structure allows the combination of the HS-AFM with an OM without reducing its performance.

A disadvantage of positioning an AFM ontop of the inverted microscope however, is that optical components cannot be placed above the sample. Therefore, condensers nor phase plates can be introduced preventing for example the use of phase contrast imaging. The AFM scanner head however is equipped with a built-in light source which can be used for general orientation on the sample mimicking transmission light, however adjustment of the illumination to provide Köhler illumination is not possible.

Chapter 3 High-Resolution Correlative Microscopy: Bridging the Gap between Single Molecule Localization Microscopy and AFM

This is a verbatim copy of an article that has been published in a peer reviewed journal: P.D. Odermatt, A. Shivanandan, H. Deschout*, R. Jankele, A.P. Nievergelt, L. Feletti, M.W. Davidson, A. Radenovic and G.E. Fantner. High resolution correlative microscopy: Bridging the gap between Single Molecule Localization Microscopy and Atomic Force Microscopy.* Nano Lett, *2015.*

**contributed equally*

3.1 Abstract

Nanoscale characterization of living samples has become essential for modern biology. Atomic force microscopy (AFM) creates topological images of fragile biological structures from biomolecules to living cells in aqueous environments. However, correlating nanoscale structure to biological function of specific proteins can be challenging. To this end we have built and characterized a correlated single molecule localization microscope (SMLM)/AFM that allows localizing specific, labelled proteins within high-resolution AFM images in a biologically relevant context. Using direct stochastic optical reconstruction microscopy (dSTORM)/AFM, we directly correlate and quantify the density of localizations with the 3D topography using both imaging modalities along (F-)actin cytoskeletal filaments. In addition, using photo activated light microscopy (PALM)/AFM, we provide correlative images of bacterial cells in aqueous conditions. Moreover, we report the first correlated AFM/PALM imaging of live mammalian cells. The complementary information provided by the two techniques opens a new dimension for structural and functional nanoscale biology.

3.2 Results

Observing nanoscale structural changes associated with many cellular processes is essential for understanding the complex mechanisms underlying biomolecular function. Performing the experiments in aqueous environments is essential for maintaining cellular integrity. At the nanoscale, the two imaging modalities atomic force microscopy (AFM) and single molecule localization microscopy (SMLM) fulfil the requirement of concomitant assessment of structures and dynamics under close to physiological conditions. AFM has long since provided nanoscale structural information on living cells.(*4-6*) Recent advances in high-speed AFM have even been suc-

cessfully used to directly visualize the dynamics of molecular machinery such as protein motors.(*7, 8*) In addition, newly emerged SMLM techniques extended all the advantages of fluorescence microscopy beyond its diffraction limited spatial resolution of about 200 nm (*2, 9, 10*) and provided new important insights into structural organization, (*11, 12*) dynamics,(*13*) and quantification (*14-16*) of biomolecules. Both techniques by themselves have proven to be very powerful for research in nanoscale structural biology. However, in SMLM, biomolecules themselves are invisible, and one observes/localizes only the fluorophores. In addition, translating the SMLM localization precision, typically between 10 and 25 nm, into spatial resolution is still very challenging due to a number of complicating factors.(*17*) Therefore, early on, the validation of SMLM has been carried out with correlative imaging using transmission electron microscopy (TEM).(*2*) Yet, in the case when SMLM is correlated either with TEM(*2, 18*) or scanning electron microscopy (SEM), (*19, 20*) sample preparation conditions are far from physiological, prohibiting the observation of live processes. Structural artefacts might as well be introduced unless one performs experiments on vitrified samples as Chang et al.(*18*)

AFM on the other hand has proven to obtain submolecular resolution on membrane proteins in solution, (*21*) but it fails at providing biomolecular specificity. In combination, AFM and SMLM hold promise for doing correlated nanoscale biomolecular and structural characterization on living samples in physiological conditions.

Nevertheless, the first attempts to correlate AFM with SMLM(*20*) have not fully exploited this opportunity. For example, Monserrate et al.(*20*) performed AFM imaging of DNA in air, dried on a mica substrate. While this approach allows a nice comparison of the two techniques, it does not allow for the two techniques to complement each other to learn new things about structure–function relationships in living systems. In addition, the presence of the thin mica sheet on the glass coverslip deteriorated the point spread function (PSF) and compromised the performance of SMLM. Although Chacko et al.(*22*) employ both modalities in physiological conditions, their samples were chemically fixed.

In order to exploit the full potential of high-resolution correlative AFM/SMLM imaging, one has to maintain optimal performance in both imaging modalities. This requires careful design of experimental procedures so that the two methods do not deteriorate each other's performance. In particular, during AFM imaging, maintaining low imaging forces is essential to ensure minimal damage to the soft biological samples in fluid. At the same time, one has to maintain a low level of noise that should not be compromised by the integration with the SMLM optical microscope. To this end, we have built a mechanical support structure to hold the AFM in place without it mechanically contacting the microscope body (Figure 3.1). Simultaneously, in SMLM it is important that the fluorescent labelling strategy minimally affects the 3D structure of the sample. Due to this requirement, from the plethora of labelling/ imaging strategies we have chosen direct stochastic optical reconstruction microscopy (dSTORM) and photo activated light microscopy (PALM). In dSTROM, the light-induced reversible photoswitching of organic fluorophores is obtained in the presence of millimolar concentrations of reducing thiol compounds such as dithiothreitol (DTT), glutathione (GSH), or mercaptoethylamine (MEA), but without requiring the presence of an activator fluorophore in aqueous buffer.(*23*) In particular, using fusion proteins or intercalating small molecules such as fluorescently labelled phalloidin, allowed us to com-

pletely avoid antibodies that would have otherwise significantly altered the sample's 3D structure. Also, after ensuring that the laser used by the AFM to detect the cantilever motion does not overlap with the fluorophore excitation spectra, only a subset of fluorophores is available for correlated microscopy.

The purpose of correlated AFM/dSTORM microscopy can be two-fold: first to compare and validate the resolution of one technique with the other, and second to provide complementary information about two different aspects of the same biological sample. To establish accurate correlation and measurement protocols, we chose F-actin as a first test sample, since high-resolution images of F-actin have been reported in both imaging modalities. Monomers in actin filaments are very weakly bound since they have to be dynamically assembled and disassembled in the cell. Even after stabilization by phalloidin they are very delicate. AFM imaging of actin filaments in physiological buffer therefore requires excellent force control to image at high resolution without destroying the fibres.(*24*) This makes them an excellent test sample to ensure high-quality AFM performance. Actin is also one of the best studied structures with SMLM both *in vitro* (*25*) and *in vivo*.(*26*)

For direct comparison of the two techniques we imaged polymerized actin filaments on a glass coverslip. The sample preparation procedure was designed to meet the requirements of both techniques. Fluorescently labelled phalloidin was used to prepare the sample for SMLM as well as for AFM, although not strictly required in the latter case. The glass coverslip was functionalized with APTES ((3-aminopropyl)triethoxysilane) to adhere the actin filaments as required for AFM and SMLM imaging. Both imaging modes were performed in buffer; however, each technique requires its own. While the SMLM experiment requires a buffer optimized for blinking of the corresponding fluorescent dye, the AFM requires a buffer which ensures structural integrity and stability.

The best image quality by AFM was obtained using soft cantilevers (BL-AC40TS-C2 cantilevers (Olympus)) with a nominal spring constant of 0.09 N/m operated in peak force tapping keeping the force set point below 100 pN to not destroy the filament. Figure 3.2a shows a high-resolution AFM image of the F-actin, revealing the ~36 nm periodicity of the single left handed generic helix.(*27*) The spacing of the individual G-actin monomers can be seen in the cross section (Figure 3.2c), which is equivalent to the highest resolution AFM images of F-actin published thus far.(*24*)

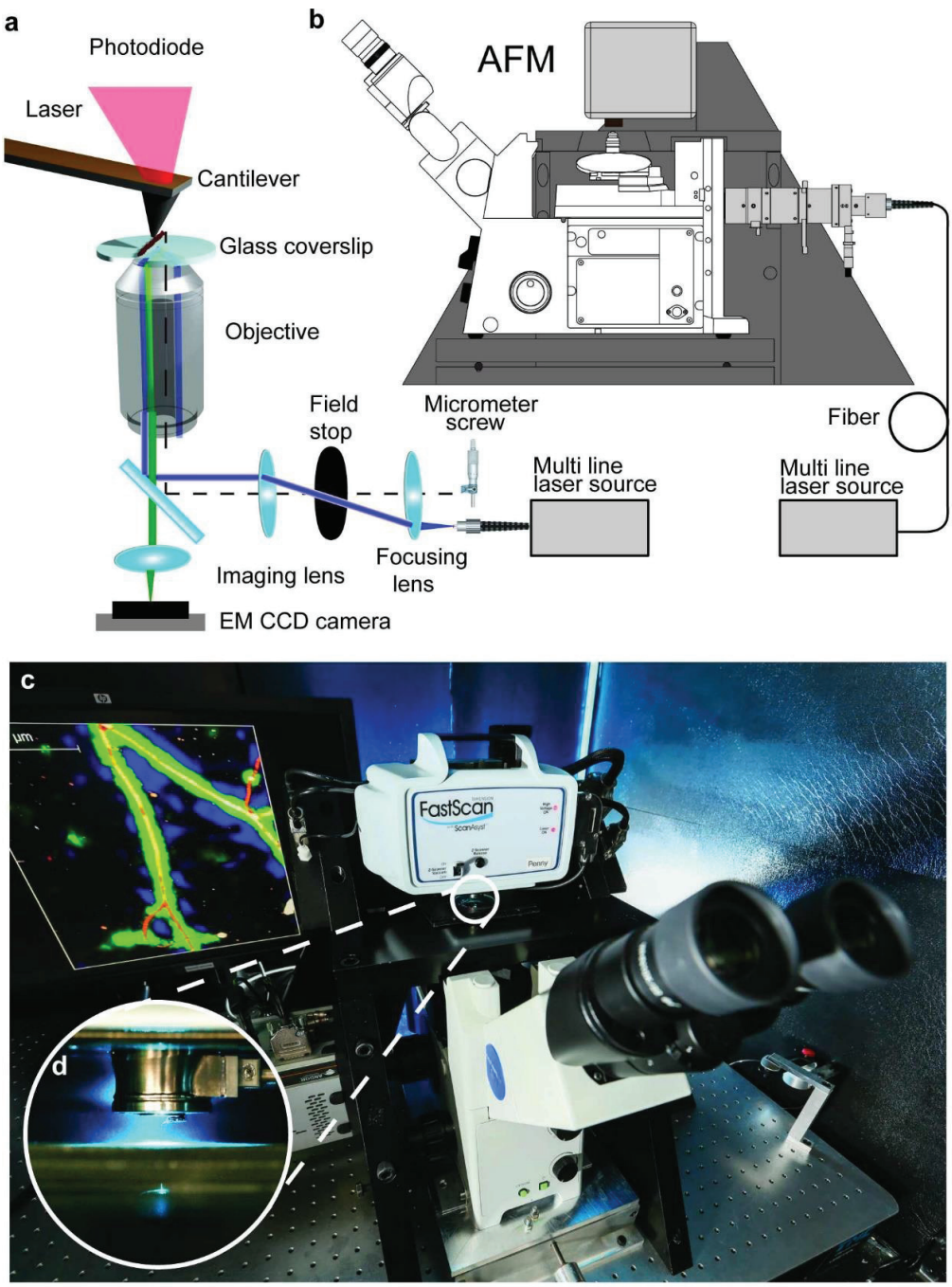

Figure 3.1 Correlative AFM-SMLM: instrument setup. (a) Schematic of the aligned optical path with the AFM cantilever. By laterally translating the incoming laser beam using a micrometre screw, the TIRF illumination condition is enabled. The AFM cantilever is cantered in the field of view by adjusting the position of the inverted optical microscope mounted on an x/y-translation stage (as shown in b and c). (b) Mechanical integration of an inverted optical microscope and the AFM. The inverted optical microscope is mounted on an x/y translation stage. Around it a mechanical support structure is built to hold the AFM in place without mechanically contacting the microscope body. The whole instrument is placed on a vibration isolation platform inside an acoustic isolation box. (c) Photograph of the instrument and (d) zoom in to the AFM cantilever aligned to the optical axis.

The height of F-actin as obtained by AFM was as expected between 6 and 8 nm, and a cross section revealed a full width at half-maximum (FWHM) height of about 10 nm (Figure 3.2d). This result demonstrates that the performance of the AFM is not deteriorated by the fact that it was recorded on the combined SMLM/AFM system.

To assess the image quality obtained by SMLM on this combined system, we imaged F-actin labelled with phalloidin− Alexa647, since the Alexa647 dye has been reported to give optimal SMLM image quality.(*28*) Figure 3.2e shows a dSTORM image with a mean photon count of about 5500 (Supporting Figure 3.1a) and a mean localization precision of 12.5 nm, comparable to the values reported in the literature.(*28*) Actin filaments that have a cross-section profile with a FWHM of ∼24 nm are visible (Figure 3.2e−g). Our measurements demonstrate that a high image quality is obtainable by both techniques individually even when performed on the combined instrument.

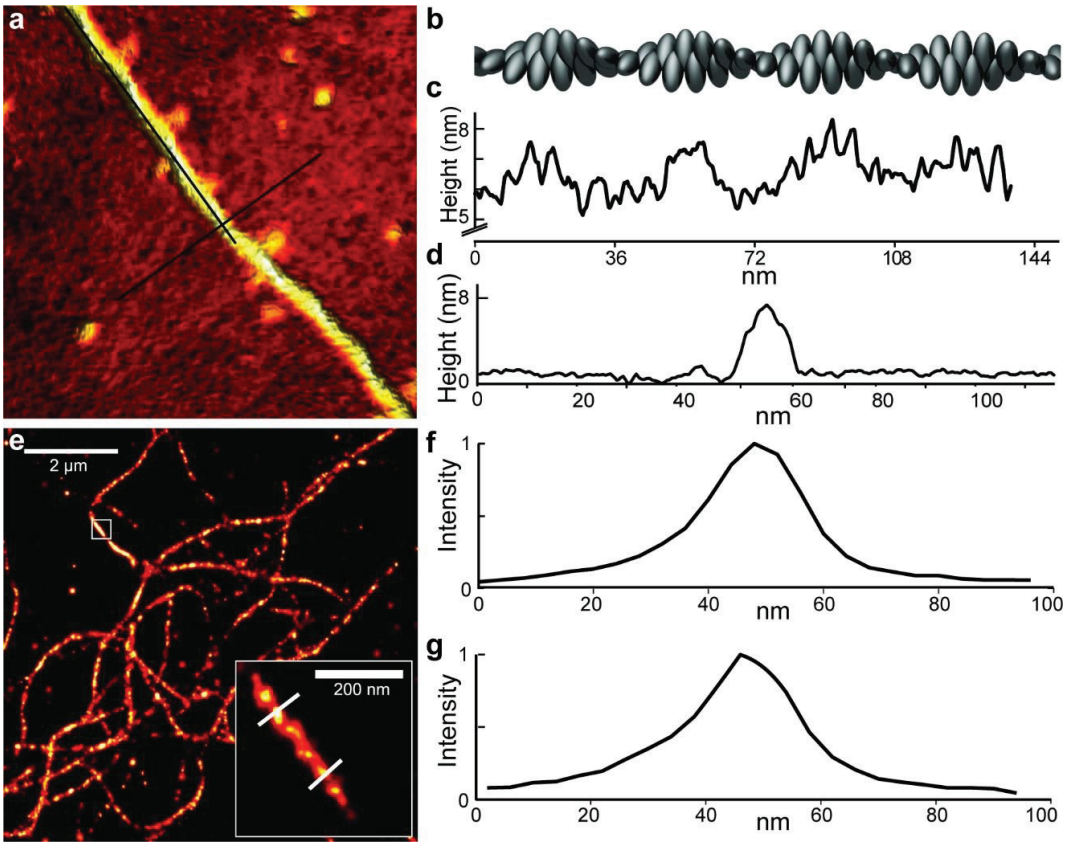

Figure 3.2 Independent performance of AFM and dSTORM on the combined AFM/SMLM system. (a) AFM image of F-actin deposited on an APTES coated glass coverslip (200 nm × 200 nm). (b) 3D model of F-actin showing its apparent helical structure, which is observed by AFM as well. (c) Height profile of F-actin extracted from AFM data, along the filament (profile line indicated in a). The length of one helical turn is 36 nm. (d) Profile perpendicular to the F-actin having a full width at the base of <15 nm. (e) Probability map of F-actin labelled with phalloidin-alexa647 imaged with dSTORM, with a selected filament zoomed in (inset). Pixel size full image: 10 nm, inset: 4 nm. (f and g) Intensity profiles corresponding to the lines in the inset, normalized to the maximum intensity in the profile. The FWHM of the profiles are ≈24 nm.

The procedure for correlated image acquisition is depicted in Figure 3.3a through h. Since Alexa647 emission deteriorates after exposure to the AFM laser (Supporting Figure 3.2a–c), phalloidin−Atto488 was used instead to label F-actin for the correlative experiment. This significantly reduced the bleaching of the dye, although some bleaching still occurs (compare Figure 3.3b and e), but also reduced the photon count and therefore the ultimately achievable localization precision. We recorded the AFM image before recording the dSTORM image, since the dSTORM seemed to degrade the structural integrity of the actin filaments (for details see Supporting Figure 3.10). By minimizing the AFM peak forces to as low as 50 pN, the sample remained intact for the subsequent dSTORM image acquisition, which is a prerequisite for recording correlative images. After the AFM image was recorded, the buffer was exchanged, and phalloidin-atto488 was forced into a triplet state by means of the chemical reducing agent $NaBH_4$ (Figure 3.3f). Subsequently, the reducing agent was washed and the buffer exchanged with the dSTORM imaging buffer containing an oxygen scavenging system to ensure optimal blinking behaviour. Then, the dSTORM image was acquired (Figure 3.3h). Figure 3.3i through k show the resulting AFM images and the dSTORM image, with the squares in Figure 3.3k indicating the areas where the AFM images i and j were taken. Similar results are displayed in Supporting Figure 3.3.

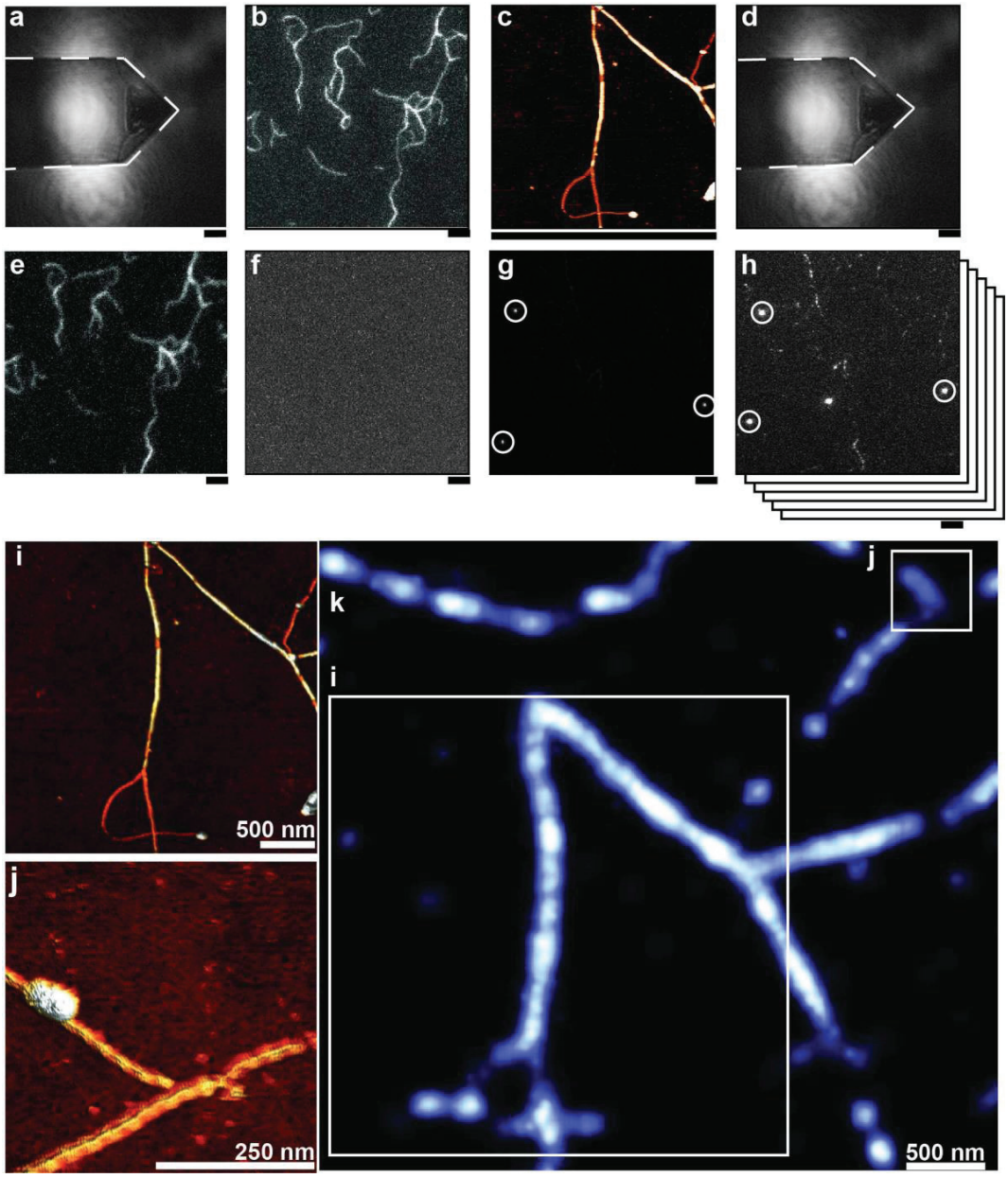

Figure 3.3 Experimental procedure and representative correlated AFM/dSTORM images. Experimental procedure (a–h): (a) The AFM cantilever is cantered in the optical field of view of the camera by translating the inverted microscope in x- and y-direction. (b) The sample is moved, and a region of interest is selected. (c) The AFM image is acquired. (d) To determine the centre of the scan another optical image is taken to account for an applied offset during AFM image acquisition. (e) Then, another TIRF image of the sample was taken and the illumination condition was optimized. (f) The fluorescent labels (phalloidin–Atto488) are quenched chemically and forced into a dark state by exchanging the buffer containing 10 mM NaBH4. (g) The buffer of the sample is exchanged with optimal dSTORM buffer, and beads are added to be used as fiducial markers during the image reconstruction. (h) dSTORM images are acquired. Scale bars below images (a–h) are 3 µm. (i and j) AFM images, (k) reconstructed dSTORM image in probability map representation. (i and j) Areas correlated with AFM.

The effects of various forms of aberrations, primarily spherical aberrations in SMLM,(*15*) are minimized by performing accurate transformation and overlay (detailed in the Supporting Information and Supporting Figure 3.4). The correlative images allow comparison as well as provide complementary information about the sample. Comparing the width of the actin bundles as measured by AFM and by dSTORM, we find that dSTORM provides comparable values to AFM. On the ability to distinguish two diverging bundles of filaments, AFM provides clearer information than dSTORM (Figure 3.4a−c). The height and width of the actin filament bundles measured by AFM was 14 and 65 nm FWHM, respectively. The FWHM of dSTORM was 94 nm and of TIRF 271 nm for the filament bundles.

In addition to direct comparison, the two techniques provide complementary information about the sample. The dSTORM image reveals a nonhomogeneous intensity along the filament which is often attributed to local differences in labelling along the filament. The correlated AFM measurements however suggest that the fluctuation in localization densities is partially due to the presence of actin bundles rather than single filaments. The tendency of F-actin filaments to bundle up (*29*) therefore likely contributes to the local differences of localizations recorded by dSTORM along the filament (Figure 3.4h). We indeed observed a correlation between the height of the F-actin and the number of localizations recorded at that particular location (Figure 3.4i). Along a single filament with a height of around 8 nm about 8 localizations are detected per line scanned by AFM (corresponding to ∼12 nm in length). On the other hand, in areas where an increased height was measured (∼12−14 nm), the number of dSTORM localizations is 1.5 times higher than observed on a single filament.

After correlation protocols have been established, we used the combination of the AFM and SMLM to extract complementary information about two different aspects of one and the same biological sample. For this we extended our method to samples including chemically fixed bacterial cells (Figure 3.4j) and mammalian cells (Supporting Figure 3.6). *Escherichia coli* (*E. coli*) expressing the fusion protein RNP-mEOS2 was measured by AFM and subsequently by PALM. We chose PALM over dSTORM for these experiments since PALM can be performed with lower laser power, which is better suited for eventually extending the technique to live cell imaging. The AFM provides the 3D morphology of the bacteria, while PALM provides the expression level and the 2D projection of the spatial distribution of the fusion protein. Interestingly, one of the bacteria showed no presence of the fusion protein in a part of the PALM image. The AFM image clearly shows that this bacterium is situated slightly on top of two other bacteria. We hypothesize therefore that the fusion proteins of this particular bacteria were not mapped because the bacterium was out of the illumination volume covered in TIRF conditions. This is a good example where the combination of the two techniques yields a clearer interpretation of the microscopy data than PALM alone. However, the conventional PALM we use does not provide 3D information on the location of the fluorescence signals with respect to the morphology of the cell. Recent advancements in 3D PALM (*30*) would further leverage the power of the correlated technique.

The same technique can be applied to correlated AFM/ PALM measurements on mammalian cells. Supporting Figure 3.6 shows a fixed mouse embryonic fibroblast expressing the fusion pro-

tein paxillin–mEos2, which is part of the focal adhesion complexes that form contact with the substrate.

Performing correlated SMLM and AFM measurements within biologically relevant media not only allows for direct comparison of the two techniques but also allows us to learn more about each individual technique and to augment the weaknesses of one with the strength of the other. In the case of the actin filaments, AFM provided a reference for the location and height of the filaments that could be directly compared to the labelling density fluctuations along the filaments as observed by SMLM. This showed that the labelling fluctuations originate partially from the presence of double and triple filaments (Figure 3.4h and i) and is therefore not solely due to insufficient labelling as it was incorrectly assumed. On the other hand, in areas along the filament revealed by AFM to be a single filament, the fluctuations can now be unequivocally attributed to insufficient binding of tagged phalloidin. This dual information makes the comparison between different labelling protocols much more effective and accurate. On the other hand, the fact that the number of localizations per scan-line correlates well with the AFM height (and therefore the number of filaments) suggests that the localization intensity could eventually be used for quantifying the number of actin filaments in a bundle in situations where no AFM information can be obtained such as in whole cell imaging.

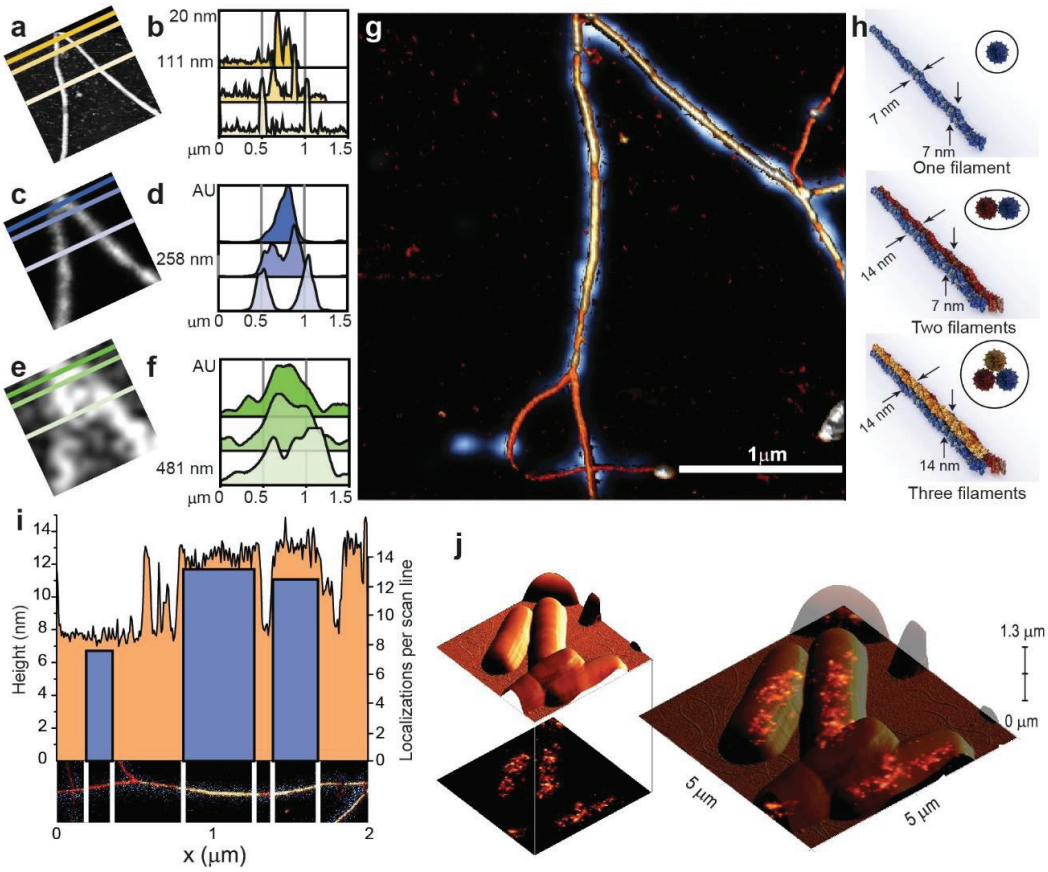

Figure 3.4 Comparison of AFM, dSTORM, and TIRF imaging resolution from correlative imaging. (a, c, and e) AFM, dSTORM, and TIRF images, respectively (1.5 µm × 1.5 µm), of correlated filaments. Lines and colours indicate the location of profiles shown in (b, d, and f). (g) Overlay of dSTORM probability map (blue)

and 3D rendered AFM image (yellow–brown). (h) Different F-actin arrangements suggested based on the AFM data. (i) Orange: Maximum height projection of the AFM section shown below the plot. Blue: Number of localizations detected in regions between the white lines per line scan of the AFM. In higher areas more localizations are observed. (j) Correlative AFM/PALM image of E. coli bacteria expressing RNA polymerase–mEos2.

Thus, far, we have chosen our sample so that a direct comparison of the two techniques is possible and we also showed the potential of revealing complementary information in fixed bacteria and mammalian cells. Now that the correlation between the two techniques has been established, they can be reliably used to complement each other in applications where the protein specific SMLM information has to be put in a 3D cellular or mechanical context. This will be especially important for the recent and ongoing developments in 3D SMLM. (*31-34*) Since we perform our AFM experiments in physiological solution, it is even possible to perform live cell imaging and nanomechanical stimulation using the AFM cantilever. Using the combination of live cell AFM (*35-37*) and live cell SMLM,(*38*) one could observe the reaction of the cells to nanomechanical stimuli with unprecedented resolution. A major concern for live cell imaging is the image acquisition speed of both SMLM and AFM, as they both traditionally require tens of minutes to obtain a high quality image. With the development of high speed AFM by Ando et al.(*7*) and the pioneering work in high-speed SMLM by Zhuang et al. (*38, 39*), real time nanoscale imaging of living cells is within reach. Our combined AFM/SMLM system is already capable of such experiments since live cell PALM has already been reported,(*13*) and the AFM we used is capable of imaging live cells within a minute or less.(*40*) Figure 3.5 shows such time-resolved AFM and PALM image sequences of live CHO-K1 cells in physiological environment. From the whole cell shown in Figure 3.5a, we chose the leading edge (upper corner) for time-resolved analysis (Figure 3.5b and c). AFM images (Figure 3.5b) were recorded at 1 min intervals showing filopodia already extended with subsequent following of the lamellipodium. PALM images shown in Figure 3.5c were recorded directly after AFM imaging, and the cell edge from the last image in the AFM sequence is shown for reference in the PALM images. Fluorescent frames were recorded at a rate of 20 frames/s and processed 5000 frames at a time with a “running average” of 1000 frames to create each PALM image (see methods, Supporting Figure 3.11 and Supporting movie 1 for details). Figure 3.5d–g show zoom-ins of regions depicting paxillin clusters in focal adhesions. In d and e, a paxillin cluster disappears at one place, while in f and g new ones appear.

The dynamic changes we observed in both the AFM and PALM images and the complementary information they provide demonstrate the potential of correlated AFM/PALM imaging of live cells. It should be noted that in these experiments the AFM and PALM data were recorded in a correlated fashion, but not simultaneously. A better integration of the AFM operating software with the PALM acquisition software would allow for truly simultaneous imaging. While many of the experimental conditions for routine experiments still have to be worked out, we expect this to become a truly enabling method in the study of mechanobiology and mechanotransduction.(*41, 42*)

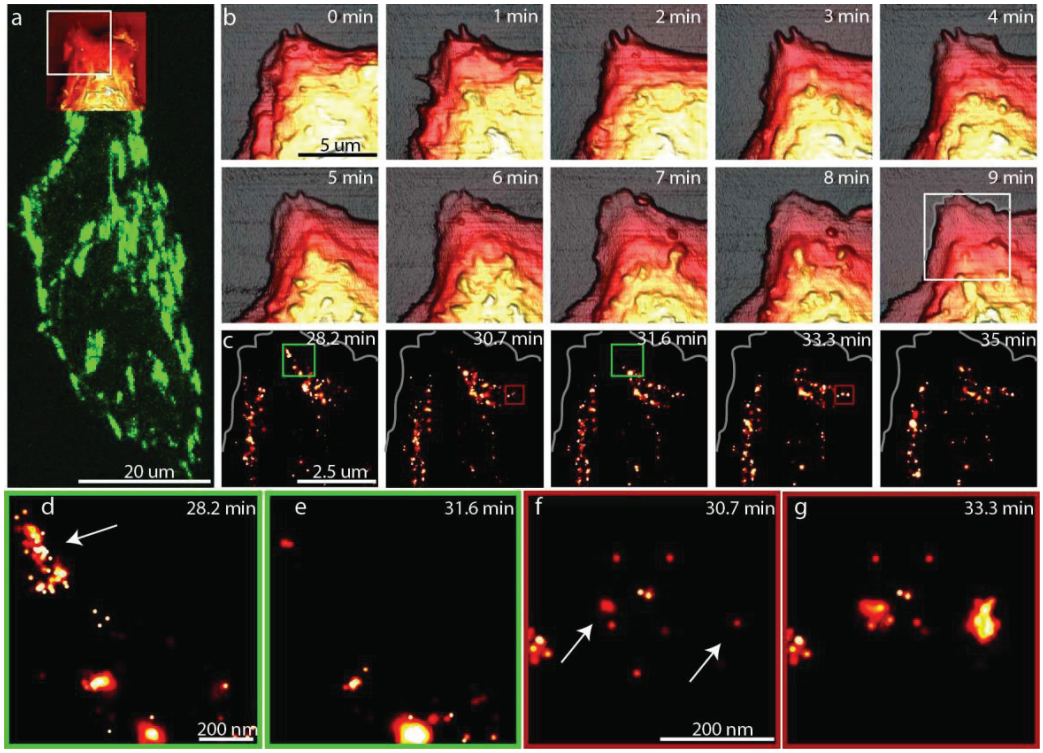

Figure 3.5 Live-cell time-resolved AFM/PALM on mammalian cell. (a) CHO-K1 cell transiently expressing a paxillin-mEos2 construct imaged in its off-state under TIRF illumination. Overlaid is an AFM overview image from the upper part of the cell. The white square outlines the area zoomed in for the AFM time-series shown in b. (b) Time-resolved AFM sequence of the leading edge of the cell, showing the normal cell behaviour of filopodia protrusion with subsequent lamellopodia extension. The frame rate is 1 min−1. The white square in the AFM image recorded after 9 min marks the area of subsequent PALM images shown in c. (c) Live-cell PALM time series showing the reorganization of the paxillin-mEos2 clusters. (d) Zoom-in of the green square outlined in c at 28.2 min. (e) The same area as in d at 31.6 min. (f) Zoom of the area outlined in red in (c) in the image taken at 30.7 min. (g) Zoom of the same area as in part f at 33.3 min. While the AFM images show the dynamics of the cell membrane, the PALM series monitors the changes in the paxillin-mEos2 clusters. In d and e, paxillin clusters disappear from the top left corner (arrow). New paxillin clusters are formed within 3 min at the site shown in f and g (arrows).

3.3 Materials/Methods

Choice of Labelling Strategy. What fluorescent labelling strategy is best suited depends on the kind of correlated experiment that is performed. In the case of the actin filaments we imaged the same aspect of a sample with both modalities. In that case it is imperative that the fluorescent labelling does not interfere with the sample structure as measured by AFM. In such a case it is preferential to use a small intercalating dye such as fluorescently labelled phalloidin. When one images different aspects of a sample with the two techniques (such as we did in the combined imaging of cells), a broader choice of labelling strategies is available such as antibody labelling or genetic expression of fluorescent fusion proteins. We chose the latter for live cell imaging as it allows for labelling of intracellular structures without permeabilizing the cell membrane. In all cases, it is essential however that the AFM laser does not bleach the fluorophores.

F-Actin. F-actin has been polymerized from G-actin following the manufacturer's protocol (BK003, Cytoskeleton, Inc.) and stored on ice subsequently. To 5 µL of a G-actin aliquot (200 µM) 45 µL prechilled general actin buffer was added, ending up with 20 µM G-actin in 5 mM Tris-HCl pH 8.0, 50 mM KCl, 0.2 mM $CaCl_2$. Next, 5 µL of 10× polymerization buffer was added, resulting in a final concentration of 50 mM KCl, 2 mM $MgCl_2$, 1 mM ATP, and incubated at room temperature to polymerize for 2 h before storing on ice. Actin was stored up to one month.

E. coli. E. coli bacteria expressing RNA polymerase labelled with mEos2 (*43*) were kindly provided by Dr. Mike Heilemann. The bacteria were grown in lysogeny broth (LB) medium supplemented with ampicillin (0.1 mg/mL) at 37 °C in an orbital shaker overnight. Then, 100 µL of bacteria solution was added to 4 mL of fresh medium and incubated again for 3 h. Subsequently, 1 mL was pelleted by centrifugation, and the supernatant was discarded. The pellet was resuspended in deionized water, and the washing step was repeated once more. The pellet was eventually resuspended in 400 µL of deionized water and used for subsequent sample preparation on the prepared glass coverslip.

Glass Coverslip. 25 mm diameter round glass coverslips (72225-01, Electron Microscopy Sciences) were cleaned by piranha etch (H_2SO_4 and H_2O_2 at a ratio of 2:1) on a heating plate for at least 20 min and then left to cool down. Then, the coverslips were thoroughly rinsed with water and blown dry by a nitrogen stream. On coverslips prepared for the F-actin sample, 500 µL of water (Milli-Q) containing 0.5% (v/v) APTES (440140, Sigma-Aldrich, Switzerland) was deposited and incubated for 10 min before rinsing with water. Coverslips were then dried at 65 °C for 1 h in vertical position. Coverslips were prepared freshly on the day of the experiment.

Cleaned coverslips used to deposit E. coli were immersed for 10 min in a solution containing 0.05 mg/mL poly-L-lysine (PLL) hydrobromide (Sigma, P1524) and 10 mM Tris at pH 8. Coverslips were then dried in a vertical position at room temperature overnight and used within a week.

Cleaned and coated coverslips were glued into a custom-made holder before the respective sample was deposited.

Sample Deposition and Imaging Buffers. F-actin samples were prepared as follows: 3 µL of phalloidin−Alexa647 (A22287, Life Technologies) or phalloidin−Atto488 (49409, Sigma-Aldrich, Switzerland) and 1 µL of polymerized F-actin was added to 45 µL of Buffer A (2 mM $MgCl_2$, 1 mM EGTA, 20 mM imidazole−HCl, pH 7.6) and incubated in darkness for 10 min. Then 100 µL Buffer A was added, and 50 µL of this was deposited on an APTES-functionalized coverslip. Another 150 µL Buffer A was added to the sample and incubated for 5 min. Additionally, up to 1 mL of Buffer A was added for AFM experiments.

E. coli samples were prepared as follows. A drop of concentrated bacteria solution was deposited onto a PLL coated coverslip, and bacteria were left to adhere for 30 min before the coverslip was gently washed with water. After imaging by AFM in water, the sample was washed with PHEM buffer (60 mM Pipes, 25 mM HEPES, 10 mM EGTA, and 2 mM $MgCl_2$ at pH 6.9) and fixed with 4% paraformaldehyde in PHEM buffer for 30 min without changing the position of the sam-

ple. Subsequently, the sample was washed with PHEM buffer 3 times, and PALM images were acquired.

CHO-K1 Cells. CHO-K1 cells were grown in an incubator at 37 °C, 5% CO_2 in DMEM-F12 supplemented with 10% (v/v) FBS and 1% antibiotics to 70% confluency prior to transfection. 4 × 105 cells were transfected with 2 µg of plasmid DNA containing the paxillin−mEos2 sequence with a Neon electroporation system. Cells were then seeded in a 6-well plate with DMEM supplemented with FBS only. The following day they were transferred onto plasma cleaned fibronectin coated 25 mm diameter glass coverslips and grown for another 2−24 h. Prior to the experiment the cells on the coverslip were transferred on a home-built coverslip heater shown in Supporting Figure 3.9 to keep them at 37 °C and the medium was exchanged to DMEM without phenol red buffered with 25 mM Hepes. As imaging took less than 35 min, it was not necessary to have a controlled CO_2 environment. For longer term imaging we suggest putting a CO_2 cage around the sample including the AFM, or use the commercially available perfusion chamber for the FastScan Bio AFM.

AFM. AFM experiments were conducted with a Dimension FastScan (Bruker, USA) mounted on a custom-built support structure on top of an inverted optical microscope (IX71, Olympus, Japan). BL-AC40TS-C2 cantilevers (Olympus, Japan) with a nominal spring constant of 0.09 N/m and a resonance frequency of 110 kHz were used to image the F-actin samples. Images were taken in PeakForce QNM mode at a maximal force <100 pN, at a resolution of 512 × 256 pixels. E. coli samples were imaged using Scanasyst-Fluid cantilevers (Bruker) with a nominal spring constant of 0.7 N/m and a resonance frequency of 150 kHz. For the live-cell experiment on CHO-K1 cells Fastscan-D cantilevers (Bruker) with a nominal spring constant of 0.25 N/m and a typical resonance frequency in water of 110 kHz were used. Images were taken in tapping mode at a resolution of 512 × 128 and a frame rate of 1 min−1. AFM data was processed with standard SPM software. Supporting Figure 3.7 displays 2D AFM height images of the 3D representations shown in the main figures. The reconstruction of the tip used in Figure 3.3 as obtained by the software Nanoscope Analysis (Bruker, USA) is shown in Supporting Figure 3.8. More details are provided in the text of the Supporting Information.

dSTORM. For the imaging with Alexa-647, the sample was imaged in the buffer conditions described in Olivier et al.(*44*) 2 mL of buffer (pH 7.5) was composed of: 1.685 mL of PBS, 200 µL of Tris (100 mM pH 7.4), 20 µL of 1 M mercaptoethylamine stock pH 8 (MEA, Sigma; pH adjusted with glacial acetic acid 100%), 7 µL of β-mercaptoethanol (M6250, Sigma), 20 µL of 200 mM cyclooctatetraene (COT) stock made from 1.27 mL of DMSO and 30 µL of COT (Sigma), 50 µL of 100 mM protocatechuic acid (PCA, Sigma) at pH 9 (adjusted with KOH), and 20 µL of 5 µM protocatechuic dioxygenase (PCD, Sigma) stock stored in 50% glycerol in 50 mM KCl, 1 mM EDTA, and 100 mM Tris-HCl pH 8.

For the correlative imaging with ATTO-488, the following protocol was used. After AFM imaging, the sample was washed 3× with PBS, leaving 300 µL PBS. 600 µL of PBS containing 0.5 mg/mL NaBH4 was added to a final concentration of 10 mM NaBH4 and incubated for at least 5 min or until the fluorescence was quenched. Then the sample was washed with Tris/Trolox buffer pH 8 (100 mM Tris, 1 mM Trolox), leaving 250 µL of buffer on the sample. Next, 750 µL of buffer con-

taining glucose, catalase, and glucose oxidase was added, resulting in a final concentration of 0.5 mg/mL glucose oxidase, 40 µg/mL catalase and 5% (w/v) glucose. Additionally, 3 µL of 100 nm fluorescent beads (Tetraspeck, Life technologies) was added to the sample.

The dSTORM measurements were performed with a TIRF objective (APON 60X TIRF, Olympus, after a further magnification of 2×, yielding a pixel size of 133 nm) and appropriate optical filters (dichroic: F73-866; emission filter: F72-866, AHF Analysetechnik AG, Germany). Illumination was provided by a monolithic laser combiner (MLC400B, Agilent, UK), and the optical fiber output of the MLC400B was coupled into an optical system (TIRFM Illuminator, Olympus, Japan) in order to generate TIRF illumination. Images were recorded with an iXon Ultra 897 (Andor) EMCCD camera. The power of the 488 nm laser at the fiber output was set to 80 mW and that of the 647 nm laser at a maximum of 140 mW, the gain of the EMCCD camera was set to 200, and images were taken with an exposure time of 20 ms.

PALM. The fixed MEF cells were imaged in PHEM buffer at room temperature. The live CHO-K1 cells were imaged in 25 mM Hepes buffered DMEM at 37 °C. More details can be found in the Supporting Information.

The PALM measurements were performed with the same setup as described in the dSTORM section. The emission light coming from mEos2 was separated from the illumination light using a combination of a dichroic mirror (493/574 nm BrightLine, Semrock) and an emission filter (405/488/568 nm StopLine, Semrock). An optical system (DV2, Photometrics) equipped with a dichroic mirror (617/73 nm BrightLine, Semrock) was placed between the EMCCD camera and the microscope frame. The DV2 splits the emission light from the on- and off-state of the mEos2 and sends each color to a separate half of the EMCCD camera chip.

In order to find a cell in the sample, the mEos2 in the off state was visualized in the green channel by excitation of 488 nm with 5 mW power at the MLC400B output. Before imaging of the mEos2 in the on-state, fiduciary beads (100 nm gold nanospheres, Corpuscular) were added to the sample. The gold beads that did not sediment after 5 min are removed by washing 1× with PHEM for the MEF cell experiment. Imaging of the mEos2 in the on-state was performed in the red channel by excitation of 561 nm with 30 mW power at the MLC400B output. During imaging, the mEos2 in the off-state was activated by 405 nm with a gradually increasing power at the MLC400B output, ranging for 0 mW to 2 mW. The gain of the EMCCD camera was 200, and the exposure time was 50 ms.

Reconstruction. The estimation of the single molecule positions from the images and the rendering as a probability map were done by the code (MATLAB, MathWorks) kindly provided by Dr. Eric Betzig, using the same algorithm described in Betzig et al.(*2*) The localization precision was estimated by means of the expression provided in Mortensen et al.,(*45*) also incorporating the precision loss due to the use of the EMCCD camera. The factor to convert ADC values to photon counts was calibrated as explained elsewhere.(*46*) The drift during imaging was corrected using either fiducial marker traces or using the correlation between frames.(*47*) The dSTORM image displayed in Figure 3.2 was obtained from 16000 frames of imaging, and the one in Figure 3.3 and Figure 3.4 from 60000 frames. For Figure 3.2, only localizations with a precision between 2 and 30 nm, and a photon count between 300 and 50000 were considered. For Figure

3.3 and Figure 3.4, a localization precision cut-off of 50 nm and a minimum photon count of 100 were used. The PALM image displayed in Figure 3.4j was obtained from 62000 frames of imaging and that in Supporting Figure 3.6 from 27000 frames. Localizations in both images were plotted if the corresponding mEos2 image contained at least 100 photons and if the localization precision was between 3 and 30 nm. The PALM time sequence (Figure 3.5c and Supporting Movie 1) was obtained from 14000 frames of imaging, with each individual PALM image in the sequence obtained from a subset of 5000 frames. The time sequence (Supporting Movie 1) was obtained by shifting 1000 (Supporting Movie 1) frames of imaging between each PALM image (for details see Supporting Figure 3.11). In Figure 3.5c selected frames of the sequence are shown. Only mEos2 localizations with a precision between 2 and 40 nm and a photon count of at least 100 were plotted.

Overlay. Overlay between the AFM image and the STORM localizations was done by estimating an affine transformation matrix between the two by minimizing a cost function based on the overlap between the two images. More details are provided in the text of the Supporting Information.

3.4 Acknowledgments

This work was financially supported by FNS grants No. 200021-125319, No. 20021-132206, No. 205321-134786 and No. 205320-152675 as well as the European Union's Seventh Framework Program FP7/2007-2011 under grant agreement 286146 and FP7/2007-2013/ERC grant agreement 307338. A. Shivanandan was funded by a PhD fellowship grant from NCCBI. We thank Dr. P. Annibale for initial help with the instrument. We thank Lina Carlini for discussion, Prof. Mike Heilemann on the generous gift of bacterial strain expressing mEos2-RNAPm and Prof. Nicolas Mermod for providing CHO-K1 cells. G.E.F. thanks Dr. Chanmin Su and Bruker Nano Surfaces for technical support.

3.5 Author contributions

A.S. and H.D. contributed equally to the study. A.R. and GEF. conceived the project. P.D.O. with the help of G.E.F. and A.P.N. built the instrument. L.F. prepared the *in vivo* specimens. A.P.N. designed and built the coverslip heating holder. R.J. and P.D.O. developed the protocol for actin filament sample preparation. A.S. optimized the STORM imaging protocol and implemented and performed the dSTORM/AFM overlay. P.D.O. and A.S. performed the dSTORM/AFM imaging experiments and analysed the data. P.D.O., A.R., and G.E.F. wrote the manuscript with inputs from A.S. and H.D.

3.6 Supporting Information

MEF cell sample preparation. The mouse embryonic fibroblast (MEF) cells are kindly provided by Dr. Luca Scorrano, and the mEos2-paxillin-22 vector is kindly provided by Dr. Michael Davidson. The MEF cells are grown in DMEM supplemented with 10% fetal bovine serum, 1% penicillin-streptomycin, 1% non-essential amino acids and 1% glutamine, at 37 °C with 5% CO_2. A 25 mm diameter round cover slip (# 1.5, Electron Microscopy Sciences) is prepared by first treating it with an oxygen plasma for 5 min and then incubating it with PBS containing 50

µg/ml fibronectin (bovine plasma fibronectin, Invitrogen) for 30 min at 37 °C. To remove the excess of fibronectin, the cover slip is washed 1× with PBS. The cells are transfected by electroporation (Neon Transfection System, Invitrogen). The electroporation is performed on ~500,000 cells using 2 µg of DNA, using 1 pulse of 1350 V with a width of 35 ms. The transfected cells are seeded on the cover slip and grown in DMEM supplemented with 10% fetal bovine serum, 1% non-essential amino acids and 1% glutamine, at 37 °C with 5% CO_2. At least 24 h after transfection, the cells are washed 1× with PHEM (60 mM Pipes, 25 mM HEPES, 10 mM EGTA, and 2 mM $MgCl_2$ at pH 6.9) and fixed by incubating them in PHEM with 4% paraformaldehyde at 37°C for 30 min. After removing the fixative, the cells are again washed 3× with PHEM and the cover slip is glued into a custom made holder that is positioned on the microscope stage.

Imaging procedure. AFM images were then recorded using the Dimension Icon head (Bruker) in peak force tapping mode. Lever A of a Hydra-All-G cantilever (AppNano) with a nominal spring constant of 0.292 N/m was used. Images were recorded at a line rate of 0.5 Hz and a pixel resolution of 512x256.

Overlay between AFM and STORM images. Both AFM and STORM imaging can involve various forms of aberrations. This is especially pronounced in the case the optical aberrations in STORM imaging. Correlative imaging therefore should account for these. Additionally, since the images are not necessarily of exactly the same size and of the same region (our STORM images typically cover a larger field of view than the AFM image), accurate overlay also involves the matching of structures in the image.

We approximate the net effect of these as an affine transformation of STORM localizations. We then estimate the transformation parameters from data to obtain the more accurate overlay.

The 2D affine transformation can be described as $\mathrm{x}' = \mathrm{Ax} + \mathrm{By} + \mathrm{T_x}$ and $\mathrm{y}' = \mathrm{Cx} + \mathrm{Dy} + \mathrm{T_y}$, where x' and y' are the coordinates obtained by the transformation of the original x and y coordinates (STORM localizations); A, B, C and D are lumped parameters that can cause scale, shear and rotation operations; and $\mathrm{T_x}$ and $\mathrm{T_y}$ are translation parameters. We estimate these parameters by the optimization of the overlap between the structures in the STORM and AFM images. The cost function for optimization is computed based on the total number of the affine-transformed STORM localizations with a signal in the corresponding pixel of the AFM image. The optimization and parameter estimation are then done by means of generic algorithm. An example of the estimation process is shown in Supporting Figure 3.4 which shows the overlays before and after the estimation.

For the overlay figures (Figure 3.4g and Supporting Figure 3.3c), since the probability map rendering of the dSTORM localizations involved the shifting of the origin estimated by the overlay algorithm to accommodate the localization error distributions, an additional manual translation operation was performed.

3.7 Supporting Figures

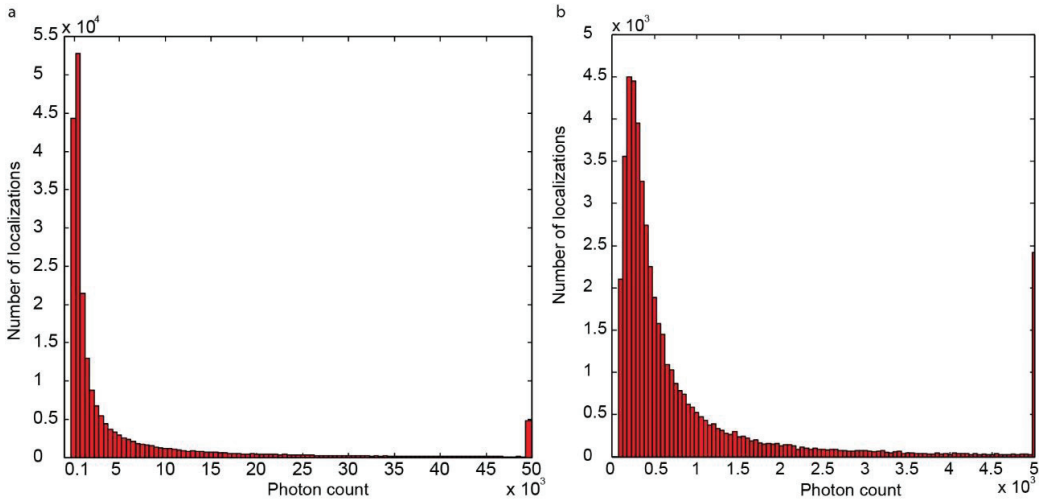

Supporting Figure 3.1 Photon count histograms of STORM images. (a) corresponding to Figure 3.2e (with alexa647) and (b) Figure 3.3 (ATTO488).

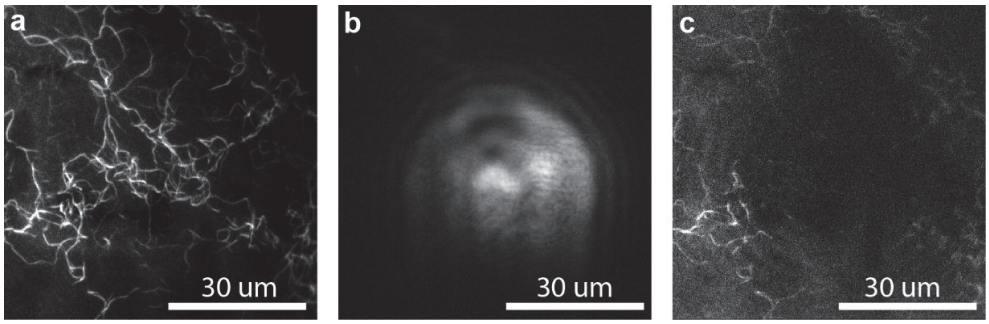

Supporting Figure 3.2 TIRF images of F-actin labelled with phalloidin-alexa647 exposed to the laser of the AFM (a-c) and effect of dSTORM on F-actin structure. (a) TIRF image taken of a fresh sample of F-actin labelled with phalloidin-alexa647 deposited on glass coverslip. (b) The AFM tip was then brought close to the sample surface by false engaging without scanning and kept at this position for 30 minutes. (c) The fluorescence in the area where the cantilever was positioned was substantially bleached after 30 minutes of exposure to the laser of the AFM, making a subsequent dSTORM image impossible. Therefore for correlated AFM/dSTORM atto488 was used.

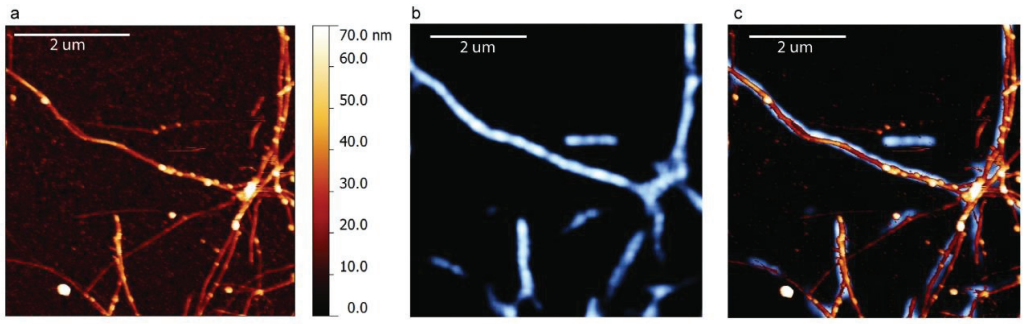

Supporting Figure 3.3 F-actin labelled with phalloidin-atto488 imaged by AFM and dSTORM. (a) AFM height image (b) dSTORM image of the same area (c) Overlay of a and b. Details to the overlay is shown in Supporting Figure 3.4b.

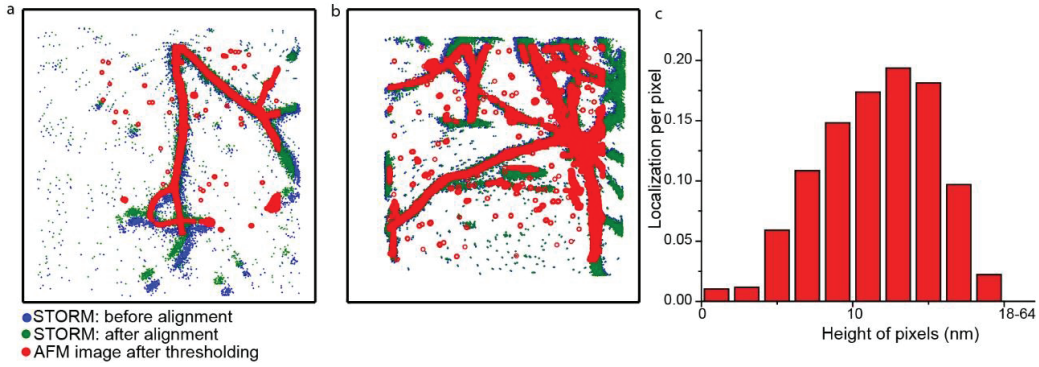

Supporting Figure 3.4 Alignment process for STORM images of Figure 3.3k (a) and Supporting Figure 3.3 (b) The localizations obtained from STORM imaging (blue) is transformed by a 2D affine transform to obtain the coordinates (green) that are better aligned with the structure in the AFM image (red). The parameters of the transform are estimated by the procedure mentioned in the Supporting material text. (c) Histogram showing the distribution of localizations per area of a particular height as measured by AFM. By correlating dSTORM data and AFM data as shown in Figure 3.4g, a height value was assigned to pixels of the dSTORM image. The sum of localizations occurring within a bin (bin size 2 nm) was divided by the total number of pixels falling into that particular bin size. Most localizations relative to the number of pixels appeared at heights between 8 nm - 14 nm, which corresponds to the measured physical height of F-actin, while very few localizations were detected on the level of the substrate (0 - 2 nm). This histogram is a quantitative representation of the correlation of dSTORM and AFM data.

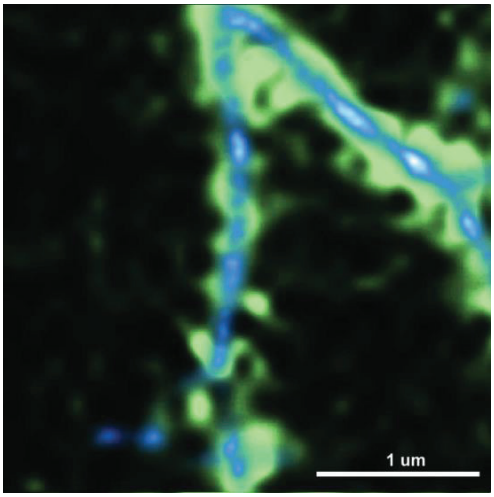

Supporting Figure 3.5 Overlay of dSTORM (blue) image and total internal reflection fluorescence (TIRF) image (green) of the same area as shown in Figure 3.4g. The TIRF image shown here was used for the analysis in Figure 3.4e & f.

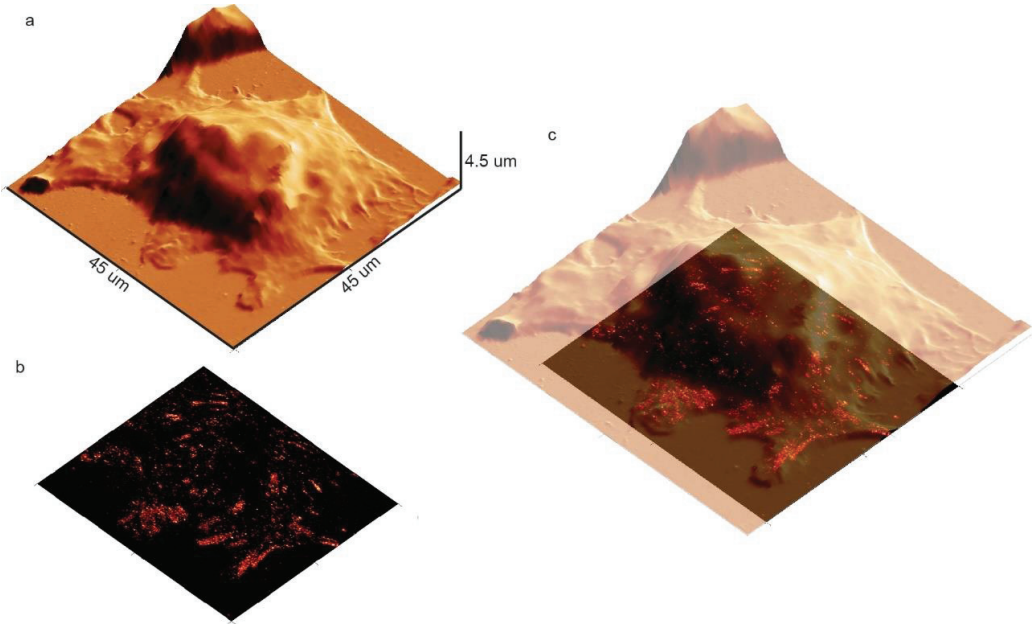

Supporting Figure 3.6 Correlative AFM/PALM image of a fixed mammalian cell (mouse embryonic fibroblast (MEF) cell) expressing the fusion protein paxillin-mEOS2. (a) 3D render of AFM image with error channel as mask. (b) PALM image. (c) Correlated AFM and PALM image. Details describing the sample preparation are discussed in the text of the Supporting material.

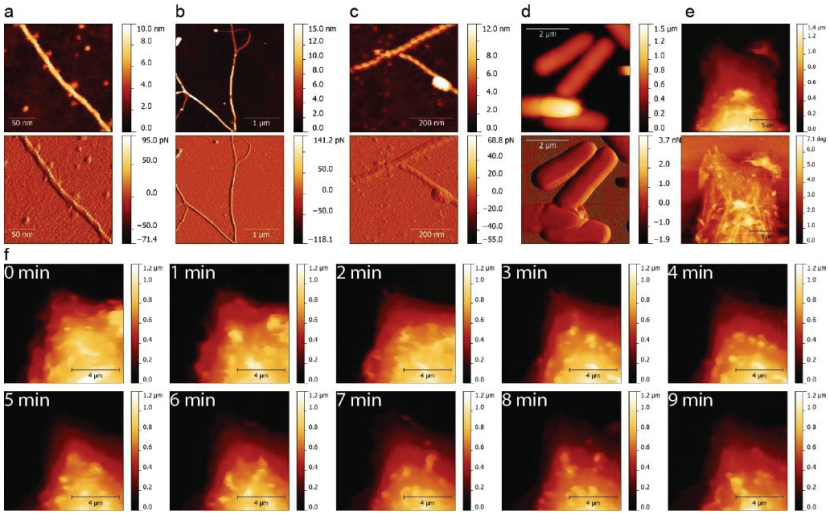

Supporting Figure 3.7 2D AFM height images of 3D representations shown in main figures. (a) Corresponds to AFM image shown in Figure 3.2a. (b) Corresponds to AFM image shown in Figure 3.3i & Figure 3.4g. (c) Corresponds to AFM image shown in Figure 3.3j. (d) Corresponds to AFM image shown in Figure 3.4j. (a-d) Top height image, bottom peak force error image. (e) Corresponds to AFM image shown in Figure 3.5a. Top height image, bottom phase image. (f) Corresponds to AFM time-resolved images shown in Figure 3.5b.

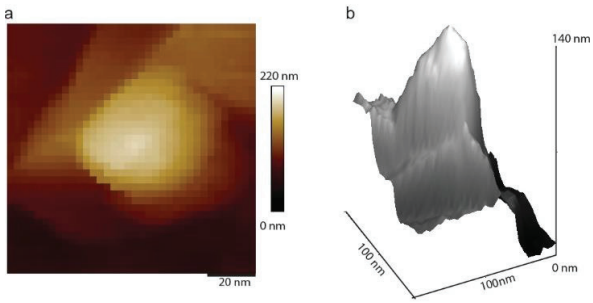

Supporting Figure 3.8 Tip reconstruction as obtained by Nanoscope Analysis software of the AFM tip used for imaging F-actin filaments shown in Figure 3.3 & Figure 3.4. The tip shape was reconstructed from an image of a tip characterization sample. (a) 2D height image. (b) 3D representation of tip reconstruction.

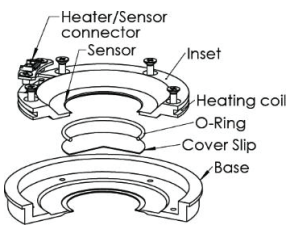

Supporting Figure 3.9 Schematic of the home-built glass coverslip holder used to keep the live-cell CHO-K1 sample at 37°C. The temperature was controlled with TC-2-80-15 (Bioscience Tools).

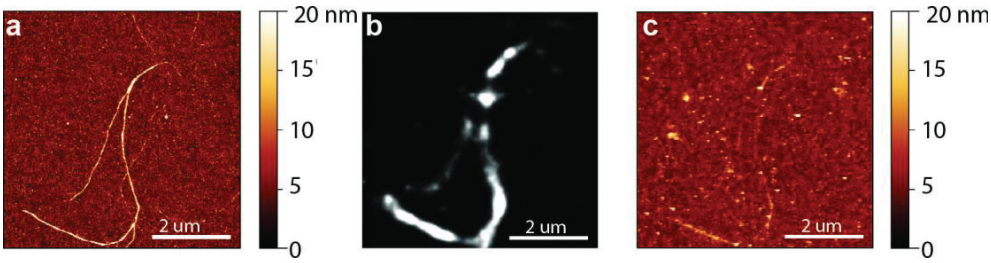

Supporting Figure 3.10 Effect of dSTORM measurement on actin filament integrity. (a) AFM image of F-actin labelled with phalloidin-atto488 before dSTORM. (b) dSTORM image acquired as described in the methods, but no beads were used for dSTORM. Reconstruction was done using the software thunder-STORM. (c) After dSTORM image was acquired another AFM was recorded. Parts of actin filaments disintegrated.

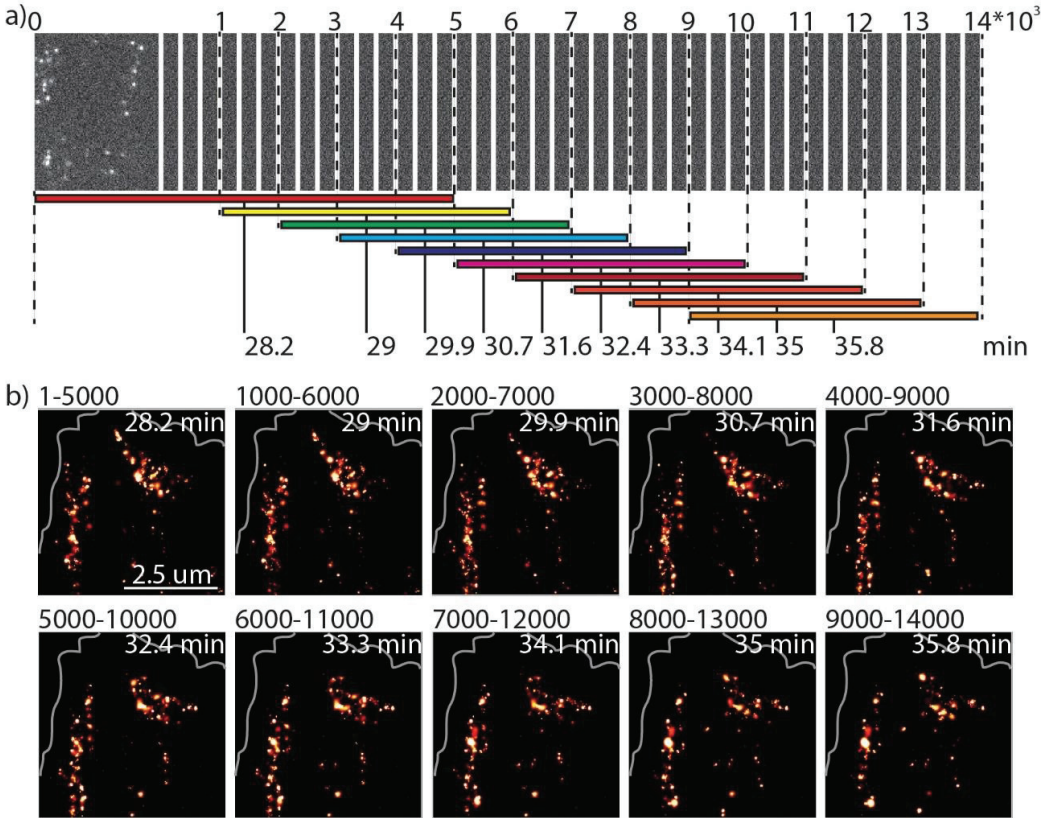

Supporting Figure 3.11 Time-resolved PALM images constructed from 5000 frames with a running average approach. (a) Schematic showing the time-resolved PALM image reconstruction. Each PALM image is a reconstruction out of 5000 frames. Between each consecutive PALM image there is an offset of 1000 frames. The time reported indicates the time at which the middle frame of the respective PALM frame has been acquired. (b) Time-resolved PALM series. On top of each PALM image the number of frames used for its reconstruction is indicated. The outline of the cell is marked in gray. This time-sequence was used for the Supporting movie 1.

Chapter 4 Bacterial division governed by mechanical properties

This a verbatim copy of a manuscript for publication in a peer-reviewed journal.

4.1 Abstract

Bacteria dividing by a mechanical rupture of the outer cell envelop manifest specific physiological and morphological features. The main features such bacteria share is the sudden separation of sibling cells happening in milliseconds. It is speculated that at the place of the septum increased mechanical stress occurs before the separation.(*48*) Besides the action of hydrolytic enzymes(*49*), mechanical forces are another, possibly essential, contributor to resolving the cell wall connection of sibling cells. After bacteria separate upon mechanical stress imposed, new cell envelop material and scars at the site of rupture can be observed.(*50*) Bacteria often change their positions relative to each other as a consequence of released mechanical tension which in mycobacteria is commonly referred to as V-snapping.(*51-53*) Many bacteria show such features, suggesting that mechanical forces play an important role in the separation process of these bacterial species. We are using *Mycobacteria smegmatis*, a non-pathogenic relative of *Mycobacteria tuberculosis*, as a model organism to study the mechanical implications of bacterial separation.

By atomic force microscopy (AFM) we can directly measure the mechanical stress imposed on the cell wall at the septum. Our measurements show that during septation the tensile stress at the septum increases remarkably and is resolved only as sibling cells physically separate. This separation happens within milliseconds and is quicker than a sole hydrolytic enzymatic activity would achieve. Moreover, by specifically applying additional mechanical load on the septum we can actively change the stress imposed on the cell wall connecting sibling cells. Thereby, premature physical separation of sibling cells can be induced without lethal damage. Hence, we show that the physical separation of daughter cells is governed and mediated by mechanical forces exerted on the cell envelop at the septum and is crucial to (the timing of) bacterial separation.

4.2 Results

It is already known that mycobacteria build a new septal wall at midcell in the process of division before the daughter cells physically separate.(*54, 55*) Electron microscopy data showed that the peptidoglycan branches off from the cell envelop at midcell and grows inward to build the new poles during septal biogenesis. (*56*) This is as well the case for *M.leprae(57), M.vaccae(52)* and *M.tuberculosis(53)* and is fundamentally different to the way other rod-shaped bacteria such as *Escherichia coli* divide, where constriction and septation occur concomi-

tantly.(*58*). The resolution of the connection between the two daughter cells is believed to be initiated by the action of hydrolytic enzymes as has been shown by fluorescent microscopy studies. A mycobacterial strain depleted of RipA, a peptidoglycan hydrolase, grew in long, branched chains unable to separate from its sibling cell.(*49*) Besides the essential hydrolytic activity of RipA little is known about the physical separation of sibling cells.

We are using the atomic force microscope (AFM) to show how mechanical cues influence this cell separation process. The AFM, a mechanical microscope, allows live cell imaging of bacteria while at the same time mechanical properties of the sample can be measured at the nanoscale. Moreover, we can use the AFM to manipulate the sample by specifically applying mechanical load.

Figure 4.1a shows a sequence of high-resolution AFM images during the last stages of the cell cycle of *M.smegmatis*. The first sign of a division visible by AFM is the appearance of a pre-separation furrow, a small constricted ring around the cell indicating the future division site which in average appears about 70 minutes before the sibling cells actually separate. A feature very similar to the pre-separation furrow has been imaged by SEM on *S.aureus(50)* and *M.vaccae(52)* or by AFM on *M.bovis BCG*(*59*). It appears long before the separation of the daughter cells and becomes more pronounced as the cell cycle progresses (Figure 4.1a, 0 min - 56 min). Other than that the cell envelop remains unchanged during all this time. Only as the cell separate and the outer cell envelop breaks, the two parts shifted apart manifesting a deep cleft at the position where the pre-separation furrow was. (Figure 4.1b & c). The new poles which have been developed within the common cell envelop prior to the separation are exposed after division (Figure 4.1d) and the scar of the ruptured cell envelop are clearly visible. Such circumferential scars of the broken peptidoglycan layer on each of the daughter cell have been reported on *S.aureus(50) M.vaccae(52)* and *M.tuberculosis(53)* as well, suggesting separation might happen in a similar way in these cells.

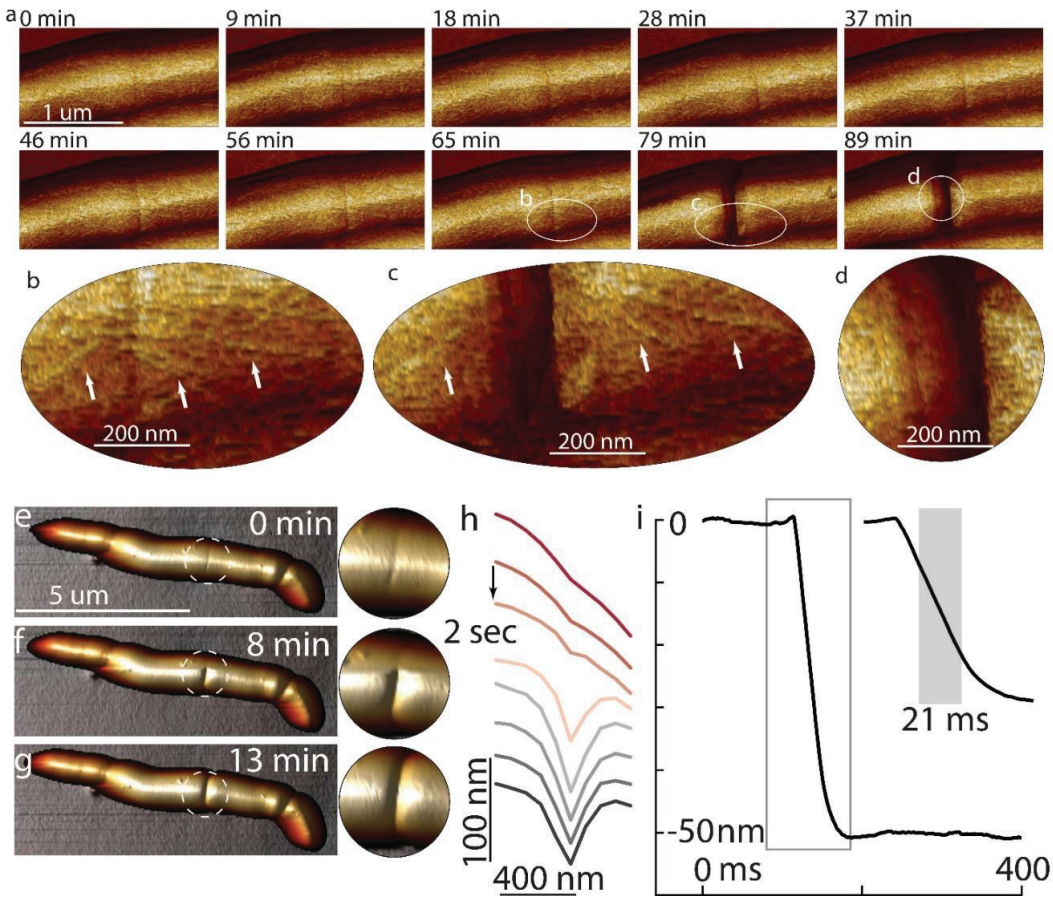

Figure 4.1 Division of M.smegmatis imaged by AFM. a) AFM image series. The pre-separation furrow at midcell becomes more pronounced as the cell cycle progresses. The division happens between 65 min and 79 min (zoom-ins shown in b & **c**). After the division the two cell envelops of the daughter cells initially move away from each other for about 200 nm in opposite directions. In the next minutes the distance does not change remarkably anymore. d) The new poles were already formed before the cell envelopes separated. Constriction and septal growth do not occur concomitantly. e-g) consecutive AFM images of dividing M.smegmatis. f) As the AFM was scanning from the top down the bacteria divided exactly while scanning over the septum (magnified region) and was divided entirely in the next image (h). Line profiles extracted from f show the appearance of the division cleft from one scan line to the next, 2 seconds later. i) Constantly measuring the height at one point on the septum at 1 ms temporal resolution shows the rapid transition at which the division snap occurs. 50% of the total height decrease (grey area) is reached in 21 ms.

Between the appearance of the pre-separation furrow and the cell separation we have never observed any appreciable stretching of the width of the pre-separation furrow, nor have we observed any partially cleaved cells. This suggests that the process of cell separation occurs much faster than the temporal resolution of our AFM images (ca 5 min/image). Yet, while scanning across a septum by AFM we saw that the separation of bacteria is happening very abruptly. Figure 4.1e-g shows a sequence of 3 AFM images of a dividing *M.smegmatis* with the pre-separation furrow region magnified. In the first image the pre-separation furrow is well visible (Figure 4.1e), while in the last one (Figure 4.1g) the cell is already fully separated. The separation coincidentally happened while scanning the middle image from top to bottom. Within the temporal resolution from one scan line to the next (in this experiment in less than 2 seconds), the

cell goes from the pre-separation furrow to the separated state, (Figure 4.1f). The pre-separation furrow deepened abruptly and the two daughter cells separated (Figure 4.1h). To increase the temporal resolution of our measurement to 1 ms we then constantly measured the height on top of a septum without any lateral scanning. We found that the height suddenly dropped by approximately 50 nm within a few tens of milliseconds. In Figure 4.1i, 50 % of the height drop is achieved in 21 milliseconds (grey area). Such rapid and drastic morphological changes are unlikely the sole product of hydrolytic activity on the peptidoglycan layer connecting the two sibling cells.

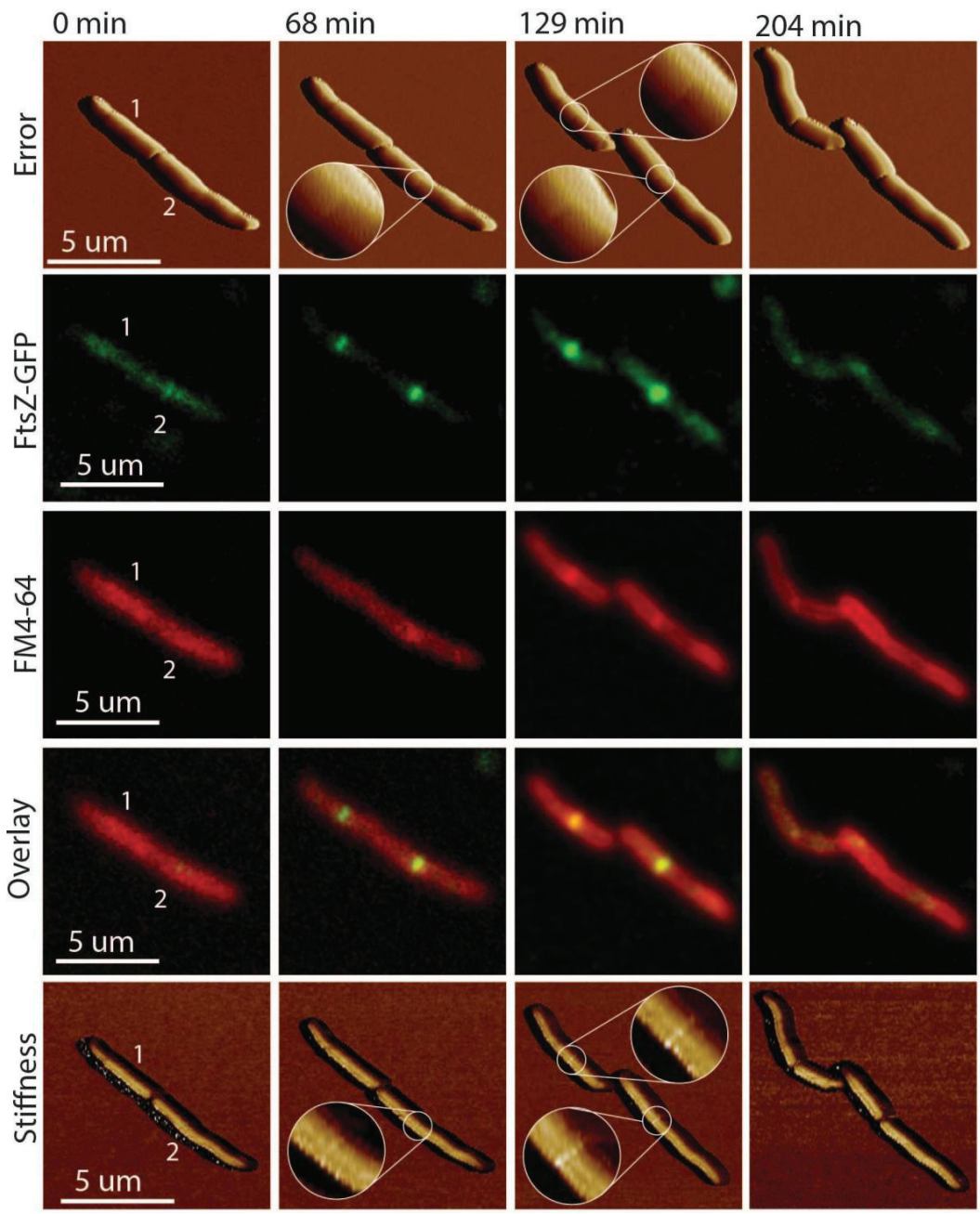

Figure 4.2 Correlated AFM and fluorescence microscopy of FtsZ and bacterial membrane. 0 min: FtsZ is not yet coalesced to midcell and pre-separation furrow has not appeared yet. 68 min: FtsZ of bacterium 1 coalesced to the future division site and appears as a band with a peaks on each side. FtsZ of bacterium 2 appears as a brighter single spot. The plasma membrane stain of the bacterium 2 is already increased at the septum of bacterium 2. The pre-separation furrow appeared on the surface, the stiffness has not changed remarkably yet. 129 min: FtsZ appears as a single bright spot in both bacteria, the plasma membrane is building up in both bacteria. The stiffness of the material spanning the septum appears stiffer. 204 min: Both bacteria divided.

To follow intracellular processes such as the septation and link it to the morphological changes on the surface we conducted combined AFM and fluorescence microscopy experiments using

the same setup as reported earlier.(*60*) The formation of the pre-separation furrow is reminiscent of the formation of the FtsZ ring as they both appear long before the separation at the future division site. FtsZ is a protein that polymerizes into a ring-like structure at midcell.(*61*) It is believed to be one of the earliest events in defining the position of division site placement and the constriction of the FtsZ ring is believed to be essential for division. To test how FtsZ dynamics temporally and spatially correlate with the appearance of the pre-separation furrow we used a bacterial strain expressing an FtsZ-GFP fusion protein described earlier.(*62*) To follow the formation of the septum at the same time the bacteria were stained with the plasma membrane stain FM4-64. Correlated fluorescence and AFM imaging results showing FtsZ-GFP, the plasma membrane, and AFM data over the course of the cell cycle are summarized in Figure 4.2. Two sibling bacteria of which the bottom one (bacterium 2) is slightly ahead in its cell cycle of the upper one (bacterium 1) are shown. The pre-separation furrow of bacterium 2 appears in the error channel after 68 minutes while for bacterium 1 it has not appeared yet. Interestingly, FtsZ-GFP seems to be coalesced in one bright spot in the bacterium with the pre-separation furrow, while bacterium 1 doesn't manifest the pre-separation furrow yet and the FtsZ-GFP signal doesn't appear centrically concentrated along the short axis and is less intense. This could mean that the FtsZ ring in bacterium 2 is constricted while in bacterium 1 it is still in the assembly process. At the same time as the pre-separation furrow appears, the plasma membrane starts to invaginate at midcell (FM4-64 at 68 min) suggesting that the formation of the septum has started in bacterium 2, but not yet in bacterium 1. Later on the pre-separation furrow formed on bacterium 1 as well (129 minutes, Error channel) and the septa are developed further (FM4-64). At 204 min both bacteria divided and the same situation as at the beginning (0 min) presents itself with the FtsZ which is disassembled. This data suggests that the constriction of the FtsZ ring and the formation of the septum at midcell come in close succession or even at the same time. The onset of these events is as well the time when the pre-separation furrow appears. Besides imaging the surface the AFM is capable of probing materials' properties. Recently developed force distance curve based AFM modes can measure the sample stiffness with nanometer resolution. The bottom line in Figure 4.2 shows the stiffness channel of the AFM measurement of the cell envelop. Interestingly, we observed an increased stiffness at the septum (129 minutes) before the separation of the cells. To probe the stiffness at the septum more precisely we measured the bacterium at a slightly elevated force (~5 nN). Between the formation of the pre-separation furrow and the separation the stiffness at the septum increased steadily. (Figure 4.3a) By constantly scanning across the septum as the cell is dividing we found that the stiffness at the septum increases gradually at the beginning (of up to more than 3-fold the bulk value) and eventually reaches a plateau after about 15 - 20 minutes (Figure 4.3b). Typically just before the separation the stiffness decreases very slightly. The fact that the stiffness at the septum increases as the cell proceeds in its cell cycle combined with the observation that broken cell envelops shift apart from each other once the sibling cells separate indicate that the apparent stiffness is a result of increased tensile stress in the cell wall at the septum. Once the tensile stress in the region of the pre-separation furrow is higher than the ultimate tensile strength of the cell wall material, the sibling bacteria separate. If this is the case it should be possible to induce a premature separation of sibling cells by either introducing structural damage or additional mechanical load at the septum, thereby increasing the tensile stress. This should result in a physical separation all around the circumference of the cell and not only where the damage has been intro-

duced and the new poles should be exposed. We used the AFM tip to specifically apply mechanical load on top of the bacterium at the position of the pre-separation furrow. The average time from the formation of the pre-separation furrow to cell separation was about 70 minutes. Figure 4.4 shows sequences where the division at the septum was induced 25 minutes (a) or 15 minutes (b) after the appearance of the pre-separation furrow, respectively. Before the separation was induced an increased stiffness could already be measured at the septum (Figure 4.4a, 23 min post-PCF). As additional mechanical load was imposed by the AFM tip at the septum (FD curve) the bacterial separation was induced. The scar where the break happened is clearly visible (30 min post-PCF). The bacteria physically separated and even reoriented, suggesting that they are not connected anymore internally (35 min post-PCF). In the sequence below (Figure 4.4b) the division has been induced already 15 minutes after the pre-separation furrow appeared. The stiffness at the septum (9 min post-PCF) has not yet increased as much as in Figure 4.4a (23 min post-PCF). Applying mechanical load (FD curve) on the septum introduced a local damage to the cell envelop rather than a break of the material all along the pre-separation furrow (18 min post-PCF). This could suggest that the new poles have not yet been developed entirely and the septum was still forming. Moreover, the bulk stiffness of the bacterium dropped entirely after some time (37 min pre-PCF vs. 36 min post-PCF), while the bacterium that has not been damaged (lower bacterium) kept its turgor pressure constant. This suggests that the damage introduced at the septum was leading to the loss of the turgor pressure and killed it, further strengthening the assumption that the new poles have not yet been entirely developed. This pressure drop on the other hand did not occur in the sequence shown in Figure 4.4a where the bacteria survived the induced division. These results show that just by adding mechanical load on the septum a premature separation of sibling cells can be induced. Bacteria only survive this prematurely induced separation if the new poles are already formed and cytokinesis is completed.

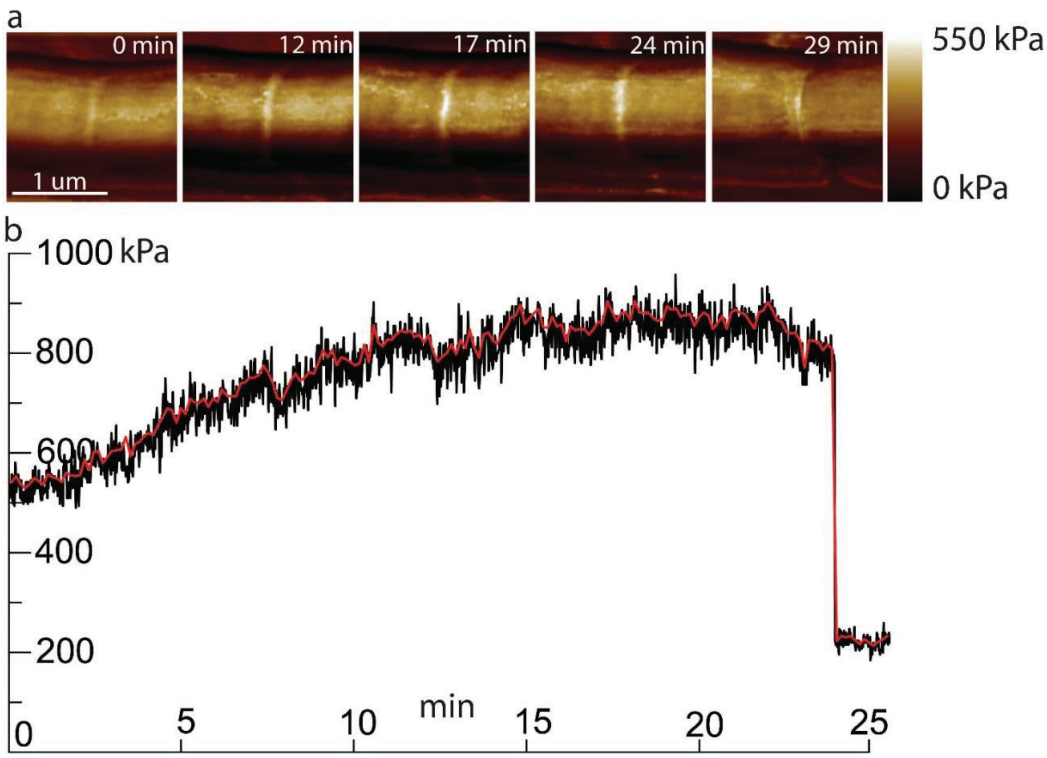

Figure 4.3 Apparent stiffness increases as the cell cycle proceeds. a) The stiffness of the cell envelop spanning across the septum increases after the pre-separation furrow is observed as the cell cycle progresses. b) Constant measurement of the stiffness across the septum shows an initial steady increase in stiffness till a certain plateau is reached. Typically, just before the division snap occurs the stiffness decreases slightly.

The sibling cell separation is dependent on the ultimate tensile strength and the tensile stress imposed on the material. Once the stress is higher than the strength the bacteria separate within milliseconds. The tensile stress is building up as the septum is forming and still increases after cytokinesis. The fact that the stiffness typically decreases just slightly before the separation (Figure 4.4b) could mean that hydrolytic enzymes acting on the peptidoglycan connection between the sibling cells are responsible for the weakening of the cell envelop at the septum. This would decrease the ultimate tensile strength, which we measure as a decrease in the apparent stiffness. It has been shown that if hydrolytic enzymes are lacking at the septum due to a genetic modification the bacteria do not separate.(*49*) This suggests that the maximal tensile stress that can naturally be built up is not enough to induce a separation on its own. The weakening of the peptidoglycan layer specifically at the septum is necessary. This could be a mechanism that helps the cell to prevent premature separations as tensile stress is built up. *M.smegmatis* did not manifest remarkable structural defects at the septum which for *S.aureus* seemed possible trigger points for a mechanical crack to propagate.(*48*) It is much more likely for *M.smegmatis* that the material connecting the two daughter cells is being hydrolysed from the inside out without defects being presented on the surface of the cell envelop.

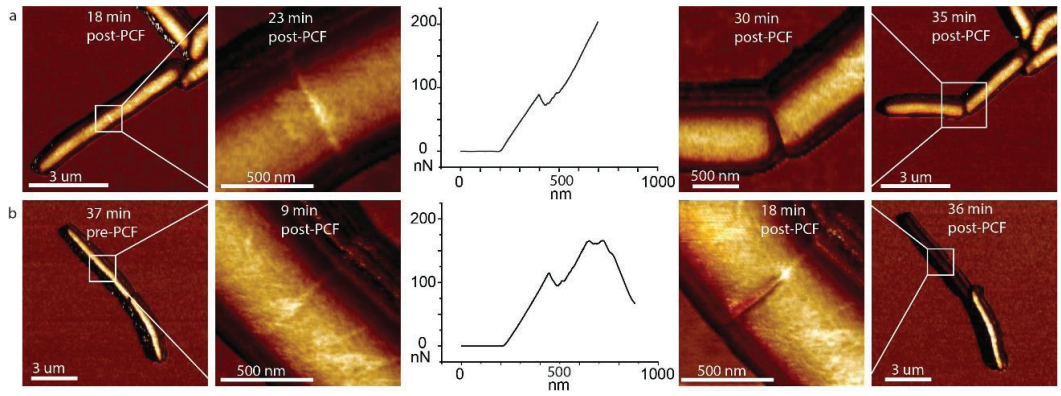

Figure 4.4 Induced division by mechanical point load on septum. a) The bacterium started septation and increased stiffness is observed at the septum (18 min post-PSF). 23 min post-PSF: Zooming-in to septum to induce division by applying force with cantilever. 25 minutes after the appearance of the pre-separation furrow bacterial division was induced. (FD-curve) 30 min post-PSF: The bacteria divided induced by the AFM. 35 min post-PSF: Both bacteria survive and keep their internal turgor pressure. b) The bacterium is growing the turgor pressure is normal (37 min pre-PSF). 9 min post-PSF: 9 minutes after the pre-separation furrow appeared, the stiffness is only slightly increased at the place of the septum. 15 minutes after the appearance of the pre-separation furrow bacterial division was induced. (FD-curve). 18 min post-PSF: The layer connecting the two future daughter cells was punched at the developing septum by the AFM. 36 min post-PSF: The bacterium where division was induced did not survive and appears much less stiff, while the bacterium where no AFM force was applied (below) is still living.

From TEM images we know that the peptidoglycan layer branches off at midcell and forms a septum before separation of the sibling cells.(*56*) Additionally, fluorescent studies showed that different proteins important for synthesizing the different cell envelop layers localize to the septum before separation. For example Wag31, which is an essential protein that plays a key role in localized peptidoglycan synthesis in mycobacteria.(*63*) Moreover, studies showed that nascent peptidoglycan labelling fluorescent vancomycin strongly colocalized with Wag31 localization.(*63, 64*) Therefore, it is conceivable that new peptidoglycan is already synthesized once the new poles are formed but the sibling cells are still connected. Besides Wag31 it has been shown that the fatty acid synthase-II (FAS-II) core as well as the mycolic acid transporter MmpL3, a transmembrane RND-family transporter, are located at the septum prior to division. Mycolic acids, which constitute the major lipid component of the envelope and form the external mycomembrane, may be synthesized at the septum in order to be transported, probably by MmpL3, to the external mycomembrane. (*65-67*) Moreover, studies using fluorescent protein fusions showed that the terminal synthetic enzymes for peptidoglycan, arabinogalactan and mycolic acids colocalize at the septum and at a subpolar elongation zone.(*68*) All of this suggests that the new poles at the septum at the time of separation of daughter cells already contain all the layers of the cell envelop and elongation might even already start to some extent. However, since the physical space is limited at the septum freshly synthesized material is accumulating within the space of the two peptidoglycan walls before sibling cells separate. This will eventually lead to a pressure inside this confined space which would result in a tensile stress acting on the peptidoglycan connecting the two daughter cells. In AFM measurements this tensile stress shows up as increased stiffness. The increasing tensile stress coupled with the activity of hydrolases specific to the septum will eventually lead to a rupture of this physical connection and to the physical separation.

4.3 Methods

Bacteria. *Mycobacterium smegmatis* mc^{2}155 (wild-type) and derivative strains were grown in Middlebrook 7H9 liquid medium (Difco) supplemented with 0.5% albumin, 0.2% glucose, 0.085% NaCl, 0.5% glycerol, and 0.05% Tween-80. Cultures were grown at 37°C to mid-exponential phase (OD_{600} ~ 0.5). Aliquots were stored in 15% glycerol at -80°C and thawed at room temperature before use; individual aliquots were used once and discarded.

FtsZ-GFP Reporter. The open reading frame (ORF) encoding *M. smegmatis* FtsZ was PCR-amplified using primers MsmftsZ-F (gctagcatgaccccccgcataactacctcg) and MsftsZ-R (ggactagttcctcctgatcctcctccacctgaaccaccaccacctgaaccaccaccacctgaaccaccggtgtgccgcatgaagggcg) with genomic DNA as the template. The underlined sequence in primer MsmftsZ-R represents the linker sequence encoding four repeats of Gly-Gly-Ser-Gly-Gly. The amplicon was ligated into vector pCR2.1 (Invitrogen) and verified by DNA sequencing, then excised as an *Nhe*I-*Spe*I fragment and ligated into the unique *Nhe*I site in the *attB*-integrating vector pND250 (gift from N. Dhar), which encodes a hygromycin resistance marker. The resulting plasmid (pND275) expresses *ftsZ-gfp* (in-frame fusion) from a strong anhydrotetracycline (ATc)-inducible promoter. pND275 was electroporated into *M. smegmatis* and transformants were selected by plating on solid medium containing hygromycin.

Bacteria deposition. Coverslips were prepared by mixing polydimethylsiloxane (PDMS) (Sylgard 184, Dow Corning) at a ratio of 15:1 (elastomer : curing agent). Air bubbles in the mixture were removed under negative pressure for 15 minutes. The PDMS mixture was dropped onto a 22 mm diameter glass coverslip (VWR) and spin-coated at 8,000 rpm (SUSS MicroTec Lab-Spin6) (*69*) for 30 seconds. PDMS-coated coverslips were baked at 80°C for 10 minutes before use. Bacteria grown to logarithmic phase were directly transferred onto the coverslip mounted in a home-built coverslip heater with integrated heating. After 15-30 minutes, non-adherent bacteria were removed by extensive washing with 7H9 medium.

Correlated Fluorescence and Atomic Force Microscopy. Correlated fluorescence and AFM images were acquired on the system described previously (*60*). Briefly, fluorescence images were acquired with an EMCCD iXon Ultra 888 camera (Andor) mounted on an IX73 inverted optical microscope (Olympus) equipped with an RMS100x-PFO oil immersion objective (Olympus). Illumination was provided by an MLC monolithic laser combiner (Agilent) using the 488 nm laser coupled to an optical fiber at 5 mW output power with appropriate optical filters. For combined FM4-64/FtsZ-GFP imaging the emission light was separated from the illumination light using the EGFP excitation filter (F39-483, AHF Analysetechnik, Germany) and dichroic (F38-495, AHF Analysetechnik, Germany). An optical system (DV2, Photometrics) equipped with a dichroic mirror (T565lpxr, Chroma Technology) was placed between the EMCCD camera and the microscope frame to split the red and green emission light each on one half of the EMCCD chip. Additionally an EGFP emission filter (F37-528, AHF Analysetechnik, Germany) or a TxRed emission filter (F37-624, AHF Analysetechnik, Germany) was placed into the light path. The AFM was mounted on top of the inverted microscope and images were acquired with a Dimension FastScan head (Bruker) using ScanAsyst fluid cantilevers (Bruker) with a nominal spring constant of 0.7 N m^{-1} in peak force tapping mode at a setpoint < 2 nN and typical scan rates of 0.5 Hz. The samples were

maintained at 37°C in 7H9 liquid medium heated by a custom-made coverslip heating holder controlled by a TC2-80-150 temperature controller (Bioscience Tools). The concentration of FM4-64 in the medium was at 0.2 µg/ml.

Image and data processing. AFM images were processed with standard scanning probe image processing software (Gwyddion or Nanoscope Analysis). Time-resolved stiffness increase was recorded by constantly scanning the same line across the septum at 5 nN peak force septoint. Of each line, the maximal value was determined using Matlab.

Chapter 5 Inherited cell-surface wave-troughs mark future division sites in mycobacteria

This is a verbatim copy of a manuscript that will be submitted to a peer-reviewed journal. Haig Eskandarian, Pascal D. Odermatt, Joëlle Ven, Adrian P. Nievergelt, Neeraj Dhar, John D. McKinney, Georg E. Fantner. Inherited cell-surface wave-troughs mark future division sites in mycobacteria.

My contribution to the project was taking the data of the correlated fluorescence microscopy and AFM and analysis thereof (Figure 5.3, supplementary figures, and supplementary movies).

5.1 Abstract

Cell division is tightly controlled in space and time in order to maintain cell size and ploidy within narrow bounds. In bacteria, the canonical Minicell (Min) and nucleoid occlusion (Noc) systems together ensure that division is restricted to midcell after completion of chromosome segregation (*70*). It is unknown how division site selection is controlled in bacteria that lack the Min and Noc systems, including mycobacteria responsible for tuberculosis and other chronic infections (*54*). Here, we use correlated optical and atomic force microscopy (*60, 71*) to demonstrate that morphological landmarks (waveform troughs) on the undulating surface of mycobacterial cells correspond to future sites of FtsZ contractile ring formation and cell division. Newborn cells inherit wave-troughs from the (grand)mother cell and ultimately divide at the centermost wave-trough, making these morphological features the earliest known landmark of future division sites. In cells lacking the chromosome partitioning (Par) system, missegregation of chromosomes is accompanied by asymmetric cell division at off-center wave-troughs, resulting in the formation of anucleate cells. These results demonstrate that inherited morphological landmarks and chromosome positioning together restrict mycobacterial division to the midcell position.

5.2 Results and Discussion

We used time-lapse atomic force microscopy (AFM) (*71, 72*) to track cell growth and division in *Mycobacterium smegmatis*, a non-pathogenic relative of *Mycobacterium tuberculosis* (Figure 5.1A; Supporting Figure 5.2). Unexpectedly, we found that the cell surface undulates in a periodic fashion along the long axis (Figure 5.1B & C) with an average wavelength of ~ 1.8 μm (Supporting Figure 5.3). These morphological features are too small (~ 100 nm from wave-crest to wave-trough) to resolve by conventional optical microscopy. The number of waves increases

with increasing cell length while the wavelength remains relatively constant, revealed by inducing cells to grow as elongated filaments with ciprofloxacin (Figure 5.1E). Conversely, blocking cell elongation with isoniazid inhibits the formation of new wave-troughs (Supporting Figure 5.4). In time-lapse series, we found that centrally located wave-troughs correspond to future sites of cell division (Figure 5.1C & D). Remarkably, wave-troughs that mark future division sites are already present at birth; they form near the cell poles in the mother, grandmother, or great-grandmother cell and are passed on to the daughter cells at division (Figure 5.2A). On average, division at a wave-trough occurs 1.5 generations after the trough is first established (Figure 5.2B), which corresponds to 250 minutes for cells growing with an average interdivision time of 190 minutes (Figure 5.2C). As wave-troughs age, they gradually shift position towards the cell center, presumably because mycobacteria grow exclusively by sub-polar addition of new cell wall material (Figure 5.2A) (*68*). Inherited wave-troughs localize to positions near midcell approximately 150 minutes prior to cell separation.

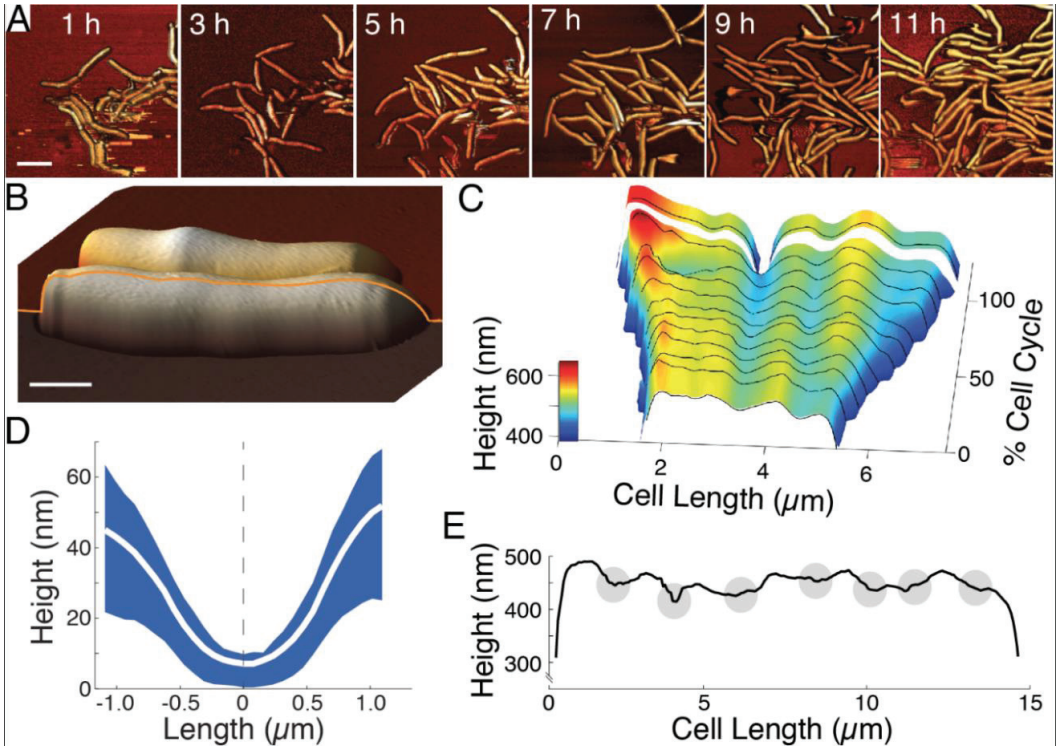

Figure 5.1 Mycobacterial cells divide at cell-surface wave-troughs. (A) Time series of top view 3D representation of AFM height images overlaid with AFM phase images for wild-type M. smegmatis cells. Scale bar, 4 µm. (B) Three-dimensional surface topology of live bacteria. Yellow trace of the cell profile highlights the undulating mycobacterial surface morphology. Scale bar, 1 µm. (C) Kymograph of the cell surface height of a representative cell from birth to division, showing that division occurs within a central wave-trough. (D) Averaged surface height around the future site of cell separation (n = 270). White line depicts the average height within a range ± 1 µm in each direction of the separation site. The blue background depicts the variation (25th and 75th percentiles) in surface height. (E) Longitudinal height profile of a single cell treated with ciprofloxacin, illustrating the formation of multiple wave-troughs (grey circles) in filamented cells.

We constructed a microscope that combines optical (fluorescence) and low-noise AFM-based imaging (*60*). Correlated AFM and fluorescence time-lapse imaging of single cells revealed a sequence of morphological and molecular events leading up to cell division. Formation of the FtsZ contractile ring at midcell is thought to be the earliest event in specification of the cell division site in rod-shaped bacteria(*70, 73*). However, in cells expressing FtsZ tagged with green fluorescent protein (GFP), we found that the FtsZ ring forms within a pre-existing wave-trough near midcell. In cells growing with an average interdivision time of 190 minutes, formation of the pre-divisional wave-trough precedes formation of the FtsZ ring by 120 minutes, on average.

Formation of the FtsZ-GFP ring near midcell (Figure 5.3A) is followed about 30 minutes later by appearance of a co-localized “pre-separation furrow” (~ 50 nm wide and ~ 10 nm deep) in the AFM image, a distinctive topological feature that is too small to detect by optical microscopy (Figure 5.3A, black arrows). This feature might correspond to the previously reported “cell wall contractile ring” in *Mycobacterium* sp. JLS, although the latter was described as a cell-surface protrusion rather than an indentation (*74*). The pre-separation furrow appears prior to the early stages of pre-division septum formation, which we visualized by staining the cell membrane with the fluorescent dye FM4-64 (Figure 5.3B; Supporting Figure 5.5). These events precede cytokinesis by ~ 20 minutes in cells expressing the cytokinetic marker Wag31-GFP (Figure 5.3C). Cytokinesis is followed by a lag period (~ 40 minutes) before physical separation of the sibling cells, signaled by an abrupt deepening (~ 100 nm in depth) of the pre-separation furrow (Figure 5.3).

Taken together, these observations suggest a sequence in which the earliest event in cell division is formation of a pre-divisional wave-trough in the mother, grandmother, or great-grandmother cell, which is inherited by the daughter cell at birth. All subsequent events take place in the daughter cell: FtsZ ring formation within the center-most wave-trough, formation of a shallow pre-separation furrow, initiation of septum formation, cytokinesis, and separation of sibling cells (Figure 5.3D).

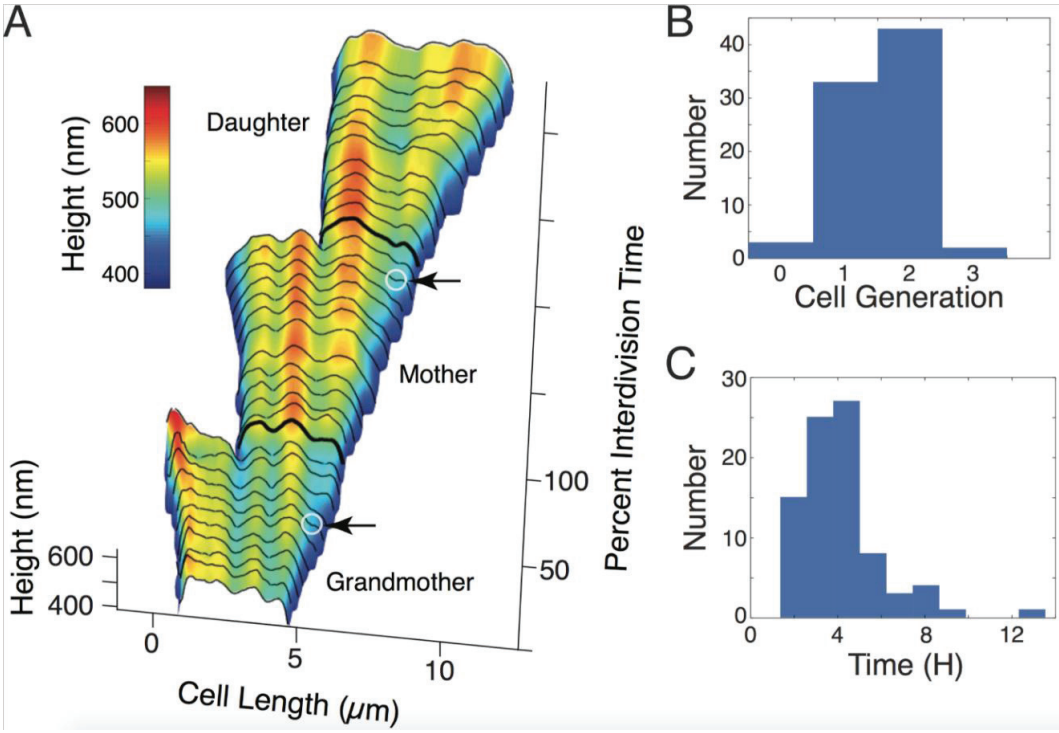

Figure 5.2 Wave-troughs are inherited from the (grand)mother cell. (A) Kymograph of the cell height of one cell lineage over three consecutive generations (bottom to top). A wave-trough formed in the grand-mother cell (arrow) becomes the division site in the mother cell. Similarly, a wave-trough formed in the mother cell (arrow) becomes the division site in the daughter cell. (B) Distribution of generations from wave-trough formation to cell separation. The wave-trough wherein division occurs in the daughter cell (generation 0) is usually formed in the mother cell (generation 1), grandmother cell (generation 2), or great-grandmother cell (generation 3). (C) Distribution of time intervals from wave-trough formation to cell separation.

Most mycobacterial cells exhibit multiple wave-crests and wave-troughs at the time of division, yet only the center-most wave-trough is selected as the division site. We asked whether off-center wave-troughs could function as alternative sites of cell division in cells lacking the ParB chromosome-partitioning protein. Consistent with recent studies (*75, 76*), we found that Δ*parB* cells frequently undergo highly asymmetric cell divisions (Figure 5.4A). We found that the positions of these asymmetric cell divisions are not random along the long axis of the dividing cell; rather, they occur within off-center wave-troughs (Figure 5.4B & C; Supporting Figure 5.7). Divisions occurring at off-center wave-troughs are skewed towards the old or new cell pole (15% or 25%, respectively), with the remainder of divisions (60%) occurring at the center-most wave-trough. The average generational time interval between wave-trough formation and separation is reduced for Δ*parB* cells compared to wild-type cells due to division at off-center wave-troughs, which are younger in most cases than the inherited central wave-troughs (Supporting Figure 5.6).

Time-lapse fluorescence microscopy revealed that central divisions in Δ*parB* cells are associated with normal chromosome partitioning (Figure 5.4D). We have never observed divisions occurring

at a local DNA maximum along the cell length. Taken together with the observation that off-center divisions of Δ*parB* cells occur within off-center wave-troughs (see above), these results suggest that chromosomes might play an inhibitory role in determining which wave-trough is selected as the division site. We tested this idea by correlated fluorescence and atomic force imaging of cells treated with the DNA gyrase inhibitor, ciprofloxacin, which causes cells to form elongated filaments with multiple wave-troughs (Figure 5.4E, 1st time point). We found that when a pre-separation furrow appears in a ciprofloxacin-blocked cell, it corresponds spatially to a local DNA minimum along the cell length (Figure 5.4E, 2nd time point, arrows).

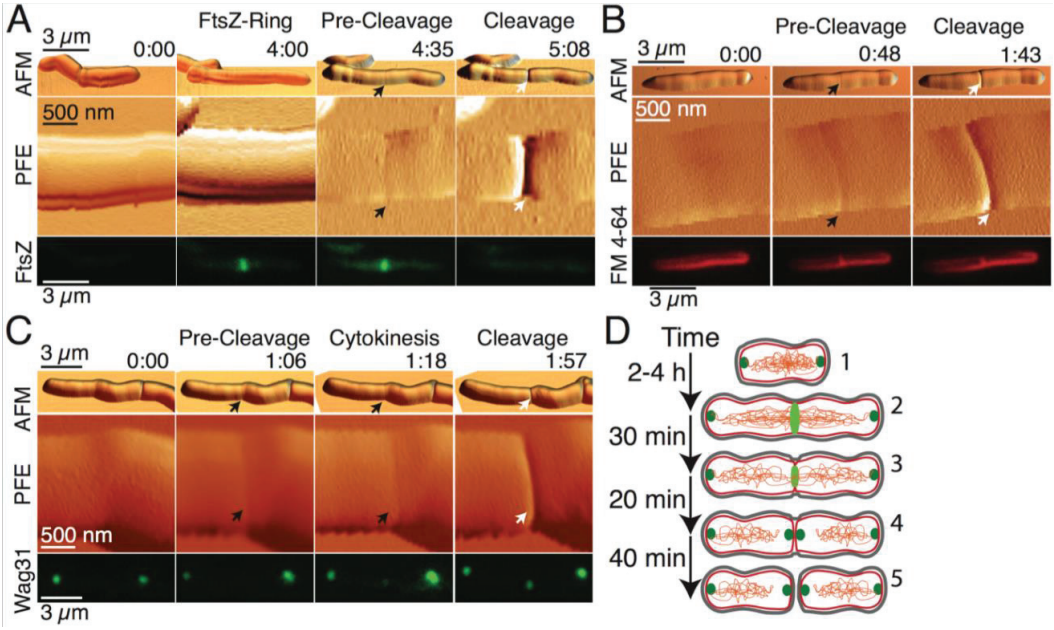

Figure 5.3 Sequence of events from cell birth to cell division. Cells were imaged by correlated AFM (upper and middle panels) and fluorescence microscopy (bottom panels). Upper panels depict 3D representation of AFM topography images. Middle panels depict AFM peak force error, which highlights the appearance of the pre-separation furrow (black arrows) and separation (white arrows). Numbers indicate time elapsed (hours:minutes) since birth. (A) Cells expressing FtsZ-GFP. The FtsZ ring co-localizes with the pre-separation furrow. (B) Cells with FM4-64-stained plasma membrane. Septum invagination co-localizes with the pre-separation furrow. (C) Cells expressing the cytokinesis marker Wag31-GFP. Cytokinesis is completed prior to cell separation. (D) Schematic of the sequence of events culminating in cell division. At birth, Wag31-GFP (dark green) localizes exclusively at the cell poles (1). FtsZ-GFP (light green) forms a circumferential ring within the central wave-trough (2-3). A pre-separation furrow then appears (indentation in the outer grey layer of the cell surface) and co-localizes with the FtsZ ring (3). Septum formation then proceeds and culminates in cytokinesis, which is marked by the appearance of a Wag31-GFP ring that co-localizes with the pre-separation furrow (4). Cell separation results in physical separation of the new-born sibling cells (5).

Previous studies using AFM (*74, 77, 78*), electron cryotomography (*79, 80*), or scanning electron microscopy (*52*) identified a variety of bacterial surface features associated with initiation or completion of cell division. To the best of our knowledge, inherited morphological features associated with division site selection have not been identified until now. Although the well characterized Min and Noc systems serve as negative regulators of FtsZ ring formation in evolutionarily divergent bacteria, emerging evidence suggests that these systems might not be responsible for

initial specification of the division site per se(*70*). Rather, these mechanisms function at later steps to help ensure that the FtsZ ring forms only at an appropriate place (distant from the cell poles and membrane-tethered DNA) and at the correct time relative to nucleoid segregation. What, then, are the mechanisms responsible for specifying the future division site? A recent study in Streptococcus pneumoniae demonstrated that the MapZ protein localizes as a circumferential band at midcell prior to assembly of the FtsZ ring, suggesting that it might play a role in division site selection (*81*). However, most bacteria, including mycobacteria, do not encode a MapZ homolog.

We observed that FtsZ ring formation, the earliest known event in division-site selection in rod-shaped bacteria, occurs within pre-existing wave-troughs on the undulating surface of mycobacterial cells. These wave-troughs correspond to local maxima of negative curvature along the cell's short axis and positive curvature along the cell's long axis. Localization of FtsZ rings to wave-troughs rather than wave-crests could act by reducing the mismatch between the negative curvature along the cell's short axis and the intrinsic curvature of FtsZ protofilaments (*82*). This mechanism would be analogous to the energetically favorable localization of cardiolipin patches at negatively curved polar regions of the cell (*83*). Molecules that preferentially localize to negatively or positively curved membranes might also direct recruitment of FtsZ to wave-troughs. In *E. coli*, several proteins localize to the negatively curved cell poles due to their intrinsic affinity for cardiolipin (*84*). In sporulating *B. subtilis* cells, preferential affinity for positively curved membranes directs the sporulation-specific protein SpoVM to the outer (convex) face of the developing forespore (*85*). Although mycobacteria do not encode SpoVM homologs, other proteins that target positively curved membranes could serve as beacons for FtsZ ring assembly at wave-troughs.

Although mycobacterial cell-surface wave-troughs serve as preferred sites for cell division, chromosomes also seem to play a negative regulatory role in division site positioning. Unlike wild-type cells, which always divide within a center-most wave-trough, mutant strains with defects in chromosome partitioning sometimes divide asymmetrically at an off-center wave-trough, but only when unpartitioned chromosomes are retained in the distal cell half. These observations suggest that mycobacteria might possess a mechanism analogous (but not homologous) to the Noc system to prevent cell division from occurring over unsegregated chromosomes. Like Noc, this mechanism might serve as a "failsafe" when chromosome replication or partitioning is severely impaired (*86*) (as in ParB-deficient cells) and may play little or no role in cells undergoing normal growth and division. Indeed, in wild-type mycobacteria nascent septa have been observed to form over chromosomes that are still in the process of segregating (*87*), which might be related to the degree of nucleoid compaction in these cells, as assembly of FtsZ rings over chromosomes has been observed in *E. coli* cells with diffuse nucleoids (*88*). Taken together, our observations suggest a bipartite model of division site selection, in which cell-surface wave-troughs are "licensed" sites for cell division and properly segregated chromosomes suppress division at off-center wave-troughs.

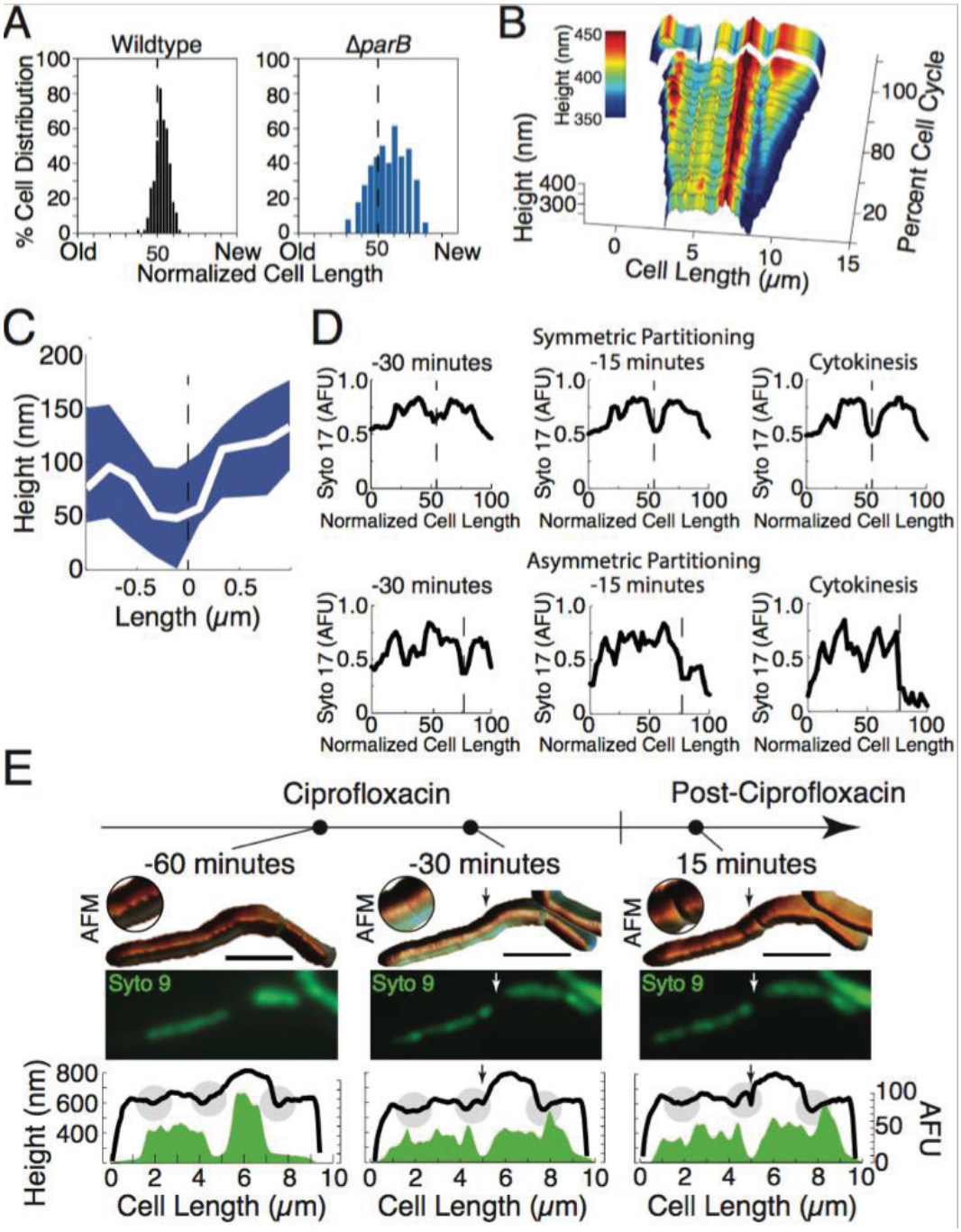

Figure 5.4 Asymmetric divisions occur at off-center wave-troughs. (A) Distribution of division site selection in wild-type cells (black histogram) and Δ*parB* cells (blue histogram). (B) Kymograph of cell height of a representative Δ*parB* cell from birth to division, showing asymmetric division within an off-center wave-trough. (C) Averaged surface height around future sites of off-center divisions (n = 27). White line depicts the average height within a range ± 1 µm in each direction of the separation site. Blue background depicts the variation (25th and 75th percentiles) in surface height. (D) Representative graphs depicting the distribution of DNA along the cell length of Δ*parB* cells at 30, 15, and 0 minutes prior to cytokinesis. Top: an example of symmetric nucleoid partitioning. Bottom: an example of asymmetric nucleoid partitioning leading to the formation of an anucleate new-pole daughter cell. Dashed lines correspond to future division

sites, which often correspond to local minima of chromosomal DNA. (E) AFM (upper) and fluorescence (middle) images of a representative wild-type cell before (-60 and -30 minutes) and after (+15 minutes) release from a ciprofloxacin block. Longitudinal height profiles (black lines) stacked atop DNA profiles (green plots) of the same cell show that the future division site (arrows) occurs at a local DNA minimum within a wave-trough (grey circle).

5.3 Methods

Bacteria. *Mycobacterium smegmatis* mc^{2}155 (wild-type) and derivative strains were grown in Middlebrook 7H9 liquid medium (Difco) supplemented with 0.5% albumin, 0.2% glucose, 0.085% NaCl, 0.5% glycerol, and 0.05% Tween-80. Cultures were grown at 37°C to mid-exponential phase (OD_{600} ~ 0.5). Aliquots were stored in 15% glycerol at -80°C and thawed at room temperature before use; individual aliquots were used once and discarded. The Δ*parB* strain with an unmarked in-frame deletion of the *parB* gene was described previously (*76*). The *attB*-integrating plasmid expressing a Wag31-GFP fusion protein was described previously (*54*).

FtsZ-GFP Reporter. The open reading frame (ORF) encoding *M. smegmatis* FtsZ was PCR-amplified using primers MsmftsZ-F (gctagcatgaccccccgcataactacctcg) and MsftsZ-R (ggactagttcctcctgatcctcctccacctgaaccaccaccacctgaaccaccaccacctgaaccaccggtgtgccgcatgaagggcg) with genomic DNA as the template. The underlined sequence in primer MsmftsZ-R represents the linker sequence encoding four repeats of Gly-Gly-Ser-Gly-Gly. The amplicon was ligated into vector pCR2.1 (Invitrogen) and verified by DNA sequencing, then excised as an *Nhe*I-*Spe*I fragment and ligated into the unique *Nhe*I site in the *attB*-integrating vector pND250 (gift from N. Dhar), which encodes a hygromycin resistance marker. The resulting plasmid (pND275) expresses *ftsZ-gfp* (in-frame fusion) from a strong anhydrotetracycline (ATc)-inducible promoter. pND275 was electroporated into *M. smegmatis* and transformants were selected by plating on solid medium containing hygromycin.

Microscopy. For time-lapse fluorescence microscopy, bacteria were grown to mid-exponential phase (OD_{600} ~0.5) in 7H9 liquid medium, collected by centrifugation (2400 *g*, 5 minutes), concentrated 30-fold in fresh 7H9 medium (37°C), and passed through a 5 µm pore-size polyvinylidene difluoride syringe filter (Millipore) to remove clumps. The declumped bacteria were spread on a glass coverslip, covered with a semipermeable membrane, and cultured in a custom-made microfluidic device with a continuous flow of 7H9 medium at 37°C (flow rate, 25 µl min^{-1}), as described (*89*). Nucleoid staining of the strain, WT mc^{2}155 expressing Wag31-GFP, was accomplished by adding SYTO 17 (red, 5 µM) to the flow medium. Bacteria were imaged at 15-minute intervals with a DeltaVision personal DV microscope (Applied Precision) equipped with a 100X oil-immersion objective and an environmental chamber maintained at 37°C (*54*). Images were recorded on phase-contrast and fluorescence channels (475/28-nm excitation filter and 525/48-nm emission filter for FITC; 575/25-nm excitation filter and 632/22-nm emission filter for SYTO17) with a CoolSnap HQ2 camera.

Atomic Force Microscopy. Coverslips were prepared by mixing polydimethylsiloxane (PDMS) (Sylgard 184, Dow Corning) at a ratio of 15:1 (elastomer : curing agent). Air bubbles in the mixture were removed under negative pressure for 15 minutes. The PDMS mixture was

dropped onto a 22 mm glass coverslip (VWR) and spin-coated at 8,000 rpm (SUSS MicroTec Lab-Spin6) (*69*) for 30 seconds. PDMS-coated coverslips were baked at 80°C for 10 minutes before use. A 3-ml aliquot of mid-exponential phase cell culture was filtered through a 0.5 mm pore size PVDF filter (Millipore) to remove cell clumps and concentrated into 200 ml final volume by pelleting cells (2,400 *g*, 8 minutes). A 50-µl aliquot was deposited on the hydrophobic surface of a PDMS-coated coverslip and incubated for 20 minutes to increase the non-specific surface interactions between bacteria and coverslip. A constant flow (140 µl min^{-1}) of Middlebrook 7H9 medium was supplied by a syringe pump. Where indicated, isoniazid (Sigma) was added to the flow medium at 5 µg ml^{-1} (1X MIC) or 50 µg ml^{-1} (10X MIC). The flow medium was preheated in a custom-made chimney that served as a bubble trap and heating element for maintaining fluid at 37°C in the sample space. Bacteria were imaged by Peak Force QNM with a Nanoscope 5 controller (Veeco Metrology) at a scan rate of 0.5 Hz and a maximum Z-range of 5 µm. A ScanAsyst fluid cantilever (Bruker) was employed. Continuous scanning provides snapshots at 10-minute intervals. Height, peak force error, adhesion, dissipation, deformation, DMT modulus, and log DMT modulus were recorded for all scanned images. Images were processed using a custom-made Matlab program (*90*) or Gwyddion (Dept. Nanometrology, Czech Metrology Institute). ImageJ was used for extracting bacterial cell profiles in tabular form. Matlab scripts were developed for automating the analysis of experimental data sets and generating graphical representations of data.

Correlated Fluorescence and Atomic Force Microscopy. Correlated fluorescence and AFM images were acquired as described (*60*). Briefly, fluorescence images were acquired with an EMCCD iXon Ultra 897 camera (Andor) mounted on an IX71 inverted optical microscope (Olympus) equipped with an UAPON100XOTIRF 100X oil immersion objective (Olympus) with the 2X magnifier in place. Illumination was provided by an MLC monolithic laser combiner (Agilent) using the 488 nm or 561 nm laser output coupled to an optical fiber with appropriate filter sets: F36-526 for GFP and F72-866 for FM4-64 (AHF Analysetechnik, Germany). For membrane staining 0.2 µg ml^{-1} FM4-64 (Life Technologies) was used. The AFM was mounted on top of the inverted microscope and images were acquired with a Dimension Icon scan head (Bruker) using ScanAsyst fluid cantilevers (Bruker) with a nominal spring constant of 0.7 N m^{-1} in peak force tapping mode at a setpoint < 2 nN and typical scan rates of 0.5 Hz. The samples were maintained at 37°C in 7H9 liquid medium heated by a custom-made coverslip heating holder controlled by a TC2-80-150 temperature controller (Bioscience Tools).

Cell Measurements. Cell length was measured as the sum of short linear segments tracking along the centerline of individual cells. Cell lengths at birth (L_b) and division (L_d) were defined as distances between cell ends. Interdivision time (I_t) was defined as the time between birth and division. Elongation velocity averaged over the lifetime of the cell was defined as $(L_d - L_b)/I_t$. Elongation rate averaged over the lifetime of the cell was defined as $(L_d/L_b)/I_t$. Elongation rate averaged over a specific time interval was defined as $(L_n/L_i)/(t_n - t_i)$, where L_i is the initial cell length at time t_i, and L_n is the cell length at a later time t_n. Cell volume was calculated as the sum of the cylindrical volume of each incremental pixel along the midline of the cell using the height as the diameter. Volume at birth (V_b) and division (V_d) were defined for each cell. Velocity of volume change averaged over the lifetime of the cell was defined as $(V_d - V_b)/I_t$. Rate of volume change averaged over the lifetime of the cell was defined as $(V_d/V_b)/ I_t$. Rate of volume change

averaged over a specific time interval was defined as $(V_n/V_i)/(t_n - t_i)$, where V_i is the initial cell length at time t_i and V_n is the cell length at a later time t_n. Cell profiles were traced along the highest point in the lateral axis, following the length of the cell (ridgeline).

5.4 Supporting Information

Supporting Figure 5.1 Time series of AFM height images. Time series of AFM height images for wild-type M. smegmatis cells corresponding to Figure 5.1A. Scale bar, 5 µm.

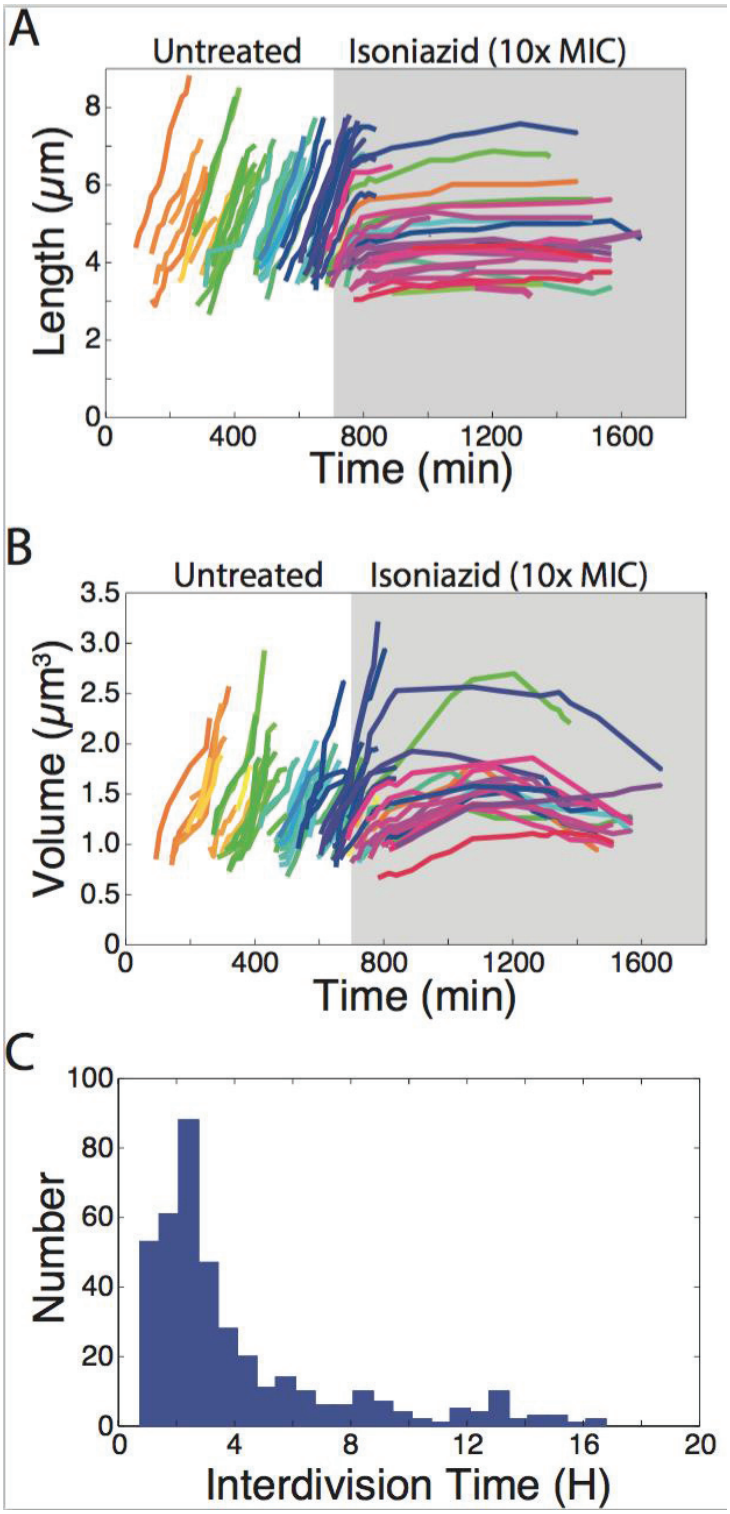

Supporting Figure 5.2 Single-cell growth dynamics. Cells were imaged by AFM at 12-minute intervals before and after addition of isoniazid (n = 270). Lines indicate individual cells plotted from birth to division and colors indicate the generation for all cell lineages (A & B). (A) Cell length. (B) Cell volume. (C) Distribution of single-cell interdivision times for untreated cells.

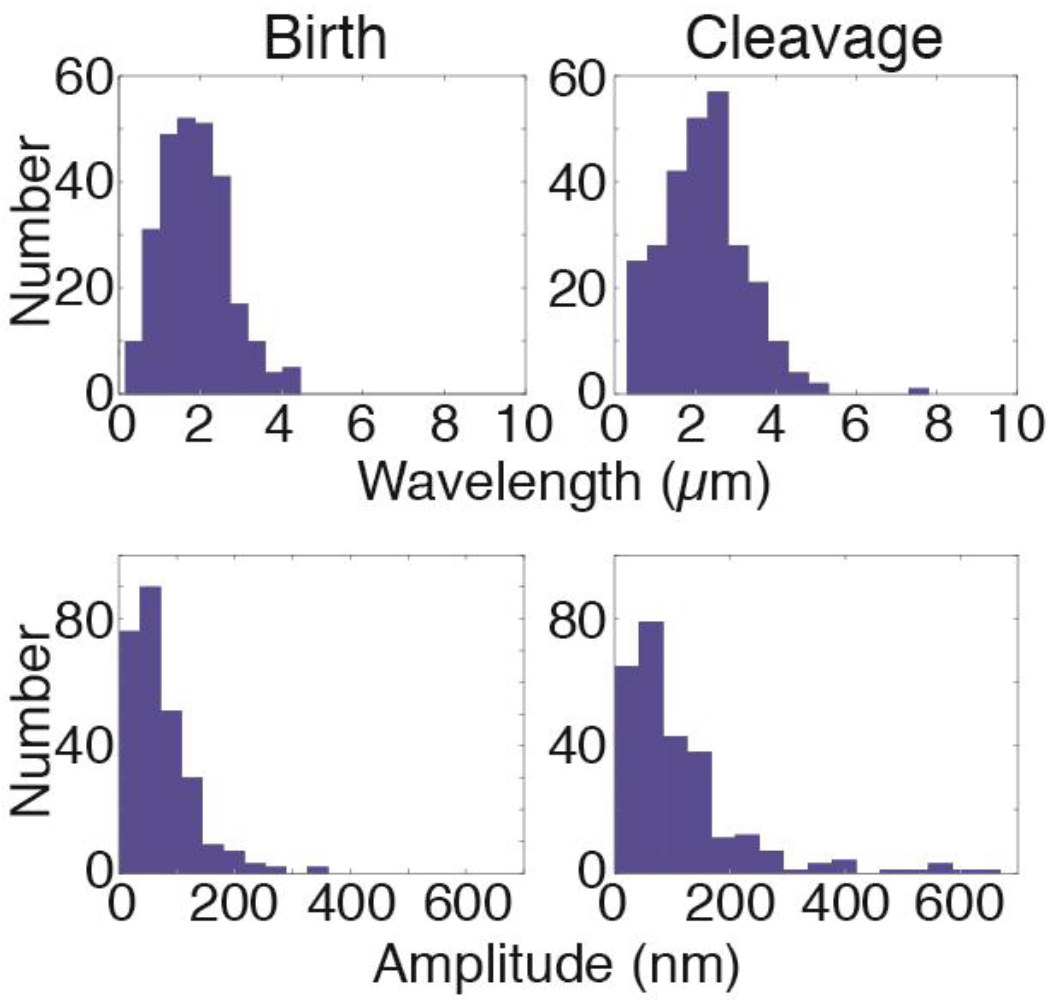

Supporting Figure 5.3 Cell-surface waveform dimensions. Distribution of single-cell wavelengths (upper row) and amplitudes (lower row) between adjacent wave-troughs at birth (column 1) and separation (column 2) (n = 270 cells).

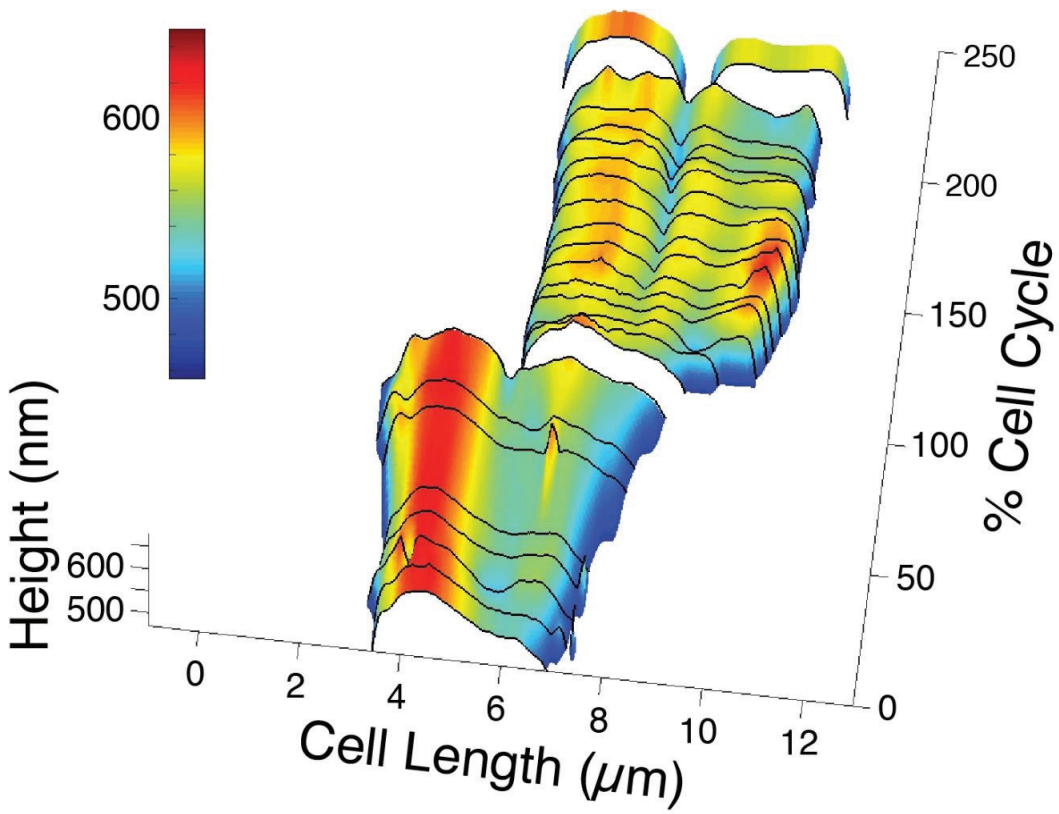

Supporting Figure 5.4 Division site selection in wild-type bacteria blocked in cell elongation. Kymograph representation of the cell surface height of single cells treated with INH (10X MIC) over three consecutive generations. Generational time progresses from bottom to top.

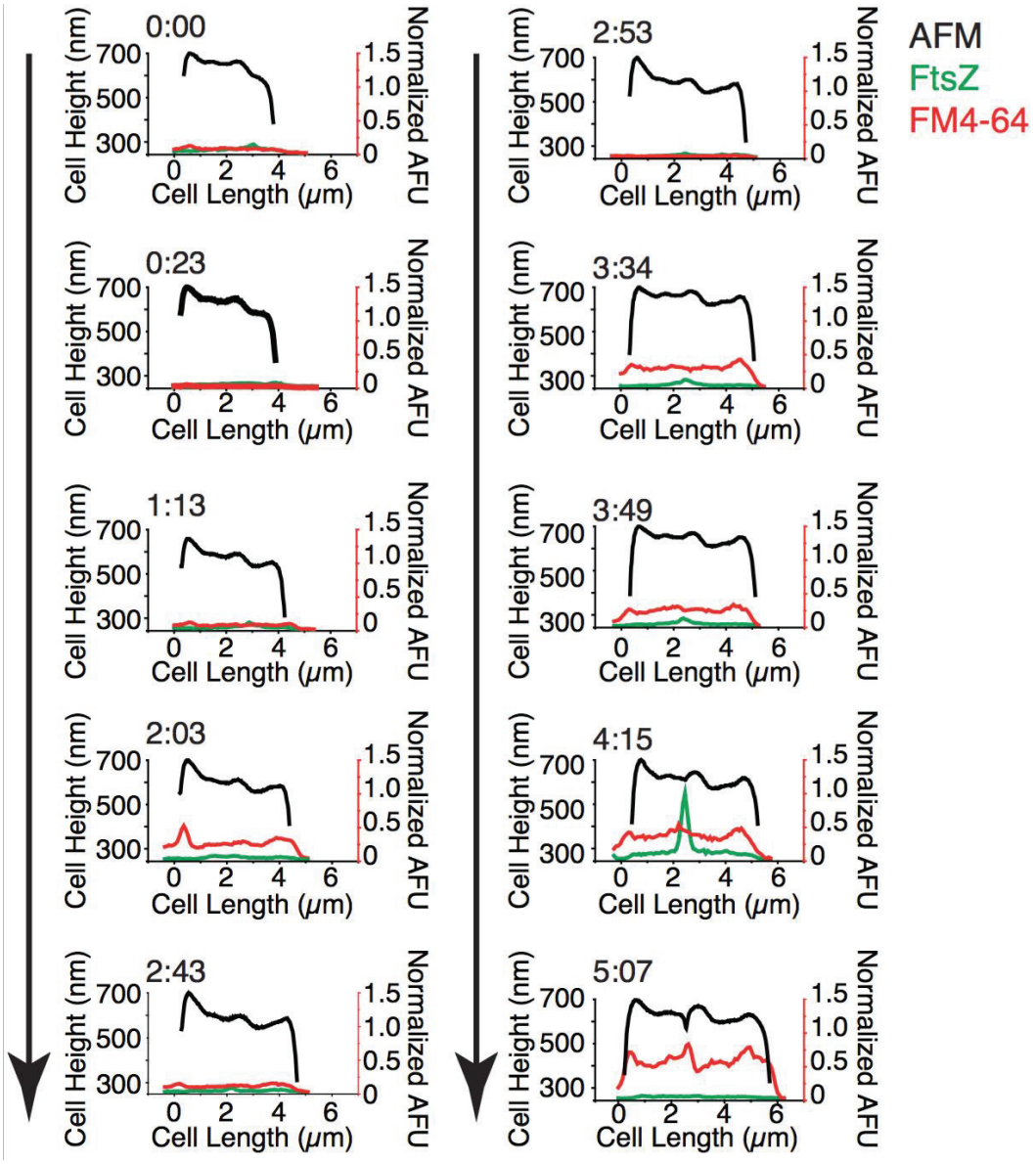

Supporting Figure 5.5 Sequence of events culminating in cell division. Cells expressing FtsZ-GFP (green) were stained with the membrane dye FM4-64 (red) to determine the timing between appearance of the Z-ring at the future division site and onset of septum formation. Cells were imaged at 15-minute intervals by correlated fluorescence and atomic force microscopy. Plots show longitudinal height profiles (black lines) and fluorescence intensity profiles (green and red lines) of a representative cell. Numbers in the upper left corner of each graph indicate the time point (t) between birth (at t = 0 min) and separation (at t = 307 min). AFU, arbitrary fluorescence units.

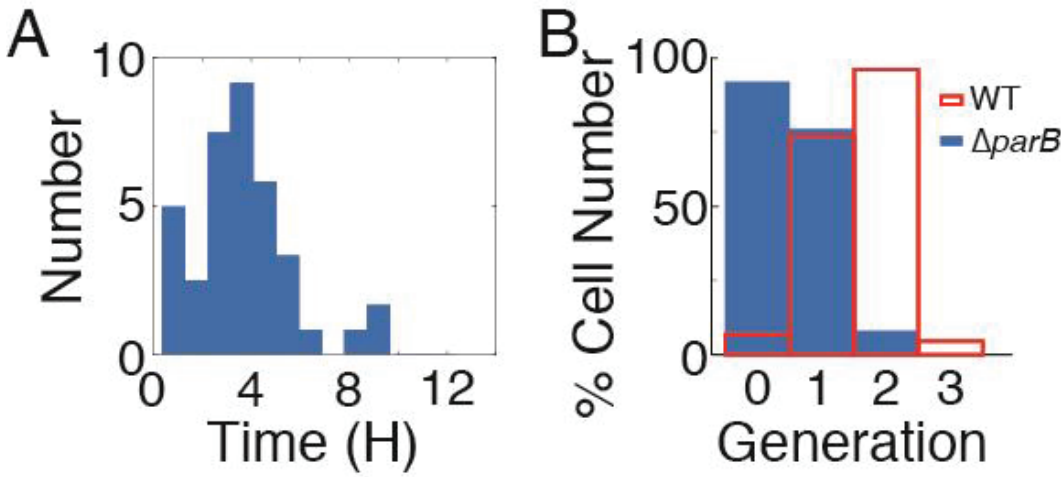

Supporting Figure 5.6 Wave-trough age in ΔparB cells. Distributions of (A) time intervals or (B) generation times from wave-trough formation to cell separation in ΔparB cells.

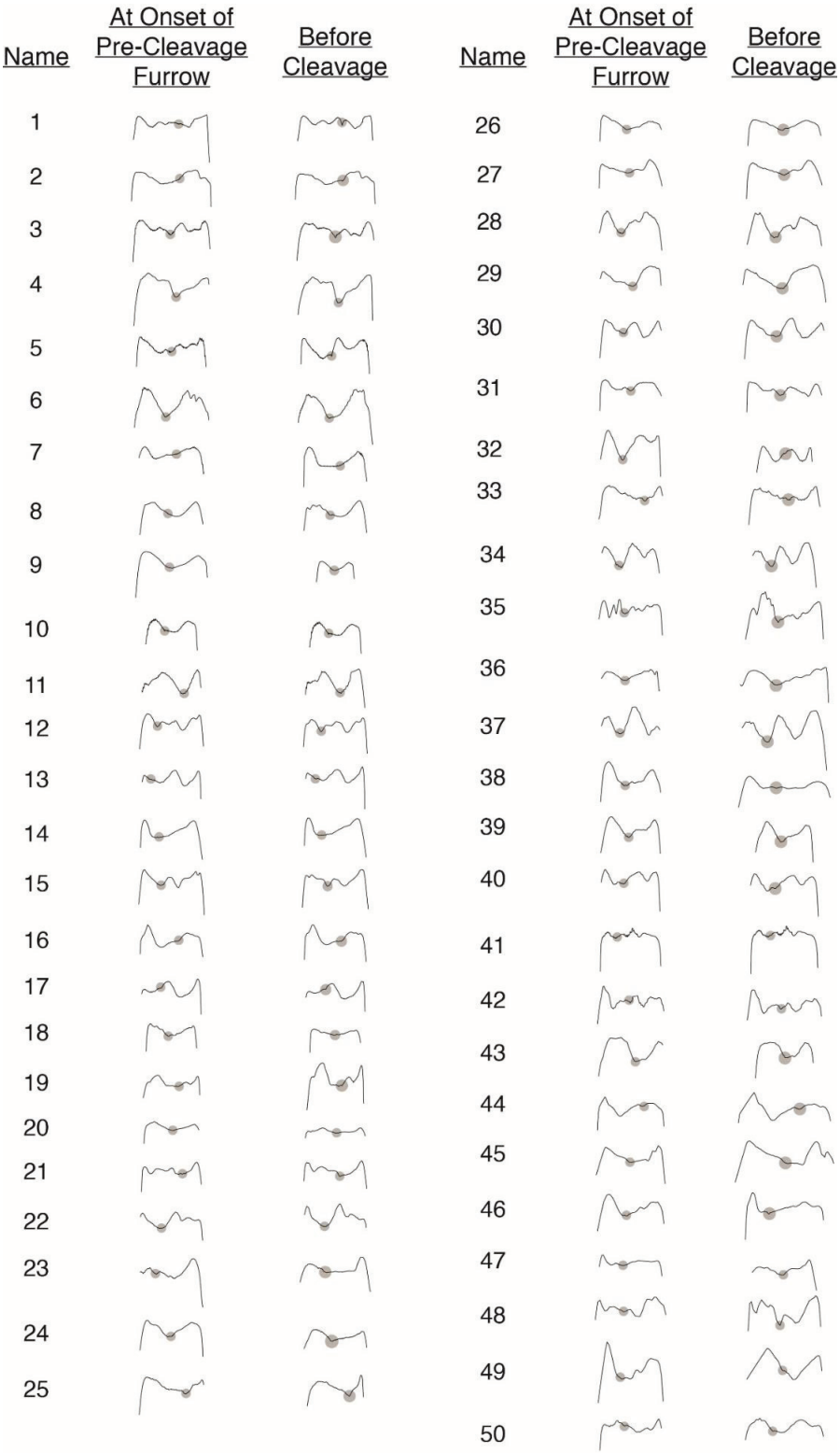

Supporting Figure 5.7 Profile traces of ΔparB cells. Longitudinal height profiles of ΔparB cells approximately 15 minutes prior to separation (A) or at first appearance of the pre-separation furrow (B). Grey circles highlight separation sites along the height profile of individual cells.

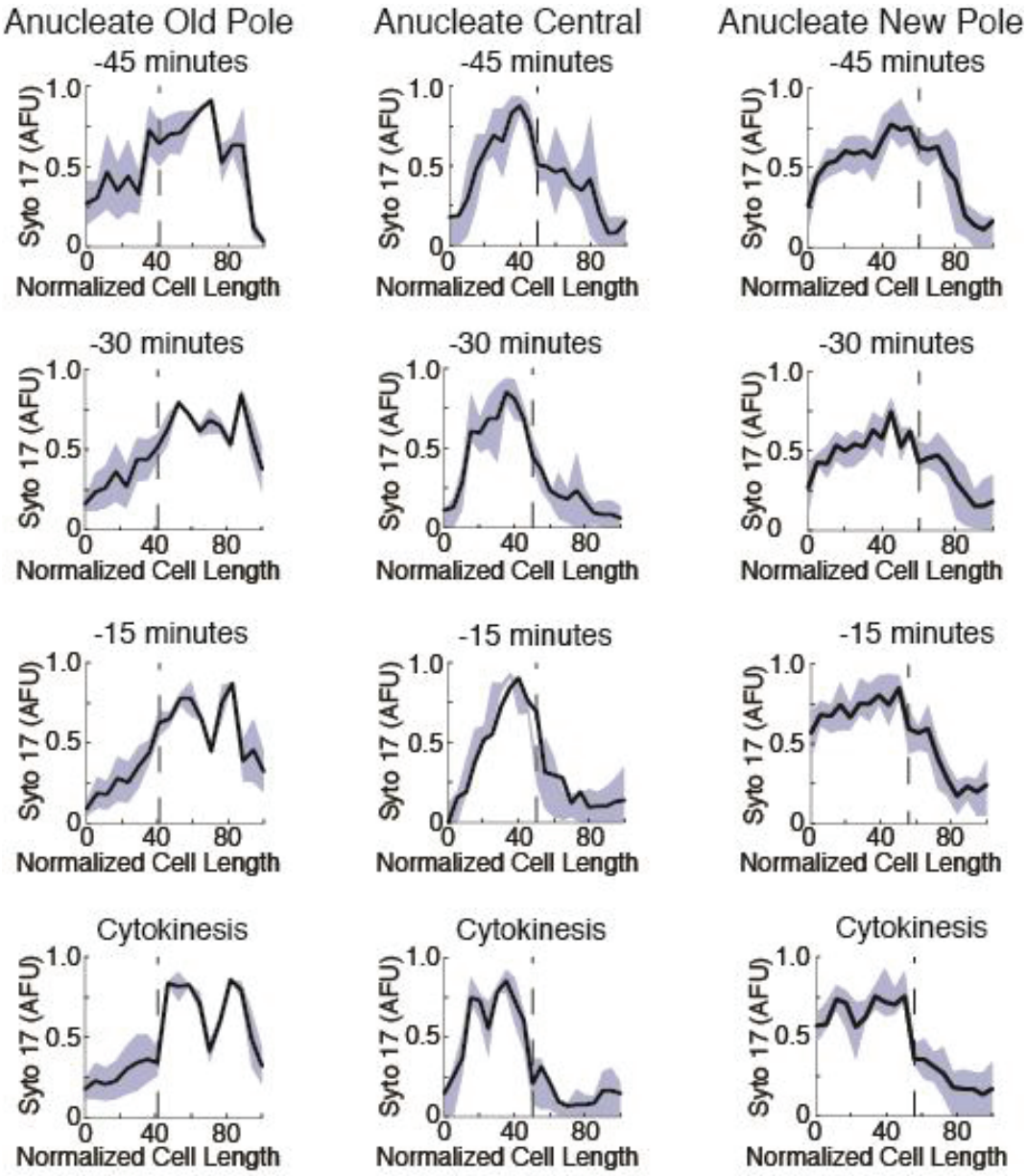

Supporting Figure 5.8 DNA distribution in ΔparB cells producing one anucleate daughter. Graphical representations of the average DNA distribution in dividing cells producing one anucleate daughter and one nucleate daughter, showing the position at which cells divide along the cell length. (Column 1) Asymmetrically dividing cells (n = 3) producing one nucleate new-pole daughter and one anucleate old-pole daughter. (Column 2) Centrally dividing cells (n = 5) producing one nucleate old-pole daughter and one anucleate new-pole daughter. (Column 3) Asymmetrically dividing cells (n = 7) producing one nucleate old-pole daughter and one anucleate new-pole daughter. Graphs represent the DNA distribution at the time of cytokinesis (cytoplasmic compartmentalization), as well as 15, 30, and 45 minutes prior. The dashed vertical line denotes the mean site of cell division. Black lines represent the average level of DNA occupancy. Colored background represents the 25-75 percentiles in the variability of DNA occupancy. Chromosomal DNA was stained with SYTO 17.

Chapter 6 Chronic inflammation imposes aberrant cell fate in regenerating epithelia through mechanotransduction

This is a verbatim copy of an article that has been published in a peer reviewed journal: Craig S. Nowell, Pascal D. Odermatt, Luca Azzolin, Sylke Hohnel, Erwin F. Wagner, Georg E. Fantner, Matthias P. Lutolf, Yann Barrandon, Stefano Piccolo and Freddy Radtke. Chronic inflammation imposes aberrant cell fate in regenerating epithelia through mechanotransduction. Nature Cell Biology, *2015.*

*My contribution to this project was the mechanical characterization of the tissue sections by AFM and the correlation with fluorescent microscopy, the analysis of the data as well as making that part of the figure (*Figure 6.7*).*

6.1 Abstract

Chronic inflammation is associated with a variety of pathological conditions in epithelial tissues, including cancer, metaplasia and aberrant wound healing. In relation to this, a significant body of evidence suggests that aberration of epithelial stem and progenitor cell function is a contributing factor in inflammation-related disease, although the underlying cellular and molecular mechanisms remain to be fully elucidated. In this study, we have delineated the effect of chronic inflammation on epithelial stem/progenitor cells using the corneal epithelium as a model tissue. Using a combination of mouse genetics, pharmacological approaches and *in vitro* assays, we demonstrate that chronic inflammation elicits aberrant mechanotransduction in the regenerating corneal epithelium. As a consequence, a YAP–TAZ/β-catenin cascade is triggered, resulting in the induction of epidermal differentiation on the ocular surface. Collectively, the results of this study demonstrate that chronic inflammation and mechanotransduction are linked and act to elicit pathological responses in regenerating epithelia.

6.2 Introduction

Chronic inflammation is associated with a variety of pathologies in self-renewing epithelial tissues, including impaired wound healing, metaplasia and cancer (*91-93*). Indeed, several studies have demonstrated that chronic inflammation is in fact a key driver of aberrant function in epithelial cells (*94-97*), although the underlying mechanisms are only beginning to be elucidated. Of particular interest is how stem/progenitor cells in self-renewing epithelia are affected by exposure to a chronic inflammatory environment, especially as aberrant stem cell function is associated with diseases linked to chronic inflammation (*97-100*).

Previous studies have shown that chronic inflammation can exert a direct effect on epithelial stem/progenitor cells by secreting soluble factors that regulate key signalling cascades controlling stem cell function (*101-103*). However, in addition to regulation by soluble factors such as cytokines and growth factors, stem cells are also regulated by a variety of other microenvironmental cues. In particular, the mechanical properties of tissues can profoundly influence cellular responses and can exert a dominant influence on their response to the milieu of extrinsic factors present in the tissue stroma/niche (*104, 105*).

Mechanical cues, such as elasticity and topography, are heavily influenced by the deposition and organization of extracellular matrix (ECM) proteins (*106-109*), which are secreted by stromal cell types such as tissue-resident fibroblasts (*106, 109*). Interestingly, a hallmark of many chronic inflammatory conditions is fibrosis, in which excessive ECM deposition occurs in response to persistent inflammation (*110-112*). This therefore raises the possibility that at least some of the effects of chronic inflammation may be a consequence of altered mechanical cues downstream of fibrosis. Thus, understanding the link between chronic inflammation and tissue mechanical properties may identify new therapeutic targets.

The corneal epithelium (CE), which forms a protective barrier on the anterior ocular surface, is a clinically relevant example of a self-renewing epithelium in which chronic inflammation is closely associated with abnormal function.

The CE is a stratified epithelium that resides on a relatively simple, avascular stroma and which is maintained during homeostasis and repair by corneal epithelial stem cells (*113*) (CESCs). At present, the precise identity of CESCs is unknown as stem-cell-specific markers are lacking. However, label-retaining experiments and functional assays indicate that they reside predominantly, although not exclusively, at the limbus, a junctional zone between the cornea and the conjunctiva (*114, 115*). Importantly, stem cells isolated from the limbus can be used clinically to reconstitute the corneal epithelium following injury or disease, either by direct transplantation or by grafting *in vitro*-expanded cultures of limbal stem cells (*116*).

Chronic inflammation has a profound effect on the function of CESCs, and is associated with poor outcome in limbal transplantation (*117*) and with conditions such as corneal squamous cell metaplasia (CSCM), in which the CE adopts a keratinizing, skin-like fate (*118-120*).

We have previously shown that loss of Notch1 in the mouse CE promotes the development of CSCM specifically during repair (*121*). In this model CSCM is induced following remodelling of the underlying corneal stroma by the Notch1-deficient CE and is thus a consequence of changes in the surrounding microenvironment. Interestingly, in other stratified epithelial tissues, such as the skin, Notch signaling has been shown to negatively regulate inflammation (*122, 123*), raising the possibility that an aberrant inflammatory response during wound healing may play a role in promoting CSCM in Notch1 mutants. In this study, we have used Notch1 mutant mice as a means to investigate the significance of inflammation during CSCM induction and have specifically explored the link between inflammation and mechanotransduction in mediating cell fate alterations.

6.3 Results

6.3.1 Chronic inflammation promotes CSCM

To investigate the role of inflammation in CSCM, we used *Notch1*$^{lox/lox}$ *:K5Cre*^{ERT} mice, in which tamoxifen-induced cre activity results in conditional deletion of Notch1 in the CE (*121*). Consistent with our previous report, the unwounded *Notch1*-deficient (*Notch1*$^{\Delta}$) cornea maintained corneal identity on the ocular surface, as indicated by the expression of the corneal-specific cytokeratin 12 (K12), and exhibited a simple, relatively acellular stroma, and was thus indistinguishable from wild-type (WT) controls (Supporting Figure 6.1a). However, after repeated injury (Figure 6.1a), *Notch1*$^{\Delta}$ mice developed corneal opacity and significant morphological changes at the histological level (Figure 6.1b). Specifically, the *Notch1*$^{\Delta}$ corneal stroma was infiltrated with large numbers of polymorphonuclear neutrophils, indicative of an ongoing inflammatory response, and exhibited CSCM, indicated by expression of the epidermal-specific cytokeratin 1 (K1; Figure 6.1b). In contrast, WT controls did not exhibit any overt signs of inflammation and retained a K12^{+}K1^{-} corneal epithelium, although K12^{-}K1^{+} cells were present at the limbus (Figure 6.1b). Flow cytometric analysis confirmed that *Notch1*$^{\Delta}$ corneas contained increased numbers of CD45^{+} leukocytes both during repair and at least 21 days after injury when wound closure had occurred (Figure 6.1c,d), with most infiltrating CD45^{+} cells exhibiting a CD11b^{+}Gr1^{+} phenotype (Supporting Figure 6.1b,c), indicative of neutrophils. Furthermore, a variety of pro-inflammatory cytokines exhibited significant upregulation in the *Notch1*$^{\Delta}$ CE compared with WT CE following injury (Figure 6.1e). Collectively, the above findings indicate that CSCM in *Notch1*$^{\Delta}$ mice is closely associated with an augmented and chronic inflammatory response.

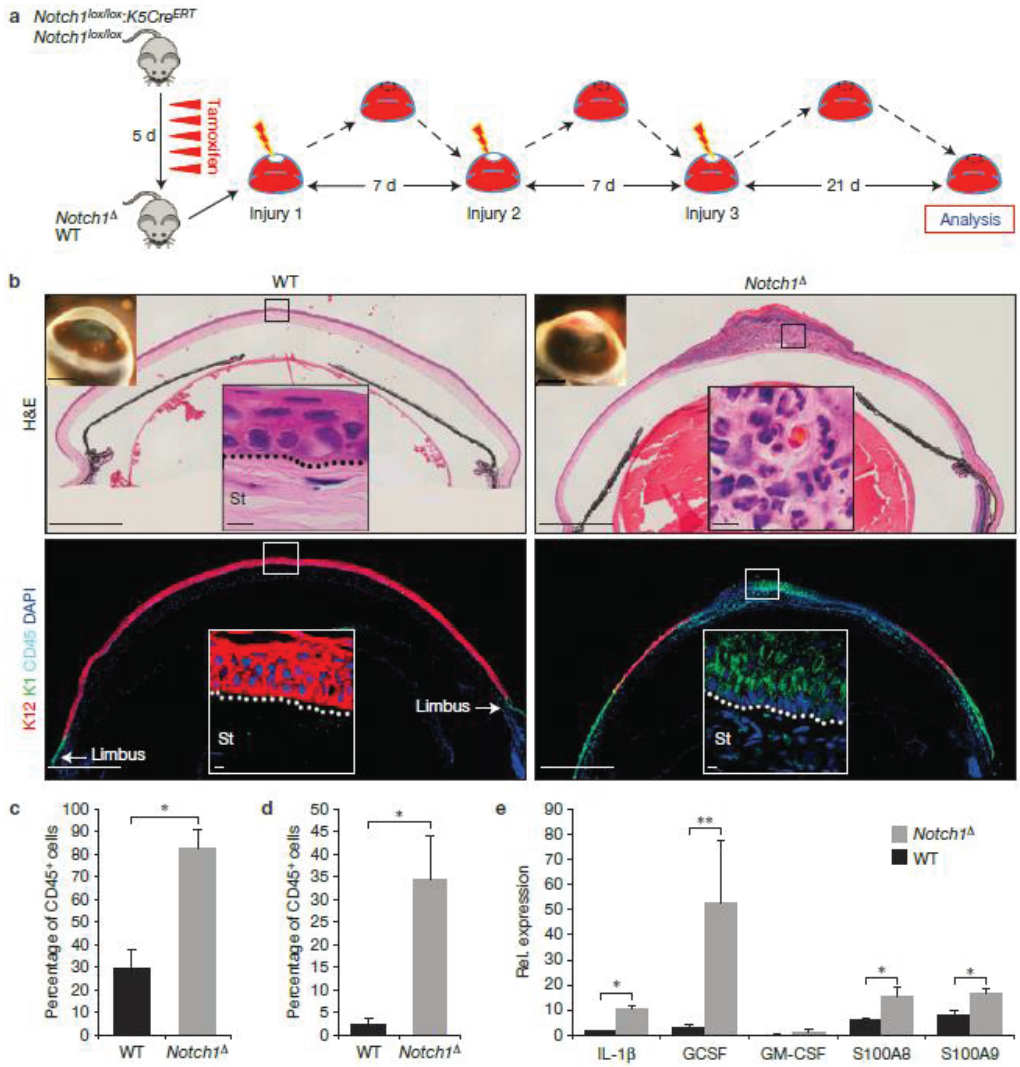

Figure 6.1 Corneal squamous cell metaplasia (CSCM) in *Notch1*$^{\Delta}$ mice is associated with an augmented and chronic inflammatory response. (a) Schematic depiction of the experimental strategy. (b) Histology of WT (*Notch1*$^{lox/lox}$) and *Notch1*$^{\Delta}$ corneal tissue after repeated injury (representative of 16 WT corneas and 20 *Notch1*$^{\Delta}$ corneas). Upper panels: haematoxylin and eosin (H&E) staining; lower panels: immunofluorescence for K12, K1 and CD45. Large panels are low-magnification tiled images. Insets on the upper left corner of the H&E images show gross phenotype on the ocular surface. Black (H&E) and white (immunofluorescence) outlined insets show high-magnification images of the indicated regions. (c,d) Quantification of the proportion of CD45^{+} cells in WT and *Notch1*$^{\Delta}$ corneas 24 h after a single injury (c) and 21 days after repeated corneal injury (d). Proportions were measured by performing flow cytometry on dissociated corneas (n=6 biological replicates for each genotype over three independent experiments; each replicate consists of cells pooled from 4 corneas isolated from 2 mice of each genotype). (e) QRT–PCR analysis for the indicated cytokines in WT (*Notch1*$^{lox/lox}$) and *Notch1*$^{\Delta}$ corneal epithelial cells 24 h after a single corneal injury. Data are expressed relative to the expression in WT unwounded corneal epithelial cells (n = 6 biological replicates for each genotype over three independent experiments; each replicate consists of corneal epithelial tissue pooled from 6 corneas isolated from 3 mice of each genotype). Scale bars represent 500 µm on tiled images and 5 µm on all other histological images. Scale bars on images showing gross morphology of corneas represent 1 mm. Black and white dotted lines indicate the boundary between the stroma and epithelium. St, stroma.*P <0.01, **P <0.05 (unpaired, two-tailed t-tests). Error bars represent standard deviation.

In light of this, we sought to establish whether chronic inflammation is both necessary and sufficient to induce epidermal differentiation on the ocular surface. We therefore employed two approaches. First, we aimed to abrogate the inflammatory response in *Notch1*$^{\Delta}$ mice to determine whether aberrant inflammation is essential for CSCM in this model. Second, we aimed to establish whether chronic inflammation is sufficient to induce CSCM in a Notch-independent setting.

Regarding the former, we noted that many of the pro-inflammatory cytokines upregulated in the *Notch1*$^{\Delta}$ CE are targets of the transcription factor AP-1. Furthermore, the *Notch1*$^{\Delta}$ CE exhibited increased phosphorylation of the AP-1 family member cjun at Ser 73, indicative of activation (Supporting Figure 6.2a). We therefore reasoned that persistent AP-1 activation in the *Notch1*$^{\Delta}$ CE contributes to the chronic inflammatory response in *Notch1*$^{\Delta}$ mice, consistent with previous reports (*124-126*). We therefore generated *Notch1*$^{lox/lox}$ *:cjun* $^{lox/lox}$ *:K5Cre*^{ERT} mice and simultaneously ablated *Notch1* and *cjun* by tamoxifen treatment (*Notch1*$^{\Delta}$*:cjun*$^{\Delta}$). Following injury, *Notch1*$^{\Delta}$*:cjun*$^{\Delta}$ mice exhibited a significantly reduced inflammatory response compared with *Notch1*$^{\Delta}$ mutants despite *Notch1* ablation (Supporting Figure 6.2b-e) and strikingly retained a K12^{+}K1^{-} CE after repeated injury (Supporting Figure 6.2f-h), supporting the hypothesis that chronic inflammation is essential for the development of CSCM in *Notch1*$^{\Delta}$ mice.

An important caveat to the experiments using the *Notch1*$^{\Delta}$*:cjun*$^{\Delta}$ mice is that AP-1 regulates a variety of cellular functions in addition to inflammation, including differentiation (*124, 127, 128*), and thus an autonomous effect cannot be ruled out. Therefore, to definitively establish that inflammation is the key driver of CSCM in *Notch1*$^{\Delta}$ mice, we administered a dexamethasone-based anti-inflammatory gel (Tobradex) to the ocular surface during the repeated injury procedure (Figure 6.2a). Strikingly, *Notch1*$^{\Delta}$ mice treated with Tobradex exhibited a relatively normal corneal stroma and maintained a K12^{+}K1^{-} CE (Figure 6.2b), despite *Notch1* ablation (Supporting Figure 6.2i), thus confirming that chronic inflammation is essential for CSCM in *Notch1*$^{\Delta}$ mutants.

To establish whether chronic inflammation is sufficient for the induction of CSCM in a Notch-independent setting, we performed the repeated injury procedure on *K14TSLPTg* mice(*129*), which develop chronic inflammation in stratified epithelia due to the expression of the pro-inflammatory cytokine TSLP ((*130*); Figure 6.2c). Strikingly, *K14TSLPTg* mice exhibited a near identical phenotype to *Notch1*$^{\Delta}$ mutants (Figure 6.2d), confirming that chronic inflammation is indeed sufficient for the induction of CSCM.

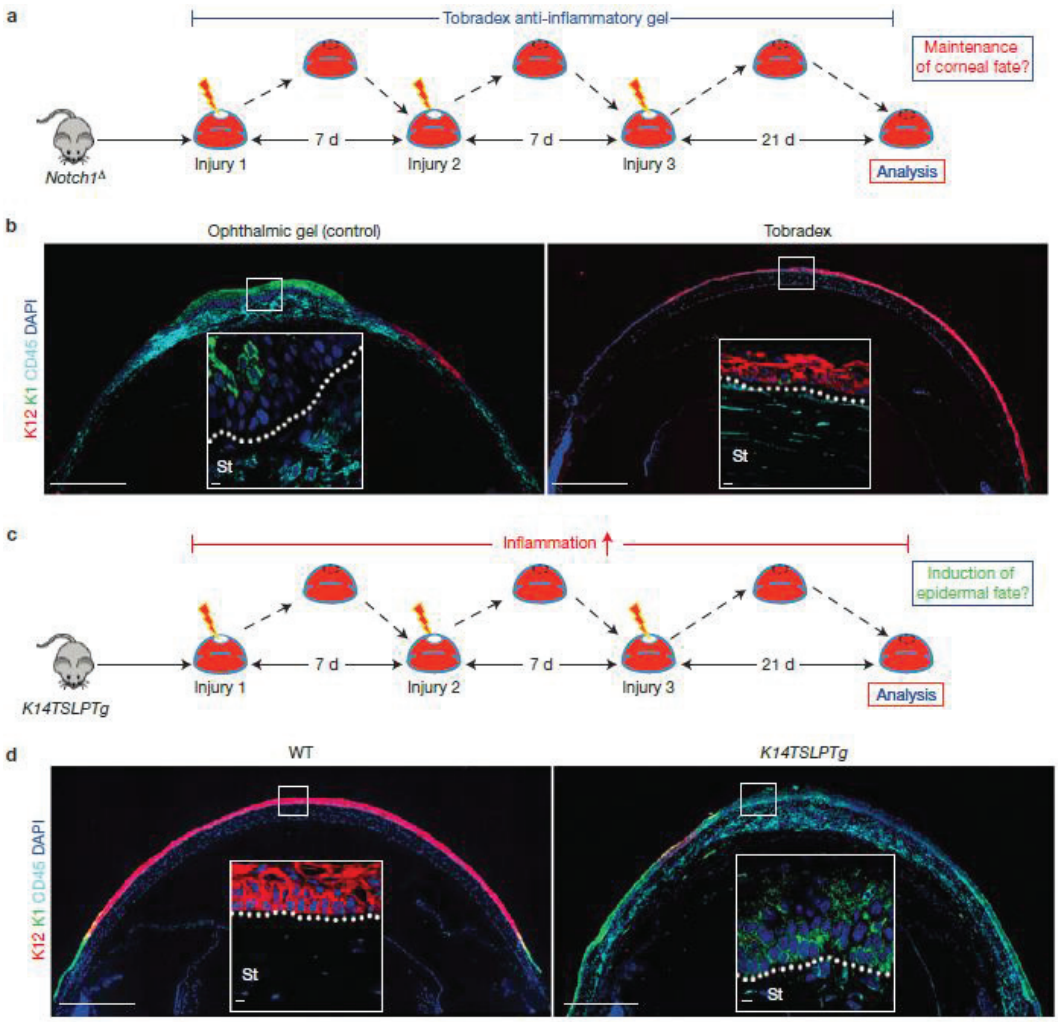

Figure 6.2 Chronic inflammation is necessary and sufficient to induce CSCM. (a) Schematic depiction of the experimental strategy used to determine whether chronic inflammation is necessary for the induction of CSCM in *Notch1*$^{\Delta}$ mice. (b) Immunofluorescent staining for K12, K1 and CD45 on *Notch1*$^{\Delta}$ corneas treated with ophthalmic gel (control) or the anti-inflammatory gel Tobradex. The images are representative of 6 corneas per treatment over three independent experiments. Large panels are low magnification tiled images. Insets show high-magnification images of the indicated regions. (c) Schematic depiction of the experimental strategy used to determine whether chronic inflammation is sufficient to induce CSCM. (d) Immunofluorescent staining for K12, K1 and CD45 on WT (non-transgenic littermates) and *K14TSLPTg* corneas after the procedure shown in c. The images are representative of 6 corneas per genotype over three independent experiments. Large panels are low-magnification tiled images. Insets show high-magnification images of the indicated regions. Scale bars represent 500 µm on tiled images and 5 µm on all other images. White dotted lines indicate the boundary between the stroma and epithelium. St, stroma.

6.3.2 CSCM is induced in activated stem/progenitor cells located at the limbus and peripheral cornea

We next sought to address the cellular and molecular mechanism by which chronic inflammation promotes aberrant cell fate and to this end used *Notch1*$^{\Delta}$ mice as a model of inflammation-associated CSCM.

Initially, we determined the spatial and temporal kinetics of CSCM development in *Notch1*$^{\Delta}$ mice. Whole-mount immunofluorescence on CE isolated after each injury-repair cycle demonstrated that CSCM first became apparent after the second injury (Supporting Figure 6.3a). This was characterized by the presence of K12^{-}K1^{+} cells within the *Notch1*$^{\Delta}$ CE, particularly at the peripheral cornea in close proximity to the limbus (Supporting Figure 6.3a). In contrast, WT CE remained K12^{+}K1^{-}, although K12^{-}K1^{+} epidermal cells were present in the limbus to varying degrees (Supporting Figure 6.3a).

We therefore chose to analyse the second injury-repair cycle at 0, 6 and 24 h after injury, to determine when and where CSCM is induced. In WT controls, K12^{+}K1^{-} cells predominated throughout the CE at each stage of repair, although K12^{-}K1^{+} cells were present in the limbus (Figure 6.3a,b), consistent with the observations from whole-mount analysis (Supporting Figure 6.3a). In contrast, Notch1$^{\Delta}$ mice exhibited increasingly prominent areas of K12^{-}K1^{+} cells extending from the limbus into the peripheral cornea as wound healing progressed (Figure 6.3a,b). In addition, the epithelium in the limbus and peripheral cornea of *Notch1*$^{\Delta}$ mice was generally less stratified than in WT controls (Figure 6.3a). Consistent with the whole-mount analysis, no overt phenotypic differences were apparent between WT and *Notch1*$^{\Delta}$ CE during the first injury-repair cycle (Supporting Figure 6.3b).

The above findings indicate that CSCM in *Notch1*$^{\Delta}$ mice is initially induced at the limbus/peripheral cornea and subsequently migrates to the site of injury as wound closure proceeds. This is consistent with the model of corneal regeneration proposed in a previous study, which found that cells mediating wound healing are derived from stem/progenitors located in the limbus25. In support of this, we observed increased proliferative activity in the limbus and peripheral cornea following injury (Supporting Figure 6.3c,d), suggesting activation of stem/progenitor cells specifically within these regions. In addition, whole-mount immunofluorescence on CE isolated after repeated injury revealed that metaplastic K12^{-}K1^{+} regions in *Notch1*$^{\Delta}$ CE remained continuous with the limbus/peripheral cornea, and thus conformed to the pattern expected if CSCM derived from this region (Figure 6.3c,d).

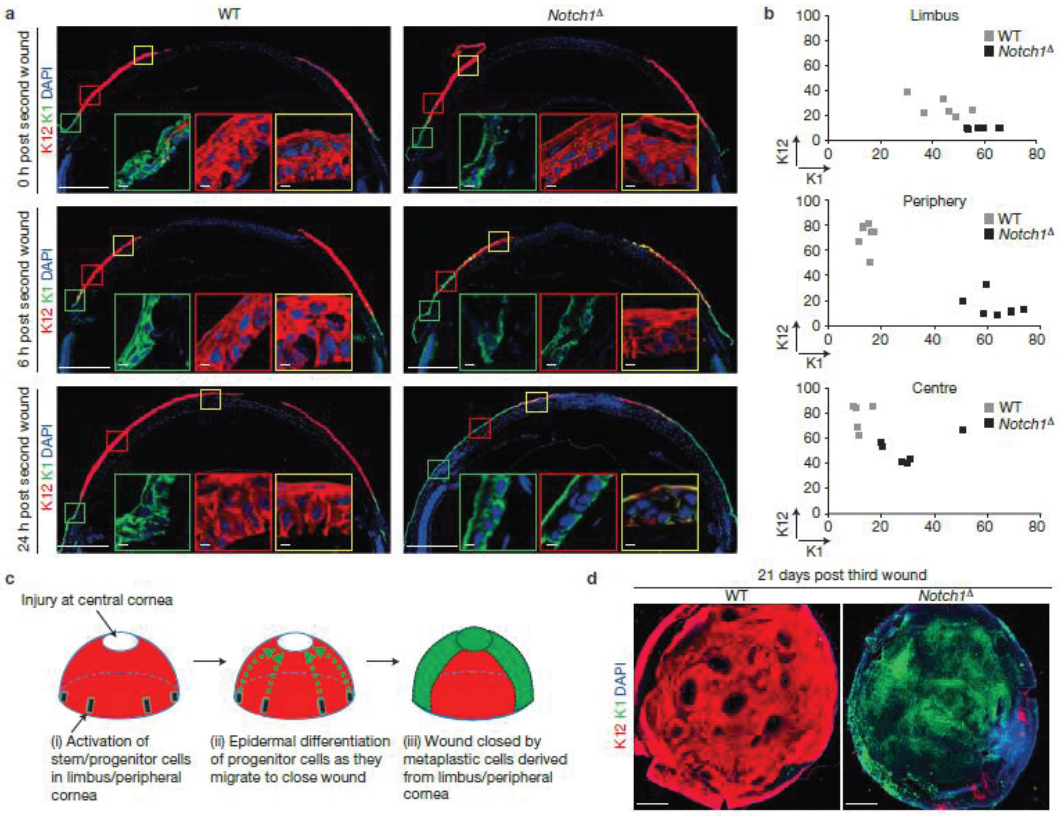

Figure 6.3 CSCM is induced in limbal and peripheral cells during repair. (a) Immunofluorescent staining for K12 and K1 in WT (*Notch1*$^{lox/lox}$) and *Notch1*$^{\Delta}$ corneas at 0, 6 and 24 h after a second corneal injury. The images are representative of 6 corneas per genotype over two independent experiments for each time point analysed. Large panels are low-magnification tiled images. Insets outlined in green, red and yellow show high-magnification images of the limbus, peripheral cornea and central cornea, respectively. (b) *XY* scatter plots showing K12 and K1 expression in the limbus, peripheral cornea and central cornea 24 h after a second corneal injury. Each data point represents mean fluorescence intensity measured from an individual cornea. Grey squares, WT (*Notch1*$^{lox/lox}$); black squares, *Notch1*$^{\Delta}$ (n=6 corneas for each genotype over three independent experiments). (c) Model predicting the cellular origin of CSCM. Following injury to the central cornea, stem/progenitor cells in the peripheral cornea become activated and proliferate to generate daughter cells that mediate wound closure. In *Notch1*$^{\Delta}$ mutants, chronic inflammation promotes epidermal differentiation of activated stem/progenitor cells or their immediate progeny. This model therefore predicts that all epidermal lineage cells in *Notch1*$^{\Delta}$ corneas will be derived from peripheral stem/progenitor cells and therefore be continuous with the peripheral cornea. (d) Immunofluorescent staining for K12 and K1 on whole-mount corneal epithelial tissue from WT (*Notch1*$^{lox/lox}$) and *Notch1*$^{\Delta}$ mice after repeated injury. The images are representative of 12 corneal whole-mounts per genotype over four independent experiments. Images shown are low magnification tiled images. Scale bars represent 500 µm on tiled images and 5 µm on all other images.

6.3.3 Chronic inflammation induces CSCM through elevation of β-catenin signalling in the CE

At the molecular level, aberrant Wnt/ β-catenin signalling has been linked to squamous cell metaplasia in a variety of epithelial tissues, including the cornea (*131-133*), and is therefore a good candidate for mediating CSCM in response to chronic inflammation. Consistent with this, the *Notch1*$^{\Delta}$ CE exhibited increased expression of β-catenin following induction of CSCM by repeated

injury (Figure 6.4a). To determine whether increased β-catenin expression overlapped with CSCM induction, we quantified its expression during each injury-repair cycle. In unwounded corneas and during the first injury-repair cycle, β-catenin expression was relatively high in the limbus but declined in the peripheral and central CE in WT and *Notch1*$^{\Delta}$ mice (Supporting Figure 6.4a,b). However, following the second injury, high β-catenin expression was evident throughout the *Notch1*$^{\Delta}$ CE (Figure 6.4b,c). In WT controls, β-catenin expression was increased in the limbus, but again declined in the peripheral and central CE (Figure 6.4b,c). Thus, high β-catenin expression overlapped spatially and temporally with the presence of K12^{-}K1^{+} epidermal cells.

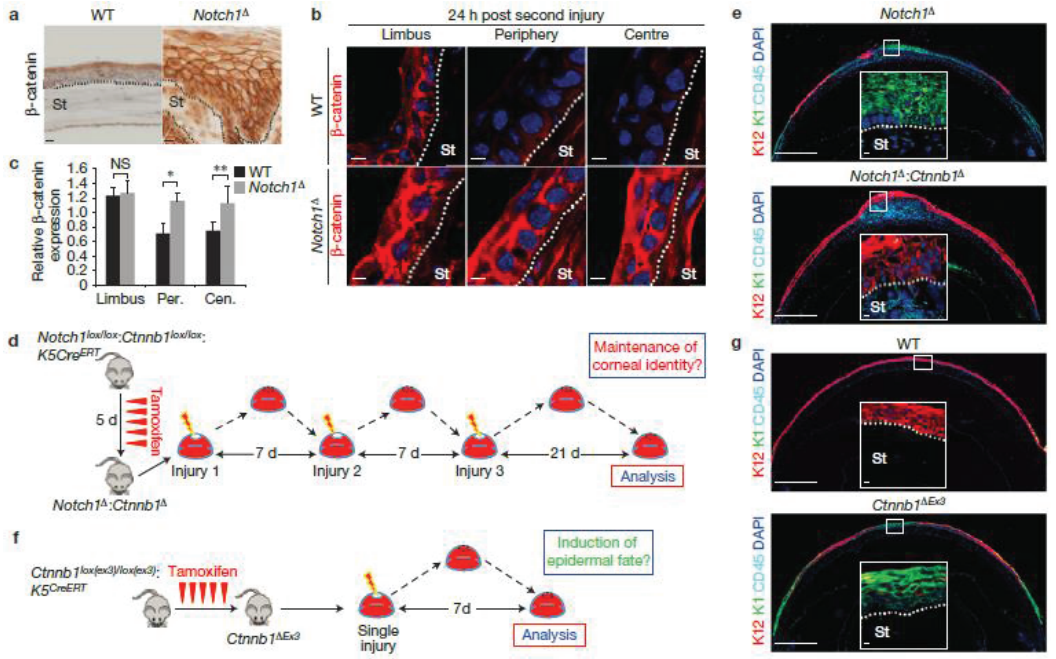

Figure 6.4 Chronic inflammation promotes CSCM through elevated β-catenin signalling. (a) Immunohistochemistry for β-catenin on WT (*Notch*$^{lox/lox}$) and *Notch1*$^{\Delta}$ corneas after repeated injury. Data are representative of 8 corneas per genotype over three independent experiments. (b) Immunofluorescent staining for β-catenin in limbus, peripheral cornea (Per.) and central cornea (Cen.) of WT (*Notch*$^{lox/lox}$) and *Notch1*$^{\Delta}$ corneas 24 h after the second corneal injury. The images are representative of 6 corneas isolated over three independent experiments. (c) Quantification of relative β-catenin expression in limbus, peripheral cornea and central cornea 24 h after the second corneal injury. Black bars, WT (*Notch*$^{lox/lox}$); grey bars, *Notch1*$^{\Delta}$ (n=6 corneas for each genotype over three independent experiments). Values for expression levels are relative values normalized to the expression level in the conjunctiva of each sample, determined by mean fluorescence intensity. (d) Schematic depiction of the experimental strategy used to determine whether β-catenin is necessary for the induction of CSCM. (e) Immunofluorescent staining for K12, K1 and CD45 on *Notch1*$^{\Delta}$and *Notch1*$^{\Delta}$:*Ctnnb1*$^{\Delta}$ corneas after the procedure outlined in d. The images are representative of 8 corneas per genotype over three independent experiments. Large panels are low-magnification tiled images. Insets are high-magnification images of the indicated regions. (f) Schematic depiction of the experimental strategy used to determine whether elevated β-catenin is sufficient to induce CSCM. (g) Immunofluorescent staining for K12, K1 and CD45 on WT (*Ctnnb1*$^{lox(ex3)/lox(ex3)}$) and *Ctnnb1*$^{\Delta Ex3}$ corneas 7 days after a single corneal injury. The images are representative of 8 WT corneas and 10 *Ctnnb1*$^{\Delta Ex3}$ corneas over four independent experiments. Large panels are low magnification tiled images. White outlined insets are high-magnification images of the indicated regions. Scale bars represent 500 µm on tiled images and 5 µm on all other images. White dotted lines indicate the boundary between the stroma and epithelium. St, stroma; NS, not significant. *P <0.01, **P <0.05 (unpaired, two-tailed t-tests). Error bars represent standard deviation.

To definitively establish whether β-catenin is the molecular factor that induces CSCM, we performed loss- and gain-of-function experiments *in vivo*. Thus, to determine whether β-catenin is necessary for CSCM induction, tamoxifen-treated *Notch1*$^{lox/lox}$*:Ctnnb1*$^{lox/lox}$*:K5Cre*^{ERT} mice, in which *Notch1* and *Ctnnb1* (β-catenin) are simultaneously ablated in the CE (*Notch1*$^{\Delta}$*:Ctnnb1*$^{\Delta}$), were subjected to repeated corneal injury (Figure 6.4d). This resulted in chronic inflammation in the corneal stroma in a similar manner to *Notch1*$^{\Delta}$ mutants (Figure 6.4e). However, β-catenin-deficient cells retained a predominantly K12^{+}K1^{-} phenotype, even in the presence of a chronic inflammatory environment, although the epithelium remained hyperplastic (Figure 6.4e, Supporting Figure 6.4c). Thus, elevated β-catenin signalling in corneal epithelial cells is essential for inflammation-induced CSCM.

In the reciprocal gain-of-function experiment, we induced constitutive activation of β-catenin in the CE using tamoxifen-treated *Ctnnb1* $^{lox(ex3)/lox(ex3)}$*:K5Cre*^{ERT} mice (*134*) (hereafter referred to as *Ctnnb1*$^{\Delta Ex3}$ mice), in which β-catenin is stabilized owing to cre-mediated excision of the degradation domain within exon 3. After a single injury-repair cycle (Figure 6.4f), *Ctnnb1*$^{\Delta Ex3}$ mice exhibited epidermal differentiation on the ocular surface, in contrast to WT controls that, as expected, maintained a corneal phenotype (Figure 6.4g). In this system, there was no evidence of chronic inflammation, as the presence of CD45^{+} cells in the *Ctnnb1*$^{\Delta Ex3}$ stroma seemed equivalent to WT controls (Figure 6.4g). Furthermore, the induction of epidermal differentiation correlated strictly with elevated β-catenin expression (Supporting Figure 6.4d). Together, these data strongly suggest that overexpression of β-catenin is sufficient for the cell-autonomous induction of CSCM. In addition, whole-mount immunofluorescence demonstrated that regions of CSCM in *Ctnnb1*$^{\Delta Ex3}$ cornea remained continuous with the limbus/peripheral cornea (Supporting Figure 6.4e), thus supporting the hypothesis that CSCM is induced at this location.

6.3.4 Chronic inflammation is associated with excessive ECM deposition, increased tissue stiffness and elevated mechanotransduction in the CE

We next addressed the mechanism by which chronic inflammation elicits elevated β-catenin in the CE. Surprisingly, we could not find any evidence of increased Wnt ligand expression in the *Notch1*$^{\Delta}$ cornea (Supporting Figure 6.5a), suggesting that the chronic inflammatory environment does not activate the Wnt signaling cascade. Previous studies have linked mechanotransduction to the induction of β-catenin activity in epithelia15. The mechanisms underlying mechanotransduction remain to be fully elucidated, although YAP/TAZ have recently emerged as primary cellular sensors of tissue mechanical cues (*104, 135*). Intriguingly, a recent report has shown that YAP/TAZ directly regulate β-catenin expression by forming an integral part of the cytoplasmic β-catenin destruction complex. According to the proposed model, removal of YAP/TAZ from the destruction complex, through mechanically induced nuclear translocation, increases β-catenin expression owing to impaired degradation (*136*). We therefore speculated that chronic inflammation may induce aberrant mechanotransduction in the CE by causing changes in the mechanical properties of the corneal stroma, for example through excessive deposition of ECM, as occurs in fibrosis (*137*). This would therefore result in nuclear localization of YAP/TAZ and increased β-catenin expression.

To determine whether increased ECM deposition was associated with CSCM, the expression of the ECM proteins periostin and tenascin C, which are linked to fibrosis (*138, 139*), was analysed during each injury-repair cycle. In WT corneas, both periostin and tenascin C were restricted to the stroma underlying the limbus at each stage (Figure 6.5a-d). A similar pattern was observed in unwounded *Notch1*$^{\Delta}$ corneas and in *Notch1*$^{\Delta}$ corneas during the first injury-repair cycle (Figure 6.5a-d). However, expression in the peripheral and central corneal stroma of *Notch1*$^{\Delta}$ mutants increased markedly during the second injury-repair cycle (Figure 6.5a-d). In support of a fibrotic-like response, the expression of periostin and tenascin C was largely restricted to non-haematopoietic cell types (Supporting Figure 6.5b). Furthermore, abrogation of inflammation in *Notch1*$^{\Delta}$ mice by Tobradex treatment resulted in reduced ECM deposition in the corneal stroma (Supporting Figure 6.5c), indicating that the effect occurred downstream of inflammation.

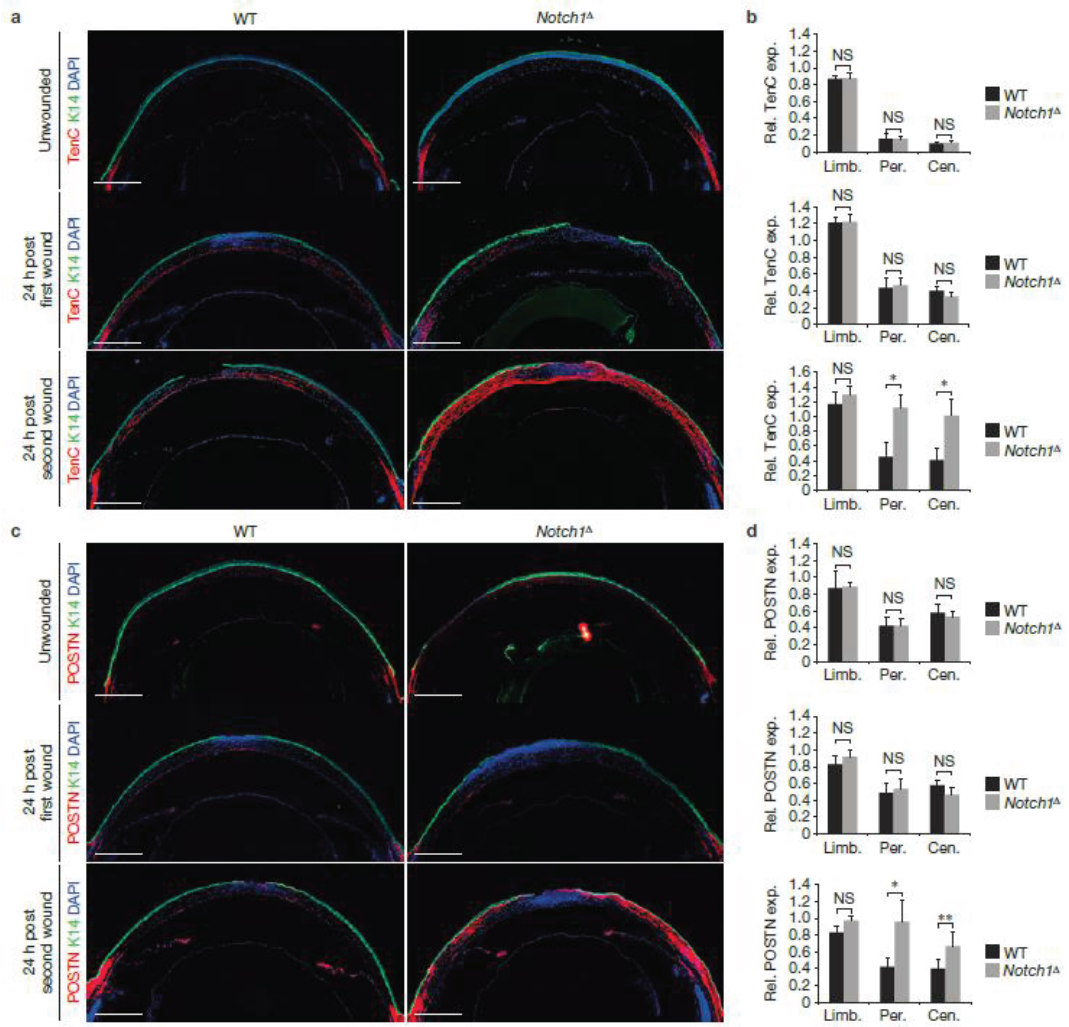

Figure 6.5 Increased ECM deposition in the corneal stroma in response to aberrant inflammation. (a) Immunofluorescent staining for K14 and tenascin C (TenC) in WT (*Notch*$^{lox/lox}$) and *Notch1*$^{\Delta}$ corneas, unwounded and 24 h after first and second wounds. The images are representative of 6 corneas per genotype for each time point analysed over three independent experiments. (b) Relative quantification of tenascin C expression in the limbus (Limb.), peripheral cornea (Per.) and central cornea (Cen.). Upper panel shows uninjured cornea; middle panel shows corneal tissue 24 h after the first injury; lower panel show corneal tissue 24 h after the second injury. Values for expression levels are relative values normalized to the expression level in the conjunctival stroma of each sample, determined by mean fluorescence intensity. Black bars, WT (*Notch*$^{lox/lox}$); grey bars, *Notch1*$^{\Delta}$ (n=6 corneas for each genotype at each time point over three independent experiments). (c) Immunofluorescent staining for K14 and periostin (POSTN) in WT (*Notch*$^{lox/lox}$) and *Notch1*$^{\Delta}$ corneas. The images are representative of 6 corneas per genotype for each time point analysed over three independent experiments. (d) Relative quantification of periostin expression in the limbus, peripheral cornea and central cornea in uninjured tissue (upper panel), corneal tissue 24 h after the first injury (middle panel) and corneal tissue 24 h after the second injury (lower panel). Values for expression levels are relative values normalized to the expression level in the conjunctival stroma of each sample, determined by mean fluorescence intensity. n=6 corneas for each genotype at each time point over three independent experiments. Scale bars on tiled images represent 500 µm. NS, not significant. $^{*}P$ <0.01, $^{**}P$ < 0.05 (unpaired, two-tailed *t*-tests). Error bars represent standard deviation.

ECM deposition in the corneal stroma also correlated with activation of mechanotransduction in the overlying CE after the second injury, as demonstrated by increased phosphorylation of focal adhesion kinase (pFAK), and increased nuclear localization of Rho coiled-coil kinase 2 (ROCK2) and YAP/TAZ (Figure 6.6a-g). Importantly, in unwounded corneas and in corneas isolated after the first injury, mechanotransduction was restricted to the ECM-rich limbus and was not apparent in the CE (Supporting Figure 6.6a,b). Furthermore, abrogation of inflammation in *Notch1*$^{\Delta}$ mice by Tobradex treatment reduced mechanotransduction in the corneal epithelium (Supporting Figure 6.6c). Thus, in a similar manner to β-catenin, there was a spatial and temporal overlap between increased ECM deposition, mechanotransduction and CSCM induction.

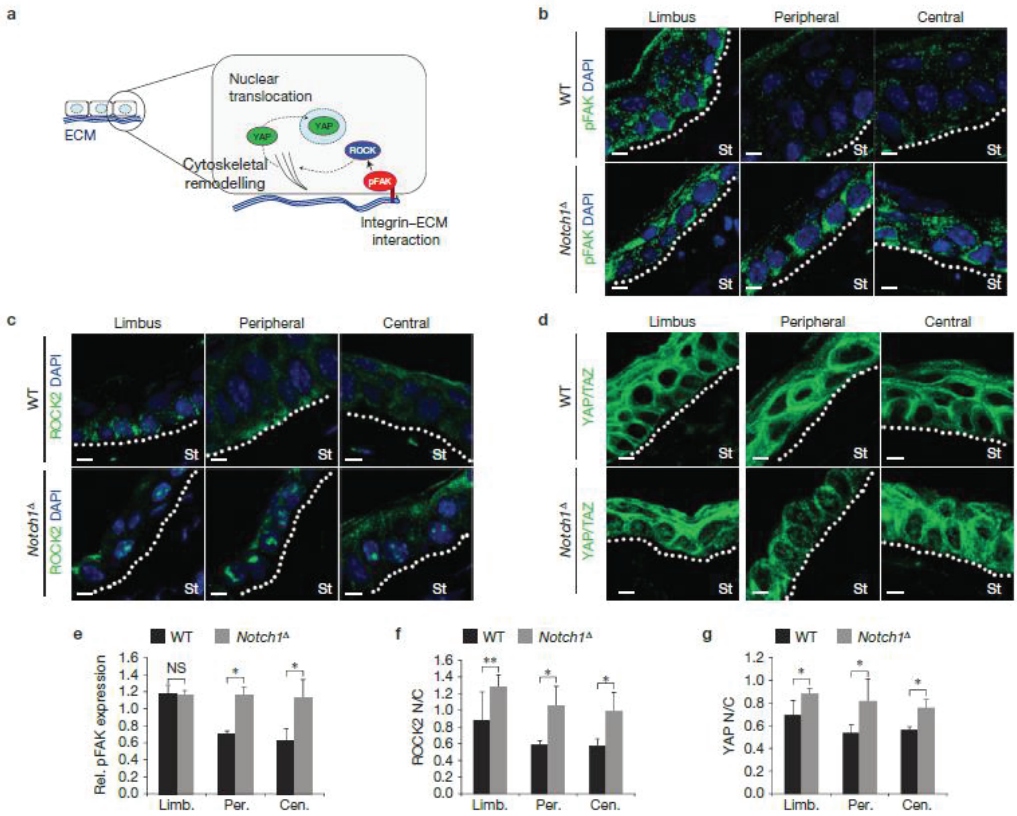

Figure 6.6 Activation of mechanotransduction in the corneal epithelium in response to aberrant inflammation. (a) Schematic depiction of key molecular mediators and/or sensors of mechanotransduction in epithelial cells. (b–d) Immunofluorescent staining for pFAK (b), ROCK2 (c) and YAP/TAZ (d) in the limbus, peripheral cornea and central cornea of WT (*Notch*$^{lox/lox}$) and *Notch1*$^{\Delta}$ mice 24 h after the second corneal injury. In d images without DAPI are shown to enable clearer visualization of nuclear YAP/TAZ. The images are representative of 6 corneas per genotype over three independent experiments. (e) Quantification of FAK phosphorylation in the limbus, peripheral cornea and central cornea 24 h after the second injury. Values for expression levels are relative values normalized to the expression level in the conjunctiva of each sample, determined by mean fluorescence intensity. Black bars, WT (*Notch*$^{lox/lox}$); grey bars, *Notch1*$^{\Delta}$ (n=6 corneas for each genotype over three independent experiments). (f,g) Quantification of nuclear/cytoplasmic ratio (N/C) of ROCK2 (f) and YAP/TAZ (g) in the limbus, peripheral cornea and central cornea 24 h after the second injury. n=6 corneas for each genotype over three independent experiments. St, stroma; NS, not significant. *P <0.01, **P <0.05 (unpaired, two-tailed t-tests). Error bars represent standard deviation. Scale bars represent 5 µm. White dotted lines indicate the boundary between the stroma and epithelium.

To gather additional evidence of a role for mechanotransduction, we determined whether ECM deposition resulted in changes in the mechanical properties of the corneal stroma by employing atomic force microscopy in combination with immunofluorescence. This enabled us to correlate the expression of ECM with tissue stiffness and revealed that increased expression of tenascin C in *Notch1*$^{\Delta}$ corneas correlated with increased stiffness of the corneal stroma compared with WT controls, an effect that was apparent at the limbus, peripheral CE and central CE (Figure 6.7a,b).

In light of the above data, we sought to establish a functional link between mechanotransduction and β-catenin signalling. We therefore obtained primary cultures of pig corneal epithelial stem cells (PCESCs), which can be readily cultivated *in vitro*, and determined the effect of mechanical stimuli by growing these cells on stiff versus soft substrates. Importantly, in this assay, PCESCs were cultured in the absence of feeder cells to promote differentiation. Strikingly, cells grown on stiff substrates expressed higher levels of β-catenin compared with cells grown on soft substrates, as well as exhibiting increased nuclear localization of YAP/TAZ and perturbed differentiation (Figure 6.7c-g). Moreover, PCESCs cultured on extremely stiff substrates (glass) in the presence of the ROCK inhibitor Y27632 expressed lower levels of β-catenin, exhibited reduced nuclear localization of YAP/TAZ and exhibited a higher propensity for corneal differentiation compared with cells maintained in vehicle (Supporting Figure 6.7a-e).

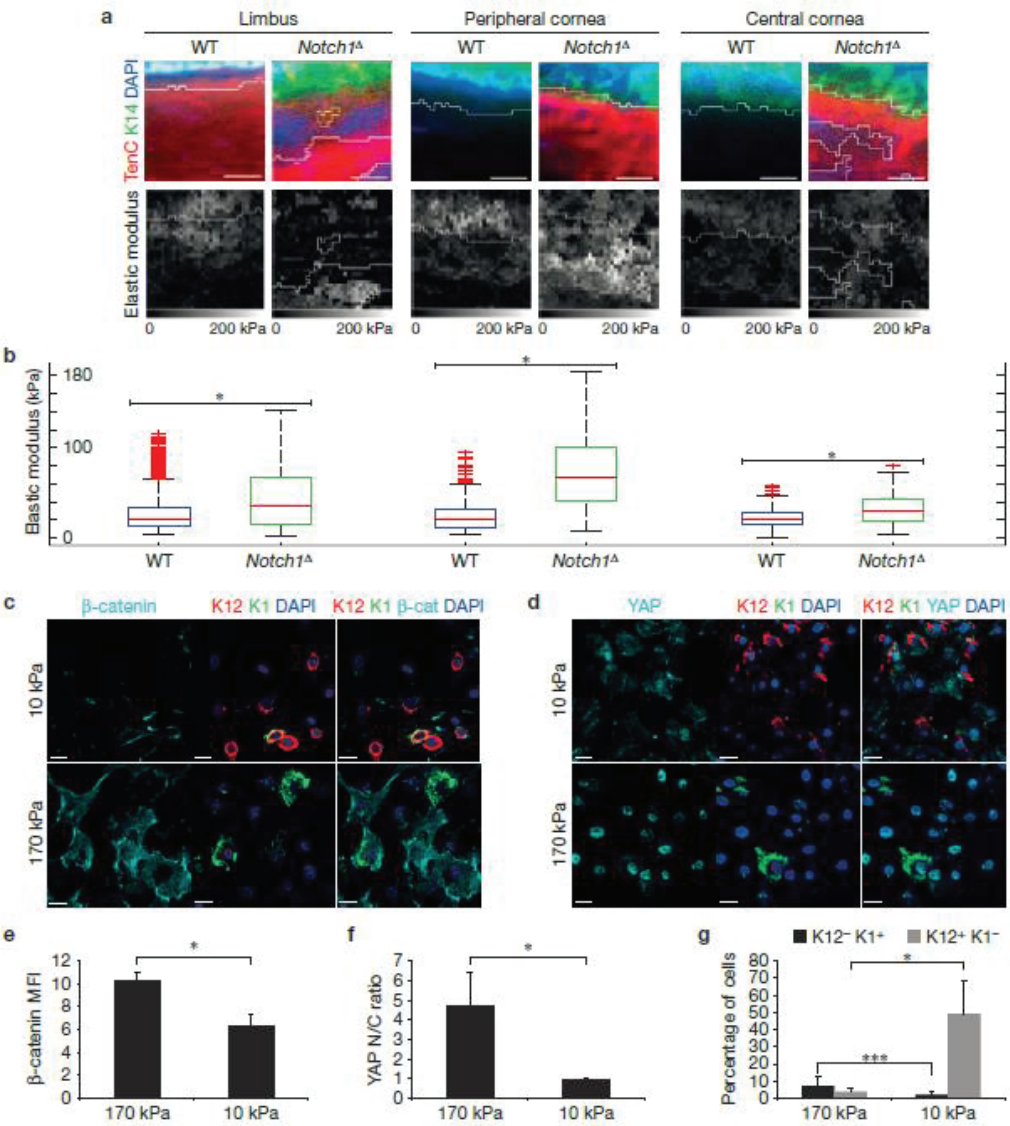

Figure 6.7 CSCM is associated with increased tissue stiffness and mechanical stimuli. (a) Immunofluorescence for K14 and tenascin C (upper panels) and corresponding atomic force microscopy (AFM) nanomechanical property measurement (lower panels) of limbus, peripheral cornea and central cornea after repeated injury. The elastic modulus was determined using AFM force–volume mode. Data are representative of 4 corneas per genotype over 4 independent experiments. (b) Quantification of the elastic modulus (kPa) of stromal tissue from the limbus (left), peripheral cornea (middle) and central cornea (right) of the regions shown in a. Red lines in each box represent the median elastic modulus value of force–volume measurements in the regions shown in a. Red lines in each whisker represent outliers. Boxes represent the middle 50% of the data. (c,d) Immunofluorescence for β-catenin, K12 and K1 (c) or YAP/TAZ, K12 and K1 (d) on PCESCs cultured on soft (upper panels) or stiff (lower panels) substrates. Data are representative of 6 individual cultures over 2 independent experiments. (e–g) Quantification of β-catenin expression (MFI, mean fluorescence intensity) (e), YAP/TAZ nuclear/cytoplasmic ratio (N/C) (f) and the proportion of $K12^{+}K1^{-}$ and $K12^{-}K1^{+}$ cells (g) in PCESCs cultured on soft or stiff substrates (nD6 for each condition over 2 independent experiments, where one replicate represents quantification from a single culture). For e, β-catenin expression is determined by mean fluorescence intensity. Scale bars in a represent 15 µm; scale bars in c and d represent 20 µm. *P <0.01, ***P <0.1 (unpaired, two-tailed t-tests). Error bars represent standard deviation (e–g) or maximal values/1.5x interquartile range (b).

Further evidence of a link between mechanotransduction and β-catenin signalling was provided by induction of TCF-luciferase activity in reporter cells following expression of a constitutively active ROCK2 kinase domain (Supporting Figure 6.7f-h), indicating that forced activation of the mechanotransduction cascade does indeed activate β-catenin signalling.

Collectively, these data support the hypothesis that activation of mechanotransduction is sufficient to promote elevated β-catenin activity in corneal epithelial cells and, in addition, suggest that this is a mechanism that is conserved across species.

6.3.5 Modulation of mechanotransduction cascades regulates cell fate on the ocular surface

To definitively establish that chronic inflammation promotes CSCM through mechanotransduction, we tested whether manipulation of the mechanotransduction cascade affects cell fate on the ocular surface *in vivo*. In the first instance, we determined whether inhibition of mechanotransduction could restore corneal differentiation in chronically inflamed *Notch1*$^{\Delta}$ corneas by using small-molecule inhibitors of FAK (PF562271) or ROCK (Y27632; Figure 6.8a). Strikingly, mice treated with either inhibitor retained a predominantly K12^{+}K1^{-} CE, despite the presence of a chronically inflamed stroma (Figure 6.8b-e), thus supporting the hypothesis that chronic inflammation elicits CSCM through activation of mechanotransduction. To test the hypothesis further, we performed the reciprocal experiment by ablating YAP/TAZ from the CE, thus removing cytoplasmic YAP/TAZ and recapitulating the effect of mechanotransduction. Thus, tamoxifen-treated *Yap* $^{lox/lox}$*:Taz* $^{lox/lox}$*:K14Cre*^{ERT} mice, in which *YAP* and *TAZ* are ablated in the CE (*YAP*$^{\Delta}$*:TAZ*$^{\Delta}$), were subjected to a single corneal injury and analysed 7 days later (Figure 6.8f). Strikingly, the ocular surface of *YAP*$^{\Delta}$*:TAZ*$^{\Delta}$ corneas exhibited overt epidermal differentiation, particularly in peripheral regions (Figure 6.8g), which correlated with loss of YAP/TAZ (Figure 6.8h) and increased β-catenin expression (Figure 6.8i). As expected, WT controls maintained corneal identity throughout the CE (Figure 6.8g-i).

Collectively, these data provide functional evidence that chronic inflammation induces CSCM by activating the mechanotransduction cascade.

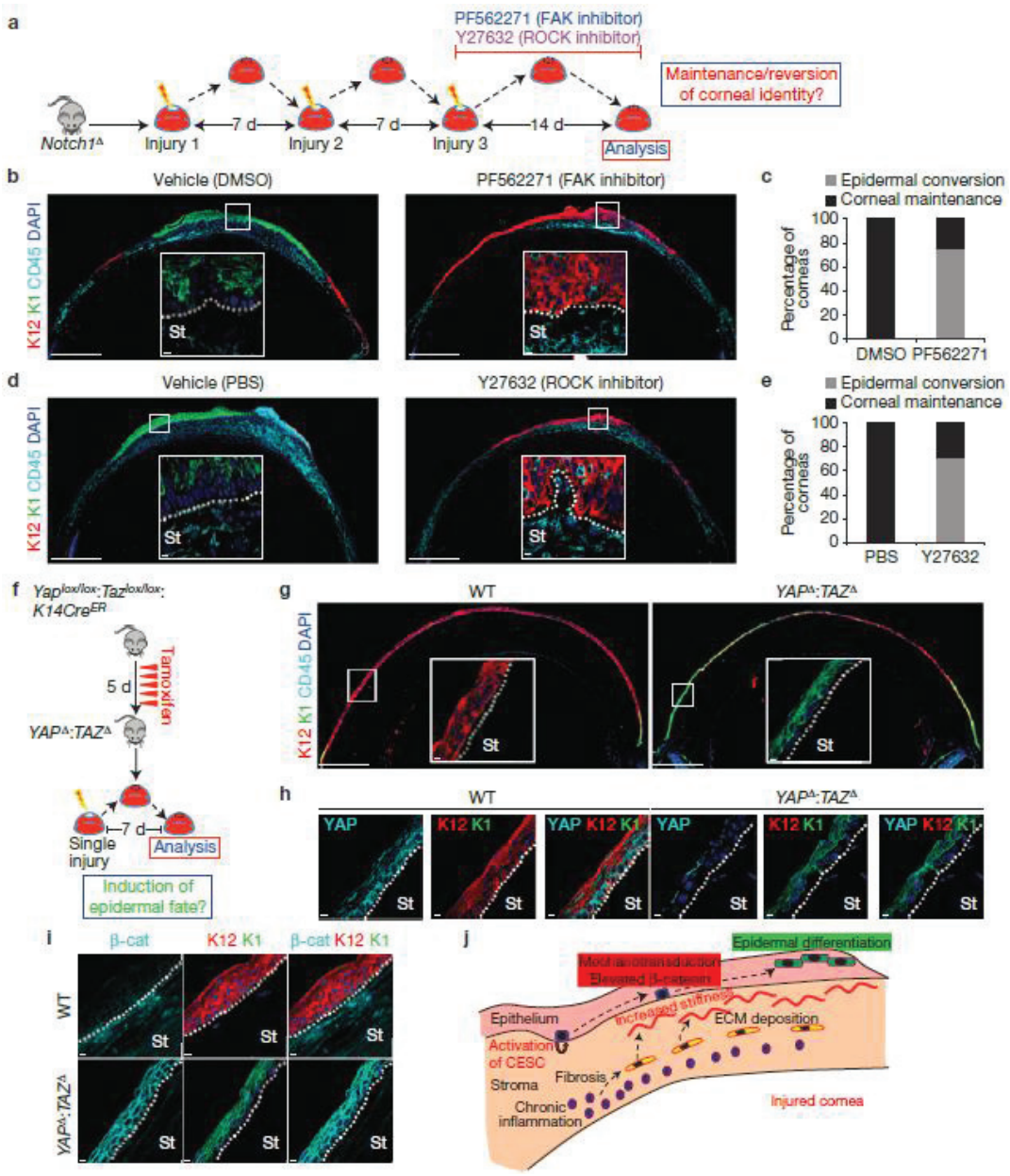

Figure 6.8 Manipulation of mechanotransduction affects corneal cell fate. (a) Schematic depiction of the experimental strategy used to determine whether inhibition of mechanotransduction prevents CSCM. (b) Immunofluorescent staining for K12, K1 and CD45 on *Notch1*$^{\Delta}$ corneas treated with vehicle (dimethylsulphoxide, DMSO) or the FAK inhibitor PF562271 during the procedure outlined in a. The images are representative of 8 corneas per treatment over four independent experiments. Large panels are low-magnification tiled images. Insets show high-magnification images of the indicated regions. (c) Quantification of the proportion of *Notch1*$^{\Delta}$ corneas exhibiting corneal or epidermal differentiation during wound closure following treatment with vehicle or PF562271 (n=8 corneas for each treatment over four independent experiments). (d) Immunofluorescent staining for K12, K1 and CD45 on *Notch1*$^{\Delta}$ corneas treated with vehicle (PBS) or the ROCK inhibitor Y27632 after the procedure outlined in a. The images are representative of 10 corneas per treatment over four independent experiments. Large panels are low-magnification tiled images. Insets show high-magnification images of the indicated regions. (e) Quantification of the proportion of *Notch1*$^{\Delta}$ corneas exhibiting corneal or epidermal differentiation during wound

closure following treatment with vehicle or Y27632 (n=10 corneas for each treatment over four independent experiments). (f) Schematic depiction of the experimental strategy used to determine whether ablation of *YAP/TAZ* is sufficient to induce CSCM during repair. (g) Immunofluorescent staining for K12, K1 and CD45 on WT (*Yap*$^{+/+}$*:Taz*$^{+/+}$*:K14Cre*^{ER}) and *YAP*$^{\Delta}$*:TAZ*$^{\Delta}$ corneas after the procedure outlined in f. The images are representative of 6 corneas for WT and 7 corneas for *YAP*$^{\Delta}$*:TAZ*$^{\Delta}$ isolated over two independent experiments. Large panels are low-magnification tiled images. Insets show high-magnification images of the indicated regions. (h,i) Immunofluorescent staining for YAP/TAZ, K12 and K1 (h) and β-catenin, K12 and K1 (i) in WT and *YAP*$^{\Delta}$*:TAZ*$^{\Delta}$ corneas as indicated. The images are representative of 6 corneas for WT and 7 corneas for *YAP*$^{\Delta}$*:TAZ*$^{\Delta}$ isolated over two independent experiments. (j) Model depicting how chronic inflammation imposes aberrant cell fate on corneal epithelia stem cells through increased tissue stiffness and mechanotransduction. Scale bars represent 500 µm on tiled images and 5 µm on all other images. St, stroma. White dotted lines indicate the boundary between the stroma and epithelium.

6.4 Discussion

In this study we have demonstrated that a central mechanism by which chronic inflammation can promote aberrant cell fate is through mechanotransduction (Figure 6.8j). The data presented support a model whereby exposure of the corneal stroma to chronic inflammation results in the induction of excessive ECM deposition, which subsequently promotes epidermal differentiation in the regenerating epithelium through mechanical induction of β-catenin signalling.

The mechanisms underlying ECM deposition in this model remain to be fully elucidated, although the expression of matrix components is confined to non-haematopoietic stromal cells, thus suggesting that the changes in the ECM occur owing to a fibrotic-like process. A variety of immune cells, including macrophages (*140*), neutrophils (*141*) and T cells (*142*), are linked to the induction of fibrosis through the secretion of cytokines such as TGF-β (*143, 144*) and IL-13 (*112, 145*), which subsequently induce excessive ECM deposition by α-SMA^{+} myofibroblasts (*146-148*). It will thus be interesting to determine whether similar cellular and molecular mechanisms are involved in the stromal remodelling observed in the chronically inflamed cornea. The profiles of inflammatory cell types in the corneal stroma of both WT and *Notch1*$^{\Delta}$ mice are similar following injury and consist predominantly of CD11b^{+}Gr1^{+} neutrophils, although the magnitude of the response is elevated in *Notch1*$^{\Delta}$ mice. However, the prolonged duration of the inflammatory response in Notch1 mutants seems to be critical for the induction of stromal remodelling and resulting metaplasia, as both of these effects occur following repeated cycles of injury and repair. Experiments in which specific inflammatory cell types and cytokines can be efficiently depleted will enable delineation of the specific cellular and molecular mediators involved and may identify promising targets for therapeutic intervention in ocular surface disorders.

The induction of CSCM in the model described here is initially induced in the limbus and peripheral corneal epithelium, locations that contain significant numbers of activated stem/progenitor cells following injury. In addition, it is notable that although there is a significant overlap between elevated β-catenin expression and CSCM, not all β-catenin^{hi} cells undergo epidermal fate conversion. This therefore suggests that only a proportion of epithelial cells on the anterior ocular surface are permissive to β-catenin-induced fate switching. Given that the induction of CSCM coincides temporally and spatially with the activation of stem/progenitor cells in the limbus and peripheral cornea, it is tempting to speculate that these cells represent uncommitted progenitor cells that retain the potency to form epidermis in response to elevated β-catenin. To formally

prove this hypothesis, phenotypic markers that precisely identify stem and progenitor cells in the corneal epithelium are required to definitively establish the cellular target of β-catenin-induced CSCM.

Finally, although this study demonstrates that mechanotransduction is a key mechanism by which chronic inflammation can impose aberrant cell fate, the mechanisms by which inflammation influences other aspects of stem/progenitor cell function are likely to be multifaceted. Notably, although inhibition of mechanotransduction and/or β-catenin signalling restores corneal identity in a chronic inflammatory environment, the epithelium remains hyperplastic. Thus, inflammation is likely to affect traits such as cell fate and proliferation through distinct mechanisms.

In summary, our findings demonstrate that chronic inflammation can promote aberrant cell fate through mechanotransduction and thus reveal an important mechanism by which aberrant inflammatory responses can promote the development of disease.

6.5 Methods

Ethics statement. All animal work was conducted in accordance with Swiss national guidelines. All mice were kept in the animal facility under EPFL animal care regulations. They were housed in individual cages at 23 °C ± 1 °C with a 12 h light/dark cycle. All animals were supplied with food and water ad libitum. This study has been reviewed and approved by the Service Veterinaire Cantonal of Etat de Vaud.

Mice. *Notch1*$^{lox/lox}$, *Ctnnb1*$^{lox/lox}$ and *K5Cre*^{ERT} mice were as previously described (*149-151*) and were maintained on a C57BL/6 background. cjun $^{lox/lox}$ mice were as previously described (*152*) and were provided by E.F.W. *Yap*$^{lox/lox}$ *:Taz*$^{lox/lox}$ *:K14Cre*^{ER} were as previously described (*95*) provided by S.P. These mice were backcrossed onto the C57BL/6 background. *Ctnnb1*$^{lox(ex3)}$ and *K14TSLPTg* mice were as previously described (*96, 97*) and were maintained on an sv129 background. The conditional mutant strains *Notch1*$^{lox/lox}$*:K5Cre*^{ERT}, *Notch1*$^{lox/lox}$*:Ctnnb1*$^{lox/lox}$*:K5Cre*^{ERT}, *Notch1*$^{lox/lox}$*:cjun*$^{lox/lox}$*:K5Cre*^{ERT} and *Ctnnb1* $^{lox(ex3)/lox(ex3)}$ were generated by performing the required inter-crosses and were maintained as homozygotes. For conditional ablation of YAP/TAZ, *Yap*$^{lox/lox}$ *:Taz*$^{lox/lox}$*:K14Cre*^{ER} mice were administered with 1mg tamoxifen once a day for 3 days by intraperitoneal injection. For all other gene activation/inactivation experiments, tamoxifen dissolved in peanut oil was administered once a day for 5 consecutive days by intraperitoneal injection at a dose of 50 mg kg^{-1}. For each experiment, all mice were age matched and were between 4 and 7weeks of age. Male and female animals were used. All mouse experiments were non-randomized and non-blinded; a minimum of three animals were used for each experiment, allowing a minimum of six corneas to be analysed for each experiment. This number was deemed sufficiently appropriate to account for normal variation, as determined from previous studies. Numbers of animals for each experiment are described in the figure legends. No statistical method was used to predetermine sample size.

Statistical analysis. For statistical analysis, unpaired two-tailed *t*-tests were performed on normally distributed data sets with equal variance assumed. Unless otherwise stated, *n* numbers for experiments stating statistical significance represent biological replicates. Sample size in

all cases was a minimum of 6 independent biological replicates, according to availability of biological material.

Corneal wounding. Mice were anaesthetized by sub-cutaneous injection of ketamine (100 mg kg^{-1}) and xylazine (10 mg kg^{-1}). Anaesthetic collrium (0.4% oxybuprocaine) was applied to the ocular surface to prevent corneal reflex.

To wound the ocular surface, a circular area 2 mm in diameter was marked on the central cornea by gentle application of a 2 mm biopsy punch. Removal of the epithelial tissue within this area was then achieved using a Demarres spatula (Moria Surgical) with a 45° cutting angle. The efficiency of wounding was monitored by application of 0.5% solution of ophthalmic fluorescein (Novartis). Following corneal wounding, Viscotears ophthalmic gel (Novartis) was applied to the ocular surface.

On waking, mice were administered with 0.3ml 0.9% NaCl solution (Braun) to aid recovery. Dafalgen analgesic was provided in the drinking water following corneal wounding at a concentration of 2 mg ml^{-1}.

Administration of Tobradex anti-inflammatory gel. Tobradex gel or ophthalmic lubricating gel was administered topically to the ocular surface once a day throughout the corneal wounding procedure, starting from the day of the first corneal wound and ending 21 days after the third corneal wound.

Administration of PF562271 (FAK inhibitor) and Y27632 (ROCK inhibitor). For systemic administration, PF562271 (Selleckchem) was dissolved in 70% DMSO/dH2O and injected i.p. at a dose of 30 mg kg^{-1} every other day for 14 days following the final corneal injury. Control mice were injected with 70% DMSO vehicle alone. For topical application, a 3 µl drop of 10 mM PF562271 was applied to the ocular surface twice a day for 14 days following the final corneal injury in a 15% DMSO solution (diluted in dH20). Control mice were administered with 15% DMSO vehicle alone.

For systemic administration, Y27632 (Sigma) was dissolved in saline solution and injected i.p. at a dose of 30 mg kg^{-1} every other day for 14 days following the final corneal injury. Control mice were injected with saline vehicle alone.

For topical application, a 3 µl drop of 10mM Y27632 diluted in saline was applied to the ocular surface twice a day for 14 days following the final corneal injury. Control mice were administered with saline vehicle alone.

Cell culture. Peripheral corneal epithelial cells were isolated from porcine corneas and cultivated on lethally irradiated 3T3-J2 feeder cells in 3:1 DMEM/F12 medium supplemented as previously described (*153*).

For experiments analysing the effect of substrate stiffness, cells were plated on glass coverslips, standard tissue culture plastic, 15% PEG or 2.5% PEG hydrogels in the absence of 3T3-J2 feeders at a density of 50,000 cells cm^{-2}. For experiments using the ROCK inhibitor Y27632, cells were seeded onto glass coverslips in the absence of 3T3-J2 feeders at a density of 50,000 cells cm^{-2}. All

substrates in feeder-free cultures were coated with recombinant human collagen I (AteloCell). Glass coverslips were treated with poly-L-lysine (Sigma) before collagen coating.

Hydrogel substrates were formed by crosslinking two branched PEG precursors of relative molecular mass 10,000, end-functionalized with either thiol (TH) or vinylsulphone (VS) groups (NOF Corporation). To adjust the stiffness the precursors were mixed at different mass to volume ratios. Fifty microliters of the mixed hydrogel precursor solution were transferred to each well of a 12-well plate (Falcon). A hydrophobic PDMS stamp with spacers was used to produce homogeneous and thin gel layers. The partially crosslinked hydrogel substrate was subsequently functionalized with Collagen I (AteloCell) under pressure for 2 h. The functionalized hydrogel layers were then washed with PBS and ultraviolet-sterilized.

Transient transfection of porcine corneal epithelial cells was performed using JetPEI transfection reagent (PolyPlus) according to the manufacturer's instructions. TCF-Luc 293T cells were maintained in DMEM supplemented with 10% FCS.

TCF-luciferase reporter assay. 293T cells with a stably integrated luciferase cassette containing upstream TCF-binding sites were a kind gift from J. Huelsken. To assay TCF-luciferase activity in the presence or absence of the murine ROCK2 kinase domain, TCF-Luc 293T cells were transiently co-transfected with pR2KD/pRenilla or pEGFP/pRenilla using JetPEI (PolyPlus) transfection reagent according to the manufacturer's instructions. Luciferase activity was subsequently analysed 36-48 h later using the Dual-Luciferase Reporter Assay System (Promega) and a Berthold Lumat Luminometer. Luciferase values were normalized to *Renilla*-luciferase values.

Preparation of corneal single-cell suspensions and flow cytometry. Whole corneal tissue was isolated from murine eyes, placed in ice-cold PBS and cut into small fragments using a scalpel blade. Corneal fragments were then digested in 2 mg ml^{-1} collagenase IV (Invitrogen)/PBS for 30-45 min at 37 °C with gentle shaking. The resulting cell suspensions were then passed through a 70 µm cell strainer into 1x HBSS/25mM HEPES/2% newborn bovine calf serum (staining medium). Cells were subsequently washed twice with staining medium and then stained according to standard flow cytometry protocols with the following monoclonal antibody conjugates: anti-CD45-Pacific blue (clone 30-F11, Invitrogen), anti-CD11b-PE (clone M1/70, Biolegend), anti-Gr-1-Alexa 647 (clone RB6-8C5, EPFL Protein Core Facility), anti-CD11c-APC-eFluor 780 (clone N418, eBiosciences), anti-B220-PECy7 (clone RA3-6B2, eBiosciences), anti-TCRB-APC-eFluor 780 (clone H57-597, eBiosciences), anti-CD4-PE (clone GK1.5, EPFL Protein Core Facility), anti-CD8-Alexa Fluor 647 (clone YTS169.4, EPFL Protein Core Facility), anti-F4/80-biotin (clone BM8, eBiosciences), Streptavidin-FITC (eBiosciences). Before analysis, propidium iodide (Sigma) was added to cell suspensions at a final concentration of 5 µg ml^{-1} to enable dead cell exclusion. Data acquisition was performed using a Cyan flow cytometer (Dako) and analysed using FlowJo software (Tree Star).

Molecular cloning and generation of the pR2KD plasmid. cDNA synthesis was performed using the Quantitect Reverse Transcription kit (Qiagen) on RNA isolated from mouse corneal tissue. The region of cDNA encompassing the first 417 amino acids of the amino-terminal kinase domain was subsequently PCR cloned in two fragments; a 641 bp 5´ fragment starting 12 bp upstream of the initiating ATG and a 659 bp 3´ fragment starting 591 bp downstream of the

initiating ATG. A 38 bp overlapping region was present in each fragment. The primers used to generate each fragment were as follows: 5´ fragment: Fwd 5´-AATT**GTCCAG**AATTCGGCGAAGCGGCATGAGC-3´; Rev 5´–TAAGCCCATGGAGTGTATTGC-3´; 3´ fragment: Fwd 5´-GTAGTGCTTGCACTGGATGC-3´; Rev 5´-**CTACTACTA**TCTAAAGTAGGTAAATCCTATAAAAGGCAGC-3´.

The above primers enabled the incorporation of a 5´ SalI site (bold underlined) and x 3 3´ STOP codons (bold double underlined) in the 5´ and 3´ fragments respectively.

Cycling conditions were as follows: 5´ fragment x 35 cycles of 94 °C, 30 s: 62 °C 30 s: 72 °C 30 s; 3´ fragment x 35 cycles of 94°C, 30 s: 60 °C 30 s: 72 °C 30 s.

PCR was performed using Q5 DNA polymerase (NEB) according to the manufacturer's instructions, with the addition of DMSO to a final concentration of 5%. Amplified fragments were cloned using the TOPO TA cloning system (Invitrogen).

The 5´ and 3´ fragments were inserted into an expression vector (pI-EGFP2) downstream of a CMV promoter/enhancer and upstream of an IRESEGFP cassette through a three-way ligation using SalI, NcoI (present in the overlapping region of each fragment) and Not-I restriction sites, resulting in the generation of pR2KD.

Tissue processing for histology. Fresh frozen and paraffin-embedded tissues were used for histological analysis. For fresh frozen tissue, whole eyes were embedded in OCT compound (TissueTek) using standard protocols. Eight-micrometre-thick sections were cut using a Leica CM1850 cryostat. Cryosections were stored at -80 °C.

For paraffin-embedded tissue, whole eyes were fixed in 4% PFA overnight at 4 °C. Fixed tissue was then processed using standard protocols and embedded in paraffin wax. Four-micrometre-thick sections were cut using a Thermo Scientific Microm HM325 microtome. Sectioned tissue was dried at 37 °C overnight and then stored at 4 °C.

Immunofluorescence using fresh frozen tissue. For immunofluorescence on fresh frozen tissue, cryosections were fixed in ice-cold acetone for 2 min and then air dried for 20 min at room temperature. Sections were then rinsed in PBS and incubated in 1%BSA/PBS/0.1% Tween20 for 30 min at room temperature to block nonspecific antibody binding. Primary antibody solutions diluted in PBS were then added at the appropriate dilution and incubated overnight at 4 °C or for 1 h at room temperature. The antibodies used and their dilutions were: anti-keratin 14 (rabbit polyclonal, Covance (PRB-155P-100), 1:500), anti-keratin 1 (rabbit polyclonal, Covance (AF 109), 1:500), anti-keratin 12 (goat polyclonal, Santa Cruz (sc-17101), 1:400), anti-ROCK2 (rabbit polyclonal, Abcam (ab71598), 1:100), anti-ROCK1 (rabbit IgG (EP786Y), Abcam, 1:100), anti-CD45 (rat IgG2b (30-F11), BDBiosciences, 1:200), anti-β-catenin (mouse IgG1 (14/beta-catenin), BD Biosciences, 1:50), anti-c-jun-phospho-S73 (rabbit polyclonal, Abcam (ab30620), 1:400), anti-FAK phospho-Y397 (rabbit polyclonal, Abcam (ab4803), 1:50), anti- periostin (mouse IgG (IC12), a gift from J. Huelesken, 1:1,000), anti-tenascin C (rat IgG1 (Mtn-12), Abcam, 1:400), anti-Ki67 (rabbit IgG (SP6), Abcam, 1:500).

Primary antibody solutions were then removed and sections were washed for 3 x 5 min in PBS/0.1% Tween 20. Sections were then incubated in the appropriate secondary antibody solutions diluted in PBS for 1 h at room temperature. The antibodies used and their dilutions were: donkey-anti-rabbit Alexa Fluor 488 (Molecular Probes, 1:800), donkey-anti-mouse Alexa Fluor 568 (Molecular Probes, 1:800), goat-anti-rat Alexa Fluor 568 (Molecular Probes, 1:1,000), donkey-anti-goat Alexa Fluor 568 (Molecular Probes, 1:600), donkey-anti-rabbit Alexa Fluor 647 (Invitrogen, 1:1,000), donkey-anti-rat Alexa Fluor 488 (Molecular Probes, 1:800), Donkey-anti-goat Alexa Fluor 488 (Molecular Probes, 1:800). DAPI (Sigma) was included in all secondary antibody solutions at a dilution of 1/4,000. Secondary antibody solutions were then removed and sections were washed for 3 x 5 min in PBS/0.1% Tween 20. A final rinse was performed in PBS and stained sections were then mounted in DABCO (Sigma) anti-fade mounting medium.

Immunofluorescence using paraffin-embedded tissue. Paraffin-embedded tissue sections were dewaxed and rehydrated and were then washed for 2 x 2 min in dH2O. Appropriate antigen retrieval was then performed depending on the primary antibody combinations used (see below for antigen retrieval conditions). Following antigen retrieval, sections were washed for 2 x 2 min in PBS at room temperature and then blocked in 1%BSA/PBS/0.1% Tween20 for 30 min at room temperature. Primary antibody solutions diluted in 1%BSA/PBS/0.1% Tween20 were then added at the appropriate dilution and incubated overnight at 4 °C or room temperature for 90 min. The antibodies used and their dilutions were: anti-keratin 1 (rabbit polyclonal, Covance (AF 109), 1:500), anti-keratin 12 (goat polyclonal, Santa Cruz (sc-17101), 1:400), anti-β-catenin (mouse IgG1 (14/beta- catenin), BD Biosciences, 1:50), anti-c-jun-phospho-S73 (rabbit polyclonal, Abcam (ab30620), 1:400), anti-YAP/TAZ (mouse IgG2a (63.7), Santa Cruz, 1:200). Primary antibody solutions were then removed and sections were washed for 3 x 5 min in PBS/0.1% Tween20. Secondary antibody solutions diluted in 1%BSA/PBS/0.1% Tween20 were then added at the appropriate dilution and incubated for 1 h at room temperature. The antibodies used and their dilutions were: donkey-anti-rabbit Alexa Fluor 488 (Molecular Probes, 1:800), donkey-anti-goat Alexa Fluor 568 (Molecular Probes, 1:600), donkey-anti-mouse Alexa Fluor 568 (Molecular Probes, 1:800). Secondary antibody solutions were then removed and sections were washed for 3 x 5 min in PBS/0.1% Tween20. A final rinse was performed in PBS and stained sections were then mounted in DABCO (Sigma) anti-fade mounting medium.

For YAP staining, a Mouse on Mouse blocking kit (Vectashield) was used and staining was performed according to the manufacturer's instructions.

Immunohistochemistry using paraffin-embedded tissue. For immunohistochemistry, antigen detection was performed using HRP-conjugated secondary antibodies combined with DAB (Sigma) revelation. Primary antibodies were as described for immunofluorescence. The staining procedure was as described for immunofluorescence with the addition of a peroxidase blocking step using 3% H_2O_2. The secondary antibodies used were: donkey-anti-mouse IgG-HRP (Jackson, 1:100), goat-anti-rabbit IgG-HRP (Jackson, 1:100).

Antigen retrieval for immunofluorescence/immunohistochemistry on paraffin-embedded tissue. For detection of keratin 12, keratin 1, phosphoS73-cjun and β-catenin, sections were incubated in 10 mM Tris/1 mM EDTA/0.05% Tween20 (pH 9.0) for 20 min at 95 °C.

For detection of Ki67, sections were incubated in 10 mM sodium citrate/0.05% Tween20 (pH 6.0) for 20 min at 95 °C.

Immunocytochemistry. Cells were rinsed in PBS, fixed in 4% PFA for 15 min at room temperature and then washed twice with ice-cold PBS. Permeabilization was performed by incubating the cells in PBS/0.25% Triton X-100 for 10 min at room temperature, followed by washing for 3 x 5 min in PBS. Cells were then incubated in 1%BSA/PBS/0.1% Tween20 for 30 min at room temperature to block nonspecific antibody binding. Primary antibody solutions diluted in1% BSA/PBS/0.1% Tween20 were then added and cells were incubated overnight at 4 °C. The primary antibodies used and their dilutions were: anti-actin (mouse IgG1 (ACTNO5 (C4)), Abcam, 1:20), anti-keratin 12 (guinea pig polyclonal (AP09545SU-N), Acris, 1:200), anti-keratin 1 (rabbit polyclonal, Covance (AF 109), 1:500), anti-β-catenin (mouse IgG1 (14/beta-catenin), BD Biosciences, 1:50), anti-YAP/TAZ (mouse IgG2a (63.7), Santa Cruz, 1:200), anti-Pax6 (rabbit polyclonal, Covance (PRB-278P-100), 1:500), anti-keratin 14 (rabbit polyclonal, Covance (PRB-155P-100), 1:500), anti-GFP (goat polyclonal, Abcam (ab6673), 1:400). Primary antibodies were removed and cells were washed for 3 x 5 min in PBS. Secondary antibody solutions diluted in 1%BSA/PBS/0.1% Tween20 were then added and cells were incubated for 1 h at room temperature. The secondary antibodies used and their dilutions were: goat- anti-mouse Alexa Fluor 488 (Molecular Probes, 1:1,000), donkey-anti-rabbit Alexa Fluor 647 (Molecular Probes, 1:1,000), donkey-anti-guinea pig biotin (Jackson, 1:200). For keratin 12 staining, an additional incubation in streptavidin Alexa Fluor 568 (Molecular Probes, 1:800) was required following incubation in the secondary antibody solutions. DAPI (Sigma) was included in all secondary antibody solutions. Cells were washed for 3 x 5 min in PBS and then mounted in DABCO (Sigma; when cells were grown on coverslips) or stored in PBS.

Whole-mount immunofluorescence. Whole corneal tissue was dissected from the surrounding eye tissue and then incubated in 20 mM EDTA/PBS (pH 7.4) at 37 °C for 45 min. The intact cornea was then placed epithelial side down onto Superfrost Plus histology slides (Thermo Scientific) and air dried for 3-5 min. Stromal tissue was then removed using forceps, leaving the intact corneal epithelium attached to the slide. The tissue was then fixed in ice-cold acetone for 2 min and then air dried for 20 min at room temperature. Immunofluorescent staining was performed using the protocols described for fresh frozen tissue.

Microscopy. Tiled images (fluorescent and bright-field) were acquired using a Leica DM5500 microscope fitted with Leica DFC 320 and DFC 350FX cameras. Confocal fluorescent images were acquired using a Zeiss LSM700 confocal microscope. Bright-field images were acquired using an Olympus AX70 microscope. Fluorescent images for immunocytochemistry experiments were acquired using an Olympus Cell XCELLENCE microscope fitted with a long-distance objective.

Image analysis. Quantification of β-catenin, K12, K1, pFAK, ROCK2, YAP/TAZ, tenascin C and periostin was performed using ImageJ software. For *in vivo* analyses, grid squares were used to specify regions corresponding to the limbus, peripheral CE and central CE. Mean fluorescence intensity was then measured bilaterally on 5 sections per cornea. Values were normalized

to the fluorescence intensity measured in the conjunctiva of each section. For *in vitro* analyses, fluorescence intensity was measured on a per cell basis in 5 fields for each replicate.

Protein extraction and western blotting. Protein was extracted from whole cultured cells in RIPA buffer using standard protocols. Protein samples were resolved by SDS-PAGE (8% acrylamide) and then blotted onto PVDF membranes (Peqlab) by wet transfer using standard protocols. Unspecific interactions were blocked by incubation in 5% milk (fat free) and then immunolabelling was performed using the following primary antibodies: anti-ROCK2 (rabbit polyclonal, Abcam (ab71598), 1:1,000), anti-actin (mouse IgG1 (ACTNO5 (C4)), Abcam, 1:2,000). Immunodetection was performed using the following HRP-conjugated secondary antibodies: anti-mouse IgG (GEHealthcare, 1:1,000), anti-rabbit IgG (GE Healthcare, 1:3,000). Revelation was performed using Pierce ECL Western Blotting Substrate (Thermo Scientific).

Quantitative real-time RT-PCR. Corneal epithelium was isolated from the underlying stroma by incubation in 20 mM EDTA/PBS (pH 7.4) containing RNA Later stabilization reagent for 45 min at 37 °C. Separated, intact corneal epithelium was then homogenized in Trizol reagent (Sigma) and total RNA was isolated according to the manufacturer's instructions and quantified using an ND-100 NanoDrop spectrophotometer (NanoDrop Technologies). First-strand cDNA synthesis was then performed using Quantitect reverse transcription kit (Qiagen). Real-time PCR reactions were performed using SYBR Green and a 7900HT Real-Time PCR System (both from Applied Biosystems) for 45 cycles. Specificity of the reactions was determined by melting curve analysis. Relative quantification was performed using the 2^{-DDCP} method. α-tubulin was used as the reference gene. Primer sequences were as follows: *Notch1*: Fwd 5´-CGCCCTTGCTCTGCCTAACG-3´, Rev 5´-TGCCACCATGGTCCACAACG-3´; *Wnt1*: Fwd 5´-ACAACAACGAGGCAGGGCG-3´, Rev 5´-GGGGAGGGAGGCTTGTGC-3´; *Wnt2*: Fwd 5´-TGCCAAGGAGAGGAAAGGC-3´, Rev 5´-TTCATGACTACCTGGATGGC-3´; *Wnt3a*: Fwd 5´-AACCGTCACAACAATGAGGC-3´, Rev 5´-TTTCTCTACCACCATCTCCG-3´; *Wnt4*: Fwd 5´-TTCACAACAACGAGGCTGGC-3´, Rev 5´-GGCTTGAACTGTGCATTCCG-3´; *Wnt7b*: Fwd 5´-TCTGCAACAAGATTCCTGGC-3´, Rev 5´-GCGACGAGAAAAGTCGATGC-3´; *Wnt10a*: Fwd 5´-TCGGAACAAAGTCCCCTACG-3´, Rev 5´-TCCGACGGAAACGTTCTTCG-3´; *Wnt10b*: Fwd 5´-ACAACAACAGGGTGGGACG-3´, Rev 5´-TGGAACGCTCCAGAGTTGC-3´; *GM-CSF*: Fwd 5´-CCTTGGAAGCATGTAGAGGC-3´, Rev 5´-ATATCTTCAGGCGGGTCTGC-3´; *IL-1β*: Fwd 5´-CATTGTGGCTGTGGAGAAGC-3´, Rev 5´-TGTCCATTGAGGTGGAGAGC-3´; *S100A8*: Fwd 5´-AACTGGAGAAGGCCTTGAGC-3´, Rev 5´-CCATCGCAAGGAACTCCTCG-3´; *S100A9*: Fwd 5´-CTTCTCAGATGGAGCGCAGC-3´, Rev 5´-ATACACTCCTCAAAGCTCAGC-3´; *IL-6*: Fwd 5´-CACATGTTCTCTGGGAAATCG-3´, Rev 5´-TCTTCATGTACTCCAGGTAGC-3´; *GCSF*: Fwd 5´-AAGTGCACTATGGTCAGGACG-3´, Rev 5´-ACTGTGGAGCTGGCTTAGGC-3´; *α-tubulin*: Fwd 5´-TCGTAGACCTGGAACCCACG-3´, Rev 5´-GGTAAATGGAGAACTCCAGC-3´.

Atomic force microscopy. Atomic force microscopy experiments were conducted with a Dimension Icon AFM scanner (Bruker) mounted on a custom-built support structure on top of an inverted optical microscope (IX71, Olympus). A 20-µm-diameter bead (510-0166, VWR) was glued on the Lever D of a HYDRA-ALL- G (AppNano) cantilever. The spring constant determined by the thermal noise method (*154*) was 0.12 N m^{-1} and the same cantilever was used for all ex-

periments. Force-volume measurements with 32 by 32 indentations over an area of 50 µm by 50 µm were taken at a rate of 1 Hz to a maximum force of 11.5 nN.

The elastic modulus on the approach direction of force curves was calculated assuming the Hertz contact model (*155*). Subsequent analysis of elastic modulus maps was done using Matlab.

Fluorescence images were taken with a 20x objective (LUCPanFLN 20X, Olympus) and 2x magnifier in position with an iXon Ultra 897 (Andor) EMCCD camera. Illumination was achieved with a halogen lamp (U-HGLGPS, Olympus) and appropriate filter sets (MDF-GFP (Thorlabs) for K14-Alexa488, U-MNG2 (Olympus) for TenC-Alexa568, and F31-000 (AHF Analysentechnik AG) forDAPI). The relevant area was cropped and binned to a resolution of 32 by 32 pixels using standard image processing software to match the resolution obtained by AFM force-volume measurements. For wild-type samples, the image regions were segmented into regions of epithelium and stroma by applying a threshold on summed up intensity values from the fluorescent signals of K14-Alexa488 and DAPI, respectively. For mutant samples an additional intensity threshold on the fluorescent intensity of TenC-Alex568 was applied. Then ratios and standard deviations of the average elastic modulus values of the particular areas (epithelium and stroma) were calculated.

6.6 Acknowledgments

This work was supported in part by OptiStem, the Swiss National Science Foundation, the Swiss Cancer League, the Marie Curie Foundation and EuroSystem. P.D.O. and G.E.F. acknowledge financial support from the Swiss National Science Foundation under award number 205321_134786 and 205320_152675 and European Union FP7/2007-2013 ERC under Grant Agreement No. 307338-NaMic. Work performed in the laboratory of S.P. was supported by grants from AIRC (5x1000 and PI) and the ERC. We thank R. Kemler (Max Planck Institute of Immunobiology and Epigenetics, Freiburg, Germany) for providing the conditional _-catenin mice, M. Taketo (Centre for Frontier Medicine, Kyoto University, Japan) for the Ctnnb11Ex3 mice and P. Chambon and D. Metzger (Institute of Genetics and Molecular and Cellular Biology, Strasbourg, France) for the K5Cre^{ERT} and K14Cre^{ERT2} mice. We thank J. Huelsken (Swiss Institute for Experimental Cancer Research, EPFL, Lausanne, Switzerland) for providing the TCF-luciferase reporter cells and the anti-periostin antibody. We would like to thank A. Radenovic, J. Artacho, J. Sordet-Dessimoz and M. Garcia for technical assistance with microscopy, histology and flow cytometry. We would like to thank G. Ferrand for guidance and advice concerning animal experiments.

6.7 Author contributions

C.S.N. designed and performed experiments, analysed data and wrote the manuscript. P.D.O. performed nanomechanical measurement experiments and analysed data. L.A. performed experiments and analysed data. S.H. performed experiments and analysed data. E.F.W., G.E.F., M.P.L., Y.B. and S.P. analysed data and provided conceptual and experimental guidance throughout the study. F.R. conceived the study and analysed data.

6.8 Supporting Information

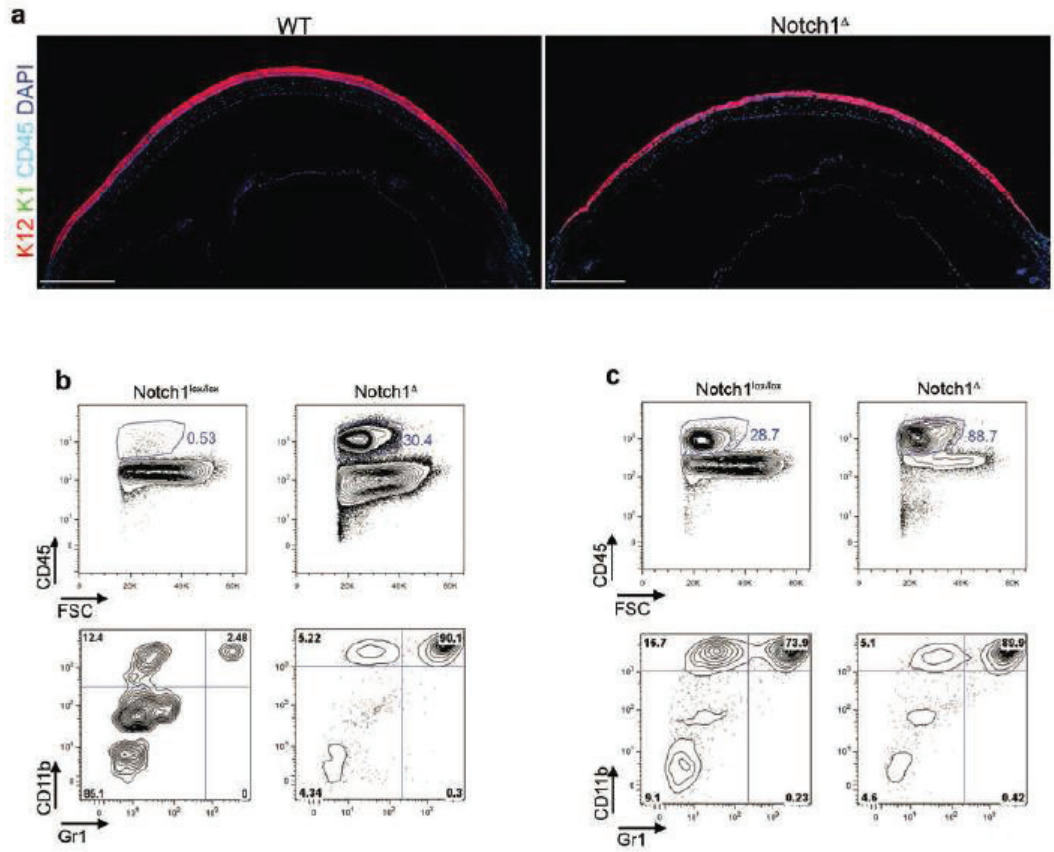

Supporting Figure 6.1 Inflammation in *Notch1*$^{\Delta}$ mice following corneal injury. (a) Immunofluorescent staining for K12, K1 and CD45 in unwounded WT (*Notch1*$^{lox/lox}$) and *Notch1*$^{\Delta}$ corneas. Data are representative of 6 corneas over three independent experiments. (b) Flow cytometric analysis showing the proportion of total CD45^{+} cells (upper plots) and CD45^{+}CD11b^{+}Gr1^{+} cells (lower plots) in WT (*Notch1*$^{lox/lox}$) and *Notch1*$^{\Delta}$ cornea 21 days after the repeated injury procedure (see Figure 6.1a). Data are representative of 6 individual analyses performed on cells pooled from 4 corneas of each genotype over three independent experiments. (c) Flow cytometric analysis showing proportion of total CD45^{+} cells (upper plots) and CD45^{+}CD11b^{+}Gr1^{+} cells (lower plots) in WT (*Notch1*$^{lox/lox}$) and *Notch1*$^{\Delta}$ cornea 24 hours after a single injury. Data are representative of 6 individual analyses performed on cells pooled from 4 corneas of each genotype over three independent experiments. Scale bars represent 500 µm.

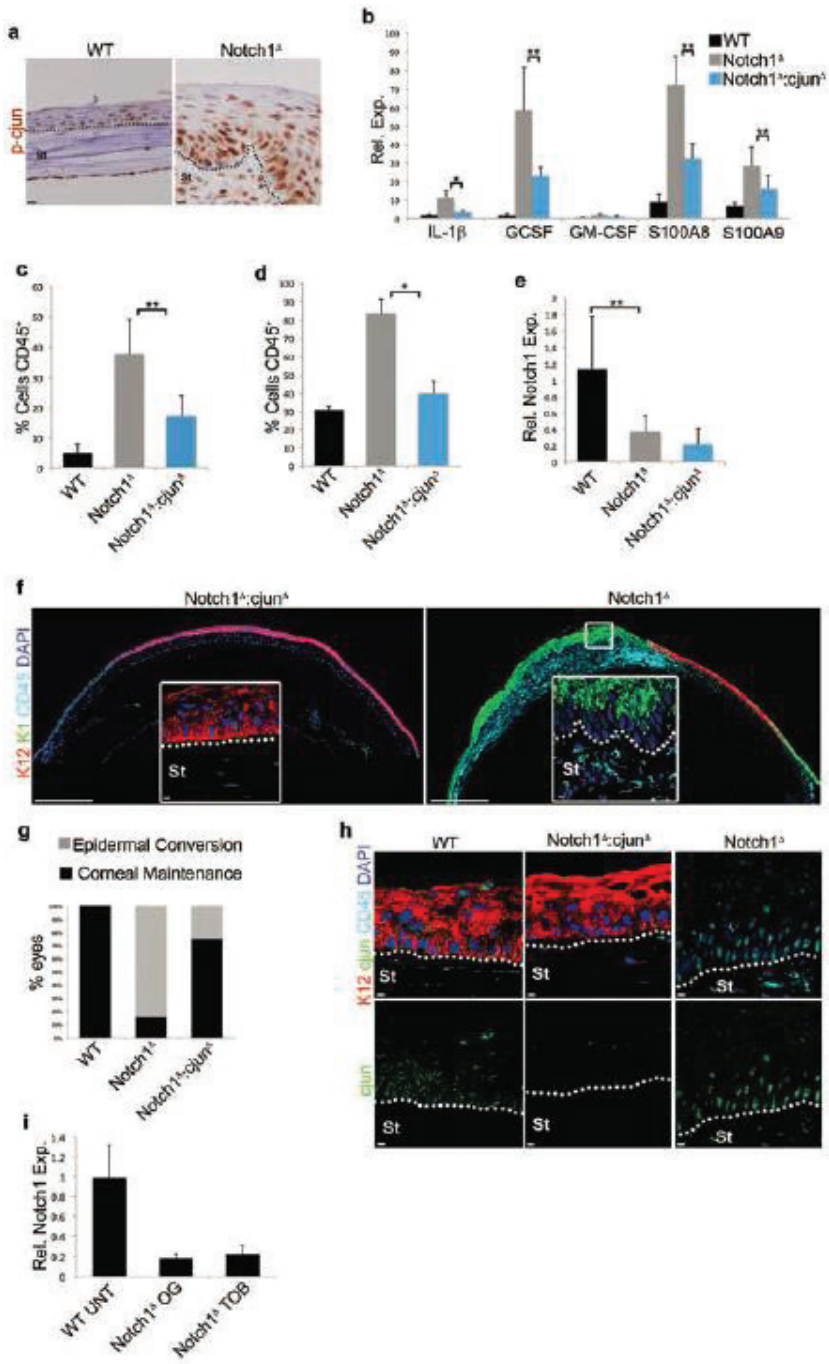

Supporting Figure 6.2 Chronic inflammation is associated with CSCM in *Notch1Δ* mice. (a) Immunohistochemistry for pS73cjun following repeated corneal injury. (b) QRT-PCR analysis for the indicated cytokines in WT (*Notch1*$^{lox/lox}$*:cjun*$^{lox/lox}$), *Notch1*$^{\Delta}$ and *Notch1*$^{\Delta}$*:cjun*$^{\Delta}$ corneal epithelial cells 24 hours after a single corneal injury (n = 6 biological replicates for each genotype over three independent experiments. Each replicate consists of corneal epithelial tissue pooled from 6 corneas isolated from 3 mice of each genotype). Data are expressed relative to the expression in WT unwounded corneal epithelial cells. (c,d) Quantification of the proportion of CD45^{+} cells in WT (*Notch1*$^{lox/lox}$*:cjun*$^{lox/lox}$), *Notch1*$^{\Delta}$ and *Notch1*$^{\Delta}$*:cjun*$^{\Delta}$ cornea 21 days after repeated corneal injury (c) or 24 hours after a single corneal injury (d). Proportions were measured by performing flow cytometry on dissociated corneas. (n = 6 biological replicates for each geno-

type over three independent experiments. Each replicate consists of cells pooled from 4 corneas isolated from 2 mice of each genotype). (e) QRT-PCR analysis of Notch1 in the corneal epithelium of WT (*Notch1*$^{lox/lox}$*:cjun*$^{lox/lox}$), *Notch1*$^{\Delta}$*:cjun*$^{\Delta}$ and *Notch1*$^{\Delta}$ mice following repeated injury (n = 6 biological replicates for each genotype over three independent experiments. Each replicate consists of corneal epithelial tissue pooled from 6 corneas isolated from 3 mice of each genotype). (f) Representative immunofluorescent staining for K12, K1 and CD45 in *Notch1*$^{\Delta}$*:cjun*$^{\Delta}$ and *Notch1*$^{\Delta}$ corneas following repeated corneal injury. Large panels are low magnification tiled images. White outlined insets show high magnification images of the indicated regions. (g) Proportion of WT (*Notch1*$^{lox/lox}$*:cjun*$^{lox/lox}$)(n = 10 corneas), *Notch1*$^{\Delta}$ (n = 20 corneas) and *Notch1*$^{\Delta}$*:cjun*$^{\Delta}$ (n = 16 corneas) corneal tissue exhibiting corneal or epidermal identity after repeated corneal injury. (h) Immunfluorescent staining for K12, K1, cjun (pS73) and CD45 on corneal tissue isolated from WT (*Notch1*$^{lox/lox}$*:cjun*$^{lox/lox}$), *Notch1*$^{\Delta}$*:cjun*$^{\Delta}$ and *Notch1*$^{\Delta}$ mice after repeated corneal injury. Data are representative of 16 corneas. (i) QRT-PCR analysis of Notch1 in the corneal epithelium of WT (*Notch1*$^{lox/lox}$) and *Notch1*$^{\Delta}$ mice treated with ophthalmic lubricating gel or Tobradex following repeated injury (n = 6 biological replicates for each treatment over three independent experiments. Each replicate consists of corneal epithelial tissue isolated during corneal wounding of a single eye). Scale bars represent 500 µm on tiled images and 5 µm on all other images. St – Stroma. * P <0.01, ** P<0.05 (unpaired, two tailed t-tests). Error bars represent standard deviation.

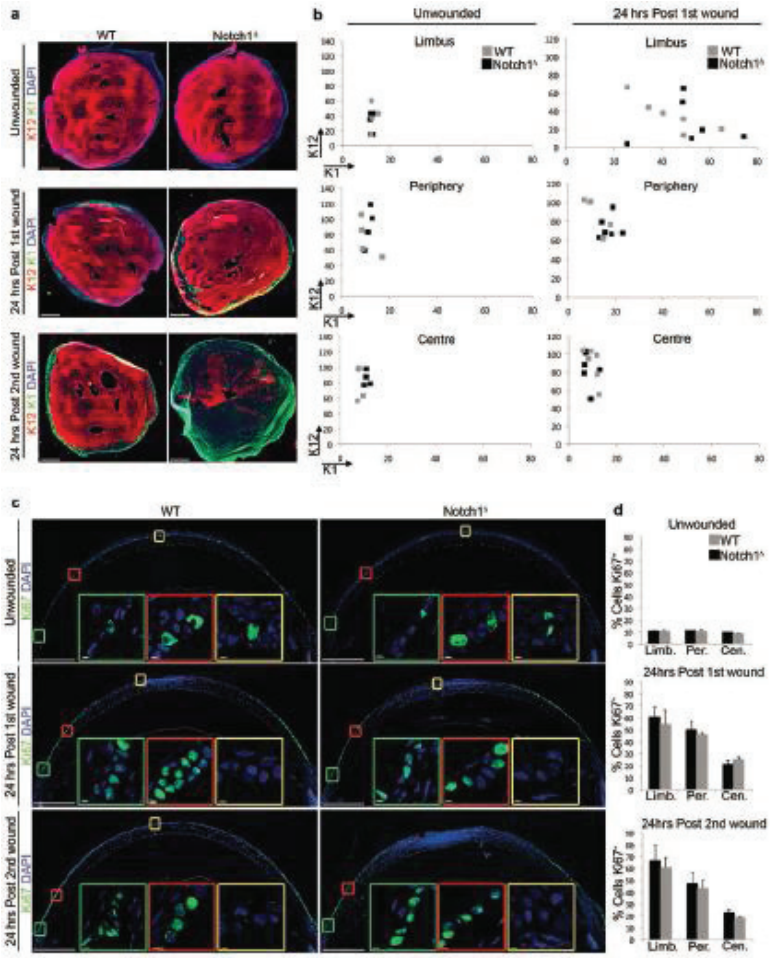

Supporting Figure 6.3 Spatial and temporal kinetics of CSCM (a) Representative immunofluorescent staining for K12 and K1 on wholemount corneal epithelial tissue isolated from WT and *Notch1*$^{\Delta}$ corneas. Upper panels show unwounded corneas, middle panels show corneal epithelial tissue 24 hours after the first injury, lower panels show corneal epithelial tissue 24 hours after the second injury. Data are representative of 6 corneal wholemounts over three independent experiments. (b) XY scatter plots showing K12 and

K1 expression in limbus, peripheral cornea and central cornea in unwounded corneas and in corneas isolated 24 hours after the second corneal injury. Each data point represents mean fluorescence intensity measured from an individual cornea. Grey boxes = WT (*Notch1*$^{lox/lox}$), black boxes = *Notch1*$^{\Delta}$ (n = 6 corneas for each genotype over three independent experiments). (c) Immunofluorescent staining for Ki67 on WT and *Notch1*$^{\Delta}$ corneas. Data are representative of 6 corneas. Upper panels show unwounded corneas, middle panels show corneal tissue 24 hours after the first injury, lower panels show corneal tissue 24 hours after the second injury. Large panels are low magnification tiled images. Insets outlined in green, red and yellow show high magnification images of the limbus, peripheral cornea and central cornea respectively. (d) Quantification of the proportion of Ki67^{+} cells in the limbus, peripheral cornea and central cornea in unwounded corneas (upper panels), corneas 24 hours after the first injury (middle panels) and corneas 24 hours after the second injury (lower panels). Black boxes = WT (*Notch1*$^{lox/lox}$), grey boxes = *Notch1*$^{\Delta}$ (n = 6 corneas for each genotype over three independent experiments). Scale bars represent 500 µm on tiled images and 5 µm on all other images. St – Stroma, Limb – limbus, Per – Periphery, Cen – Centre. Error bars represent standard deviation.

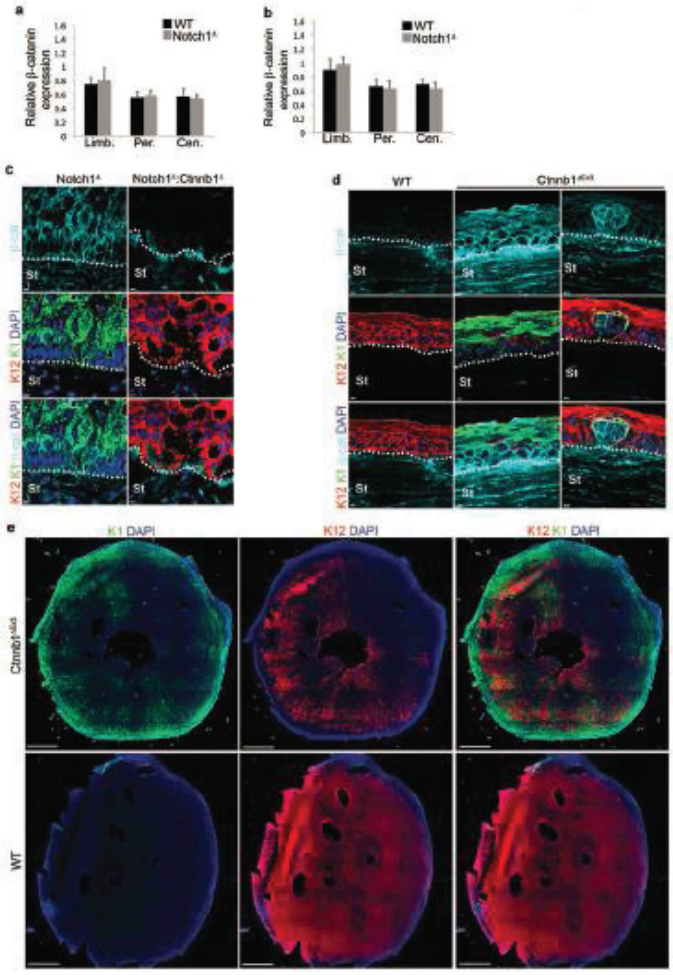

Supporting Figure 6.4 Elevated β-catenin is necessary and sufficient to induce CSCM. (a-b) Quantification of relative β-catenin expression in limbus, peripheral cornea and central cornea in unwounded eyes (a) and 24 hours after the first injury (b). Black bars = WT (*Notch1*$^{lox/lox}$), grey bars = *Notch1*$^{\Delta}$ (n = 6 corneas for each genotype over three independent experiments). Values for expression levels are relative values normalized to the expression level in the conjunctiva of each sample, determined by mean fluorescence intensity. (c) Immunofluorescent staining for β-catenin, K12 and K1 on *Notch1*$^{\Delta}$ and *Notch1*$^{\Delta}$*:Ctnnb1*$^{\Delta}$ corneas after repeated injury. Data are representative of 8 corneas for each genotype over 3 independent experiments. (d) Immunofluorescent staining for β-catenin, K12 and K1 on WT (*Ctnnb1*$^{lox(Ex3)/lox(Ex3)}$) and *Ctnnb1*$^{\Delta Ex3}$ corneas 7 days after a single injury. Data are representative of 8 WT corneas and 10 *Ctnnb1*$^{\Delta Ex3}$ corneas over 4 independent experiments. (e) Immunofluorescent staining for K12 and K1 on wholemount corneal epithelial tissue isolated from or WT (*Ctnnb1*$^{lox(ex3)/lox(ex3)}$) or *Ctnnb1*$^{\Delta Ex3}$ corneas 7 days after a single corneal injury. Data are representative of 6 WT and 8 *Ctnnb1*$^{\Delta Ex3}$ corneas over 3 independent experiments. Scale bars represent 500 µm on tiled wholemount images and 5 mm on all other images. Error bars represent standard deviation.

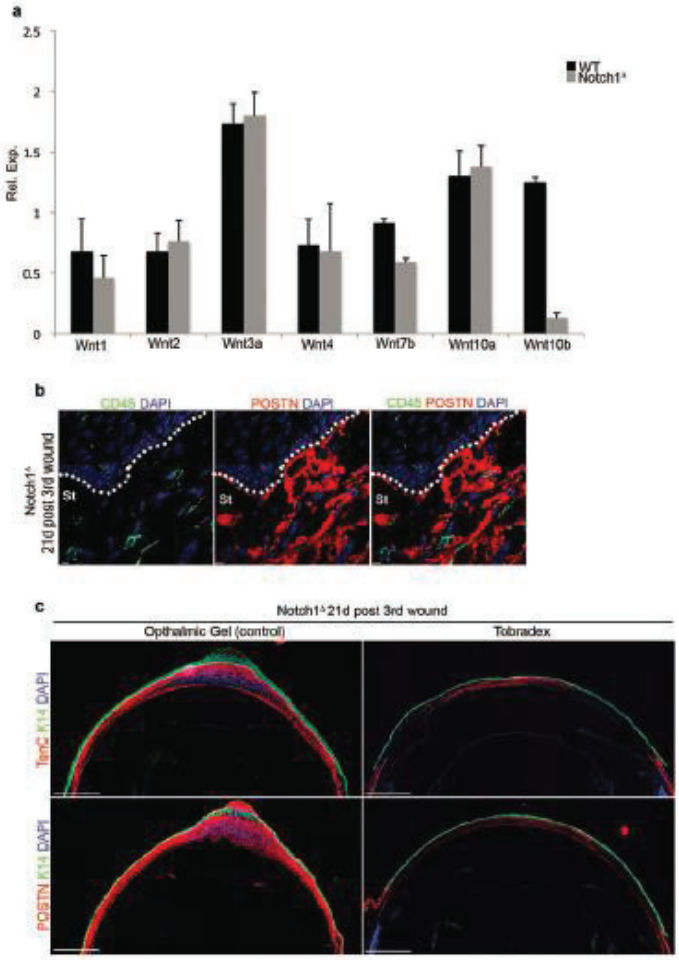

Supporting Figure 6.5 Inflammation induced CSCM is associated with increased ECM deposition in the corneal stroma. (a) QRT-PCR analysis of Wnt ligands that exhibit expression in corneal tissue after repeated injury. Analysis was performed on whole corneal tissue isolated from WT (*Notch1*$^{lox/lox}$) and *Notch1*$^{\Delta}$ mice 21 days after the 3rd corneal injury (n = 5 biological replicates for each genotype over four independent experiments. Each replicate consists of corneal epithelial tissue pooled from 4 corneas isolated from 2 mice of each genotype). Data are expressed relative to the expression in whole corneal tissue isolated from unwounded mice. Error bars represent standard deviation. (b) Immunofluorescence for Periostin, CD45 and DAPI on chronically inflamed *Notch1*$^{\Delta}$ corneal tissue after repeated injury. Single fluorescent images and merges are shown as indicated. Data are representative of 4 corneas analysed over two independent experiments. Scale bars represent 5 mm. (c) Immunofluorescent staining for K14 and Tenascin C (upper panels) or K14 and Periostin (lower panels) in *Notch1*$^{\Delta}$ mice treated with either ophthalmic gel (control) or Tobradex during the repeated injury procedure. Data are representative of 6 corneas analysed over three independent experiments. Scale bars represent 500 µm.

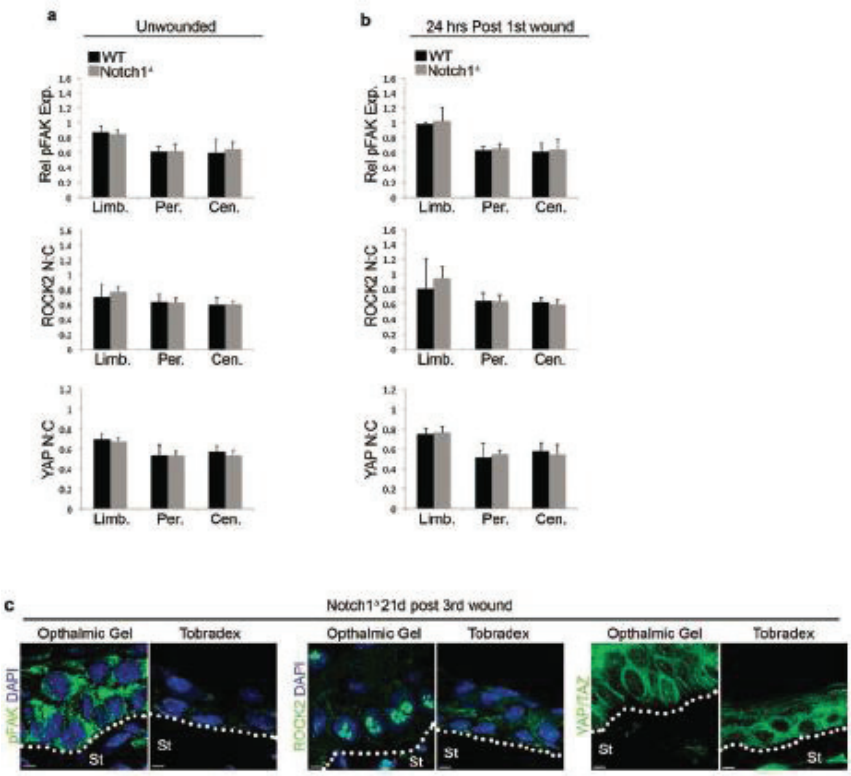

Supporting Figure 6.6 CSCM is associated with mechanotransduction. (a,b) Quantification of FAK phosphorylation (upper panels) and nuclear:cytoplasmic ratio of ROCK2 (middle panels) and YAP/TAZ (lower panels) in the limbus, peripheral cornea and central cornea isolated from unwounded eyes (a) or eyes isolated 24 hours after the first corneal injury (b). Values for expression levels are relative values normalised to the expression level in the conjunctiva of each sample, determined by mean fluorescence intensity. Black bars = WT (*Notch1*$^{lox/lox}$), grey bars = *Notch1*$^{\Delta}$ (n=6 corneas for each genotype over three independent experiments). Error bars represent standard deviation. (c) Immunofluorescence for pFAK, ROCK2 and YAP/TAZ on corneal tissue isolated from *Notch1*$^{\Delta}$ mice treated with ophthalmic gel (control) or Tobradex during the repeated injury procedure. Data are representative of 6 corneas for each treatment analysed over three independent experiments. Scale bars represent 5 µm.

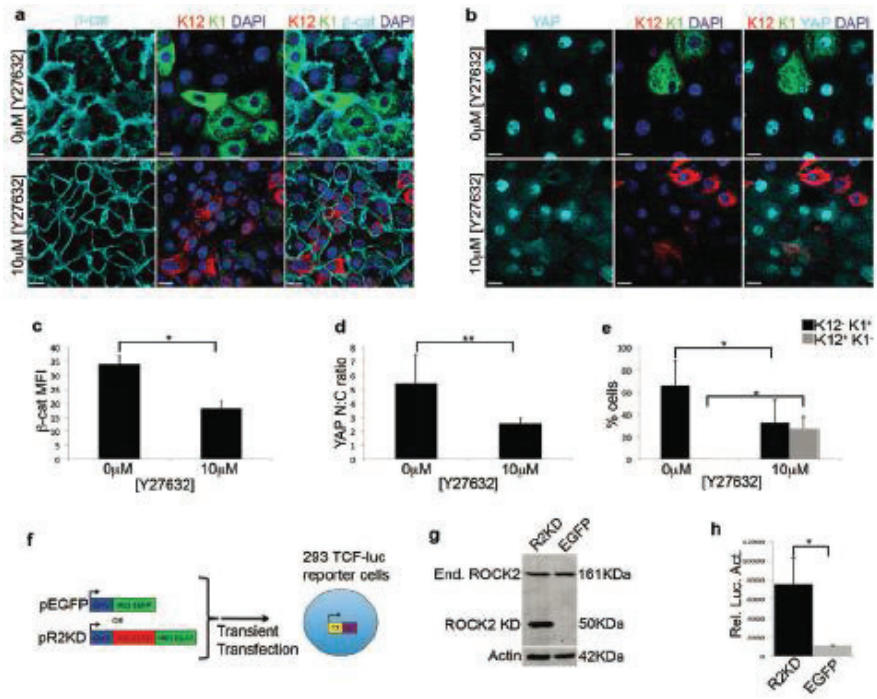

Supporting Figure 6.7 Manipulation of mechanotransduction affects Δ-catenin expression in corneal epithelial cells. (a,b) Immunofluorescence for β-catenin, K12 and K1 (a) or YAP/TAZ, K12 and K1 (b) on PCESCs cultured on stiff (glass - >2GPa) substrates and maintained in vehicle (PBS – upper panels) or 10 μM Y27632 lower panels). Data are representative of 8 individual cultures for each condition. (c-e) Quantification of β-catenin expression (c), YAP/TAZ nuclear:cytoplasmic ratio (d) and the proportion of $K12^{+}K1^{-}$ and $K12^{-}K1^{+}$ cells (e) in PCESCs maintained in vehicle (PBS) or 10 μM Y27632 (n = 8 individual cultures over four independent experiments). For (c) β-catenin expression is determined by mean fluorescence intensity. (f) Schematic depicting the transfection of TCF-Luc 293 T cells with pR2KD or pEGFP. (g) Western blot performed on TCF-Luc 293T cells 48 hours after transfection with pR2KD or pEGFP. (h) Relative luciferase activity in TCF-Luc 293 T cells 48 hours after transfection (n = 6 individual transfections over three independent experiments). * P <0.01, ** P<0.05, (unpaired, two tailed t-tests). Error bars represent standard deviation. Scale bars represent 20 μm.

Chapter 7 Conclusion

7.1 Achieved Results

The combination of a HS-AFM and an inverted optical microscope on a low noise platform enabled nanomechanical measurements and fluorescence imaging in a correlative way. As both imaging modalities are capable of imaging in buffer living biological samples could be measured. The high-resolution structural and mechanical information can thus be linked to the dynamics of specific proteins provided by FM. Nanomechanical properties of the sample can thus be linked to specific steps and processes of the cell cycle, or related to the protein composition of the sample.

The design of the implementation allowed the extension from conventional FM to sinlge molecule localization microscopy increasing the resolution by a factor of ~10, a resolution similar to AFM. This allowed individual protein clusters to be resolved which could then be followed during assembly and disassembly in time-resolved PALM imaging. The HS-AFM data provided the structural context and dynamics of the cell membrane.

HS-AFM measurements in the milliseconds range showed the kinetics of the sibling cell separation of *M.smegmatis.* This last step in the division process is governed by the mechanical properties of the outer cell wall and the mechanical tension built up. Time-resolved nanomechanical measurements correlated with functional imaging by FM showed that tension is being built up during septation at the septum. Once the tensile stress exceeds the ultimate tensile strength the sibling cells separate. Moreover, the separation can even be induced solely by applying additional mechanical load on the septum. This demonstrates that the mechanical properties dictate the timepoint of sibling cell separation and shows how this is linked to the progression of the cell cycle.

On a longer time scale, time-lapse AFM imaging of *M.smegmatis* over many generations revealed morphological surface features described as wave-troughs. These wave-troughs are established at the poles where the bacterium is growing and migrate towards the center as the cell grows. Cell division is closely correlated to these features and happens in the region of the center-most wave-trough. Correlated AFM/FM measurements in a mutant defective of proper chromsome segragation indicates that chrosome segregation influences which wave-trough is chosen as the division site. This would suggest a model where among the potential specified division sites the choice falls on one that is minimally blocked by colocalization of the chromosome.

The capability of taking quantitative mechanical measurements by AFM allowed to correlate the stiffness of the tissue with the distribution of ECM proteins. It shows that enhanced deposition of ECM proteins due to a chronic inflammation correlated with an increase in tissue stiffness.

The increased tissue stiffness eventually leads to a pathological disorder where stem cells acquire an aberrant character.

7.1.1 Design, implementation and testing of a new platform to integrate HS-AFM and OM

The integration of an AFM and inverted OM into one instrument demands specific requirements to ensure the proper functioning of both microscopes. Mechanical stability is of paramount importance for the AFM in order to reduce mechanical vibrations which otherwise deteriorate the image quality. In order to place an inverted optical microscope below the AFM the bottom side of the sample needs to be freely accessible. This allows high numerical aperture objective lenses to be positioned close to the sample, allowing TIRF illumination to be used for super-resolution imaging techniques. The platform developed here to combine these microscopes is based on the idea to mechanically decouple the two microscopes, thereby increasing the performance of the AFM while maintaining the functions of the inverted optical microscope. This improved the noise performance of the AFM by a factor of more than 3 compared to the conventional design (Figure 2.1). This design, and the implementation is enabling high resolution AFM and super resolution microscopy imaging.

7.1.2 Correlated HS-AFM and SMLM on biological samples

Correlated AFM and SMLM measurements were conducted after the successful integration of the AFM and inverted OM. To demonstrate the performance of each imaging modality on this system we imaged F-actin, a well characterized sample of known structure (Figure 3.2). After development of experimental protocols aimed at a sample preparation meeting AFM and SMLM requirements alike we acquired images accordingly to demonstrate the performance. The periodicity of the F-actin single left handed generic helix could be determined from the high resolution AFM images as well as an accurate height measurement. The measured FWHM achieved by dSTORM was ~24 nm.

In order to extend this imaging technique towards correlated imaging we adapted the sample preparation protocol and imaging procedure in such a way as to maximize the overall quality of the two images. Correlative AFM/SMLM measurments revealed a correlation between the height of the sample and the number of localizations recorded by dSTORM. The number of localizations in areas where a single filament was measured by AFM was lower than at other locations where AFM revealed that more than one filament is present. In such a case the differences reflect the amount of biomolecules present. On the other hand, in areas where a single filament is present, the local differences in localizations can be attributed to differences in labelling efficiency. Such a measurement approach could therefore be a tool to accurately determine the labelling efficiency by correlating the amount of biomolecules present to the number of localizations. (Figure 3.4).

As dSTORM imaging is not optimal for live cell imaging we performed PALM imaging on live samples. This didn’t require exchanging the buffer between AFM and PALM imaging such that experiments could be conducted in a buffer solution close to physiological conditions. Moreover, PALM doesn’t require to force the fluorophores into a dark state at the onset of the experiment

using high laser powers, thereby reducing phototoxic effects compared to dSTORM. A mammalian cell expressing a fluorescently tagged protein which forms part of the focal adhesion complex was imaged first by AFM and and then by PALM (Figure 3.5). Time-resolved AFM images were recorded every minute, showing the leading edge of the cell membrane extending. PALM images of the dynamics of the underlying focal adhesions were reconstructed with a similar temporal resolution. Correlated nanoscale imaging both with AFM and PALM showed the migration of the cell. Changes of the cell membrane were observed as well as the dynamic assembly and disassembly process of focal adhesions. These results demonstrate the potential of this technique in correlated structural and functional imaging of live cells at nanometer resolution.

7.1.3 Bacterial division of *M.smegmatis* is governed by mechanical forces

High-resolution imaging and nanomechanical characterization of *M.smegmatis* throughout entire cell cycles by AFM show remarkable insights into the cell division process. The first sign of division detectable by AFM is the feature described as the pre-separation furrow at midcell (Figure 4.1). As the cell progresses in its cell cycle this feature becomes more pronounced. After the outer cell envelope breaks apart and the bacteria separate, the new poles that have been formed before cell separation become visible. From the relatively slow AFM imaging rate (5 min/image) we saw no intermediate states of the separation, suggesting that this process is happening at shorter time scales. Moreover, scars were detected at the place where the outer cell envelop broke apart indicating that the separation of sibling cells could be due to a mechanical rupture of the cell envelop at the site of the septum. Constant measurements of the height at a rate of 1 kHz on the septum without lateral scanning indeed revealed that the separation of sibling cells is actually happening within tens of milliseconds.

Correlated AFM and FM imaging of the division process revealed a sequence of events in the progression of the cell cycle. The appearance of the pre-separation furrow at the surface of the bacterial cell envelop spatially and temporally correlates very closely with the coalescence of the FtsZ ring as well as the onset of septation at midcell (Figure 4.2). The septum is then being formed completely while the sibling cells still remain connected by the outer cell envelop. Just before separation the FtsZ ring disassembles. Then, after separation of the sibling cells, the newly formed septum becomes visible as the new poles.

Interestingly, during septation we observed an increased mechanical stiffness at the septum which disappeared after the separation of the sibling cells Nanomechanical measurements showed that the stiffness at the septum starts to increase as soon as the pre-separation furrow appears and the stiffness continues increasing as the cell progresses in its cell cycle (Figure 4.3). The stiffness increase then typically reaches a plateau and even slightly decreases just before the sibling cells separate. These results indicate that the timing of the separation of the sibling cells is influenced by the mechanical properties of the cell envelop connecting the sibling cells. Tension is built up at the septum which by AFM is apparent as increased stiffness. It is conceivable that the increase in stiffness is correlated to the formation of the septum and could possibly be a consequence thereof. In such a case, the increase in tension would be coupled to the progression in septation, preventing premature separation of the sibling cells. The observation of decreasing stiffness just prior to sibling cell separation could be due to hydrolytic activity of en-

zymes weakening the connection of the outer cell envelope specifically at the septum. This reduces the ultimate tensile strength, thus inducing the process of cell separation.

To test whether additional mechanical load could induce a premature cell separation I used the AFM to apply mechanical load on the septum. On average it took 70 minutes between the appearance of the pre-separation furrow and the separation of sibling cells. By pushing the cantilever down on the septum premature sibling cell separations could be induced already 25 minutes after the appearance of the pre-separation furrow. To apply mechanical load a FD curve was recorded on the septum. In the extending direction (Figure 4.4) a break can be observed as the mechanical load applied increases. In the following AFM image the sibling cells appeared completely separated. This result demonstrates that the separation of sibling cells can be induced prematurely by solely applying additional mechanical load on the septum. Whether bacteria survive this premature division depends on whether septation is finished. If the division is induced too early, the cell wall will be damaged. As a consequence, the bacteria lose their internal turgor pressure and die.

These results presented show how mechanical forces can influence the timing of cell separation. At the point where the tensile stress in the cell wall is higher than the ultimate tensile strength of the cell wall material, the bacterial cells separate. This separation can be induced prematurely by applying additional load Without the activity of hydrolytic enzymes specifically at the septum (potentially decreasing the ultimate tensile strength) the sibling cells do not separate(*49*). Therefore, these results suggests that the separation of sibling cells is dependent on hydrolytic enzymes and mechanical forces alike. The increase in tensile stress alone which might be in some form a consequence of the ongoing process of septation is not high enough as to induce the cell separation. This would ensure that the cells don't separate before septation is finished. On the other hand enzymes might be much more effective when hydrolysing chemical bonds under tension. Different reasons could be responsible for this. Firstly, chemical bonds might be more accessible. Secondly, each time a covalent bond under tension is hydrolysed the material opens up slightly revealing new bonds. Thirdly, as more bonds are hydrolysed the total tension is distributed over less bonds, overall increasing the tension on each bond reinforcing these effects even more.

7.1.4 Wave-troughs are sites where division will happen

The polar growing bacterium *M.smegmatis* exhibits wave-trough undulations on the surface. These features are ~1.8 µm in length with an amplitude of ~100 nm (Figure 5.1d) and are thus too small to detect by optical microscopes. Time lapse AFM imaging shows that the wave-troughs are established at the poles, the sites where growth happens in *M.smegmatis.* As the bacteria grow these wave-troughs move towards the center and become the preferred sites of division. Established wave-troughs often become division sites only one or two generations later as they are passed on to the daughter cells demonstrating that this is an inheritable morphological feature (Figure 5.2a). The positioning and formation of the FtsZ contractile ring is restricted to the central wave-trough. It is conceivable that the curvature at wave-troughs favors the positioning of the FtsZ ring at these sites while it is less favourable at wave-crests which are therefore chosen as division sites.

The formation of the wave-troughs is strongly associated with the growth of the bacterium. If cells are treated with antibiotics preventing cell growth no more new wave-troughs are formed and only already existant wave-troughs become division sites. On the other hand if cells are treated with an antibiotic preventing cell division but not cell growth new wave-troughs are still formed (Figure 5.1e). This suggests that growth is necessary for the establishment of new wave-troughs.

Experiments performed with a mutant strain indicate that the choice of which wave-trough becoms a division site seems to be dependent on the DNA distribution (Figure 5.4e). In a strain with a deletion of parB (*ΔparB*), a protein involved in proper segregation of chromosomes to each of the daughter cells before division, chromosome segregation is impaired. As a consequence, cells often divide at off-center positions where DNA density is lower. Correlated AFM/FM measurements showed that even in these cases division happens at wave-troughs further strengthening the link between these morphological features and the division site selection.

Combined AFM/FM measurements show the sequence of different events happening during cell division. 2-4 hours after a new cell is born FtsZ starts to coalesce at the center wave-trough. 30 minutes later the pre-separation furrow appears at the surface and 20 minutes later the cytokinesis marker wag31 marks the new poles. 40 minutes later cell separation occurs. (Figure 5.3)

These morphological features are the earliest detected characteristic correlated to division sites. Characterization of these features by combined AFM/FM showed their inheritable nature, establishment and progression and most importantly their link to cell division.

7.1.5 Chronic inflammation imposes aberrant cell fate in regenerating epithelia through mechanotransduction

This work describes the link between chronic inflammation and aberrant cell fate in regenerating epithelia. Stem cells at the limbus are activated upon injury on the cornea. A specific mouse model used in this study (Notch1 mutant) develops a chronic inflammation upon repeated injury of the cornea. This caused a change in cell fate of the activated stem cells from a corneal cell type to a skin-like cell type leading to turbidity of the cornea. Upon inhibiting the chronic inflammation the stem cells took on a normal corneal cell fate. This shows that the chronic inflammation or consequences thereof are the cause of this change in cell fate. On the other hand, an aberrant cell fate could be induced by overactivating mechanotransduction pathways even in the absence of a chronic inflammation, suggesting that the mechanotransduction pathway influences the cell fate downstream of the chronic inflammation. Fluorescent microscopy studies showed that extensive extra cellular matrix deposition occurred in the presence of a chronic inflammation. AFM measurements on tissue sections have been done to test the hypothesis whether this could lead to an increased stiffness of the tissue which could possibly overactivate mechanotransduction pathways thereby inducing the aberrant cell fate. Force-volume measurements with an AFM cantilever modified with a 20 µm diameter bead at the front combined with fluorescent microscopy imaging were performed. The results showed that the tissue exposed to chronic inflammation showed increased ECM deposition. These regions turned out to be significantly stiffer as measured by AFM. The highest increase in stiffness between the normal tissue and the tissue exposed to the chronic inflammation was measured at

the peripheral area and was ~ 3x higher. This is as well the area where the biggest difference in ECM deposition was observed compared to the wildtype control. The stiffness was as well significantly higher at the limbus and at the center but to a lower extent. The limbus being the site furthest away from the place of injury forms a stem cell niche. Since this is a place of constant cell division and cell migration it is not very surprising the tissue to be a bit softer there. At the center where the actual injury happened polymorphonuclear cells were found indicative of a chronic inflammation. These cells might not contribute to the stiffness of the tissue as much as structural proteins do. At the periphery however, only very few cells were present indicated by DAPI fluorescent images. The most contributing part to this tissue was ECM mainly composed of structural proteins, making this the region of highest change in stiffness. It is conceivable that since the stem cells from the limbus have to migrate through this region the underlying stiffness might induce the mechanotransduction pathways resulting in aberrant cell fate.

By AFM we could show in a quantitative way that besides increased activation of mechanotransduction pathways and deposition of ECM the stiffness is enhanced. This study could provide a mechanistic link between cell fate and chronic inflammation through mechanotransduction and potentially reveal new targets for treatment of diseases linked to chronic inflammation.

7.2 Future development

In this work the combination of AFM and fluorescence microscopy has mainly been done in a sequential way, meaning that either AFM data or fluorescence data was taken. A better integration of these imaging modalities could make measurements easier where a quick change of imaging modality is desired or where the manipulation of the sample by one instrument should be observed with the other instrument. Such as applying a force with the AFM tip while observing changes in the fluorescence. This could for example be useful for experiments where the mechanical deformation by the AFM tip leads to activation of a mechanosensitive protein, whose effect can then be measured by fluorescence. A better integration of software as well as hardware potentially solves this challenge. We have already started to synchronize the excitation of the fluorescent molecules by the laser and image recording by the camera to an AFM imaging mode where the AFM laser can be switched off intermittently. In order for the AFM to not have negative impact on the fluorescence molecule through bleaching the AFM laser reading out the position of the cantilever could be replaced by an IR laser which is less common to use for conventional fluorescent dyes.

Moreover, since AFM represents a 3 dimensional imaging modality, it would be very interesting to upgrade the fluorescence microscopy capabilities to imaging in 3 dimensions as well. Therefore, processes such as phagocytosis could be observed where for example pathogens could be tracked at the outside of the cell by AFM and then internally in a 3D pattern as well. Or cytoskeletal structures could be imaged in a 3 dimensions. This could potentially be achieved by adding a confocal module to the optical microscope. Mainly in thick tissue sections confocal imaging is of particular interest. With such a capability the stiffness measurments presented in Chapter 6 could be interpreted with more precise knowledge of the underlying composition of the tissue.

Considering the mechanical implications of the division mechanism of *M.smegmatis* it would be interesting to know how much the tensile strength has to be weakend for the separation of the

cells to happen. This could then be used to estimate the strength of the outer cell envelop. Moreover, where the tension exactly comes from could not be answered by these experiments. We could speculate that the tension is building up as more material gets pumped into the space between the septal walls, or the new poles already start to grow for a little bit in the septal region. As they are still connected at the outside this would increase the tension specifically in this region.

Curriculum Vitae

PASCAL DAMIAN ODERMATT

Born: 30th of April 1985 in Stans, Switzerland

Citizenship: Swiss

CONTACT INFORMATION

Telephone: +41 79 103 65 08

E-mail: pascal.odermatt@epfl.ch

Address: EPFL STI IBI-STI LBNI

BM3113

Station 17

CH-1015 Lausanne

EDUCATION

1998-2004 High School Kollegium St. Fidelis, Stans, Switzerland

2005-2008 BSc in Cell Biology, University of Berne, Switzerland

Thesis title: "*Involvment of SMG5, SMG6 and SMG7 in Exon Junction Complex independent NMD and the NMD suppressing influence of poly-A tail proximity in Exon Juction Complex enhanced NMD*", Institute of Cell Biology, University of Berne, Switzerland. Supervisor: Dr. Oliver Mühlemann

2008-2010 MSc in Biomedical Engineering, ETH Zurich, Switzerland

2010 Thesis title: "*Capsosomes: Liposome Anchoring, Enzymatic Reaction and Cargo Release*", CNST – Nanostructured Interfaces and Materials Group, University of Melbourne, Australia. Supervisor: Prof. Frank Caruso, Prof. Janos Vörös, Dr. Rona Chandrawati

2011-now PhD student at Laboratory of Bio- and Nanoinstrumentation (LBNI), Interfaculty Institute of Bioengineering (IBI), EPF Lausanne, Switzerland

EMPLOYMENT HISTORY

2004-2005 Civilian National Service, Switzerland

2007-2008 Part-time biology teacher, Kollegium St. Fidelis Stans, Switzerland

2010 Research assistant (Civilian Natinal Service), University of Lausanne

RESEARCH EXPERIENCE

École Polytechnique Fédérale de Lausanne, *Lausanne, Switzerland*

Live-cell quantitative imaging

Atomic Force Microsocopy imaging and nanomechanical characterization of biological samples (biomolecules, living mammalian cells, bacteria, tissues)

Fluorescence microscopy, single molecule localization microscopy (SMLM) imaging (PALM , dSTORM)

Correlated AFM and SMLM measurements

Preparation of biological samples

Cell culture

Surface functionalization

University of Melbourne, *Melbourne, Australia*

Quart crystal microbalance with Dissipation Monitoring (QCM-D) measurements

Capsosome assembly

Fluorescence spectrophotometry

University of Berne, *Berne, Switzerland*

Cell culture and Transfection

RNA isolation and quantitative real-time RT-PCR

Plamsid characterization

TEACHING EXPERIENCE

2012-2015 Teaching assistant “Advanced bioengineering methods laboratory” EPFL (Prof. Fantner)

2012 Assistant for iGEM Team EPFL (international genetically engineered machine competition)

2013 Internship Project Supervision

2013 Bachelor Project Supervision

AWARDS

2015 Finalist, Runner-up in "the 2015 'Future Leaders in Bioengineering' Award, EPFL

POSTERS

2013 Poster: "*Effects of Antimicrobial Peptides on Bacteria Measured with Combined High-Speed AFM / Fluorescence Microscope*", Global Challenges – Opportunities for Nanotechnology, San Servolo, Venice, Italy

2014 Poster: "*Correlative Atomic Force Microscopy and dSTORM for Biological Samples in Fluid*", IBI Day, Interfaculty Institute of Bioengineering, EPF Lausanne

2015 Poster: "*Correlated atomic force microscopy and single molecule localization microscopy*", 10th EBSA EBSA European Biophysics Congress, Dresden, Germany

ORAL PRESENTATIONS

2015 *"Correlated atomic force microscopy and single molecule localization microscopy"* 10th EBSA European Biophysics Congress, Dresden, Germany

2015 *"Correlated atomic force microscopy and single molecule localization microscopy"* Single Molecule Localization Microscopy Symposium, Bordeaux, France

2015 *"Living Matters: Imaging of Live Cells at Nanometer Spatial and Millisecond Temporal Resolution"*, Bioengineering Day, EPF Lausanne, Switzerland

PUBLICATIONS

"Noncovalent Liposome Linkage and Miniaturization of Capsosomes for Drug Deliver", L. Hosta-Rigau,* Rona Chandrawati,* Elli Saveriades, **Pascal D. Odermatt,** Almar Postma, Francesca Ercole, Kerry Breheney, Kim L. Wark, Brigitte Städler, and Frank Caruso, *Biomacromolecules*, **11**, 3548 (2010)

"Triggered Cargo Release by Encapsulated Enzymatic Catalysis in Capsosomes" Rona Chandrawati, **Pascal D. Odermatt**, Siow-Feng Chong, Andrew D. Price, Brigitte Städler, and Frank Caruso, *Nano letters, **11**,* 4958 (2011)

"High-frequency multimodal atomic force microscopy", Adrian P. Nievergelt, Jonathan D. Adams, **Pascal D. Odermatt**, and Georg E. Fantner, *Beilstein Journal of Nanotechnology,* **5**, 2459 (2014)

"High-Resolution Correlative Microscopy: Bridging the Gap between Single Molecule Localization Microscopy and Atomic Force Microscopy", **Pascal D. Odermatt**, Arun Shivanandan,* Hendrik Deschout,* Radek Jankele, Adrian P. Nievergelt, Lely Feletti, Michael W. Davidson, Aleksandra Radenovic, and Georg E. Fantner, *Nano letters,* **15**, 4896 (2015)

"Chronic inflammation imposes aberrant cell fate in regenerating epithelia through mechanotransduction", Craig S. Nowell, **Pascal D. Odermatt**, Luca Azzolin, Sylke Hohnel, Erwin F. Wag-

ner, Georg E. Fantner, Matthias P. Lutolf, Yann Barrandon, Stefano Piccolo, and Freddy Radtke, *Nature cell biology,* **advance online publication**, (2015)

*contributed equally

IN PREPARATION

"Bacterial division governed by mechanical properties", **Pascal D. Odermatt**, Haig A. Eskandarian, John D. McKinney, and Georg E. Fantner

"Inherited cell-surface wave-troughs mark future division sites in mycobacteria", Haig A. Eskandarian, **Pascal D. Odermatt**, Joëlle Ven, Adrian P. Nievergelt, Neeraj Dhar, John D. McKinney, and Georg E. Fantner

INTERESTS

Skiing, Hiking, Soccer, Cooking, Historical fiction

LANGUAGES

German (Native), English (Fluent), French, Spanish (Basic knowledge)

COMPUTER SKILLS

Gwyddion, Nanoscope Analysis, ImageJ, Matlab, Adobe Illustrator, Adobe Photoshop, OriginLab

Bibliography

1. G. Binnig, C. F. Quate, C. Gerber, Atomic Force Microscope. *Phys Rev Lett* **56**, 930 (1986).
2. E. Betzig *et al.*, Imaging intracellular fluorescent proteins at nanometer resolution. *Science* **313**, 1642 (Sep 15, 2006).
3. S. van de Linde *et al.*, Direct stochastic optical reconstruction microscopy with standard fluorescent probes. *Nature protocols* **6**, 991 (Jul, 2011).
4. E. Henderson, P. G. Haydon, D. S. Sakaguchi, Actin filament dynamics in living glial cells imaged by atomic force microscopy. *Science* **257**, 3 (1992).
5. Y. F. Dufrene, C. J. P. Boonaert, P. A. Gerin, M. Asther, P. G. Rouxhet, Direct Probing of the Surface Ultrastructure and Molecular Interactions of Dormant and Germinating Spores ofPhanerochaete chrysosporium. *Journal of Bacteriology* **181**, 5 (1999).
6. C. Rotsch, F. Braet, E. Wisse, M. Radmacher, AFM IMAGING AND ELASTICITY MEASUREMENTS ON LIVING RAT LIVER MACROPHAGES. *Cell Biology International* **21**, 685 (1997).
7. N. Kodera, D. Yamamoto, R. Ishikawa, T. Ando, Video imaging of walking myosin V by high-speed atomic force microscopy. *Nature* **468**, 72 (Nov 4, 2010).
8. T. Ando, High-speed atomic force microscopy coming of age. *Nanotechnology* **23**, 062001 (Feb 17, 2012).
9. S. T. Hess, T. P. Girirajan, M. D. Mason, Ultra-high resolution imaging by fluorescence photoactivation localization microscopy. *Biophys J* **91**, 4258 (Dec 1, 2006).
10. M. J. Rust, M. Bates, X. Zhuang, Sub-diffraction-limit imaging by stochastic optical reconstruction microscopy (STORM). *Nat Methods* **3**, 793 (Oct, 2006).
11. K. Xu, G. S. Zhong, X. W. Zhuang, Actin, Spectrin, and Associated Proteins Form a Periodic Cytoskeletal Structure in Axons. *Science* **339**, 452 (Jan 25, 2013).
12. A. Szymborska *et al.*, Nuclear Pore Scaffold Structure Analyzed by Super-Resolution Microscopy and Particle Averaging. *Science* **341**, 655 (Aug 9, 2013).
13. H. Shroff, C. G. Galbraith, J. A. Galbraith, E. Betzig, Live-cell photoactivated localization microscopy of nanoscale adhesion dynamics. *Nat Methods* **5**, 417 (May, 2008).
14. P. Annibale, S. Vanni, M. Scarselli, U. Rothlisberger, A. Radenovic, Quantitative Photo Activated Localization Microscopy: Unraveling the Effects of Photoblinking. *Plos One* **6**, (Jul 26, 2011).
15. P. Annibale, M. Scarselli, M. Greco, A. Radenovic, Identification of the factors affecting co-localization precision for quantitative multicolor localization microscopy. *Optical Nanoscopy* **1**, 9 (2012).
16. N. Durisic, L. Laparra-Cuervo, A. Sandoval-Alvarez, J. S. Borbely, M. Lakadamyali, Single-molecule evaluation of fluorescent protein photoactivation efficiency using an in vivo nanotemplate. *Nat Methods* **11**, 156 (Feb, 2014).
17. R. P. Nieuwenhuizen *et al.*, Measuring image resolution in optical nanoscopy. *Nat Methods* **10**, 557 (Jun, 2013).
18. Y. W. Chang *et al.*, Correlated cryogenic photoactivated localization microscopy and cryo-electron tomography. *Nat Methods* **11**, 737 (Jul, 2014).
19. B. G. Kopek, G. Shtengel, J. B. Grimm, D. A. Clayton, H. F. Hess, Correlative Photoactivated Localization and Scanning Electron Microscopy. *Plos One* **8**, (Oct 25, 2013).
20. A. Monserrate, S. Casado, C. Flors, Correlative atomic force microscopy and localization-based super-resolution microscopy: revealing labelling and image reconstruction artefacts. *Chemphyschem* **15**, 647 (Mar 17, 2014).
21. D. J. Muller, F. A. Schabert, G. Buldt, A. Engel, Imaging purple membranes in aqueous solutions at sub-nanometer resolution by atomic force microscopy. *Biophys J* **68**, 1681 (May, 1995).

22. J. V. Chacko, F. C. Zanacchi, A. Diaspro, Probing cytoskeletal structures by coupling optical superresolution and AFM techniques for a correlative approach. *Cytoskeleton* **70**, 729 (Nov, 2013).
23. M. Heilemann *et al.*, Subdiffraction-resolution fluorescence imaging with conventional fluorescent probes. *Angew Chem Int Edit* **47**, 6172 (2008).
24. S. Schmitz *et al.*, Malaria parasite actin polymerization and filament structure. *J Biol Chem* **285**, 36577 (Nov 19, 2010).
25. D. J. Metcalf, R. Edwards, N. Kumarswami, A. E. Knight, Test samples for optimizing STORM super-resolution microscopy. *J Vis Exp*, (2013).
26. K. Xu, H. P. Babcock, X. W. Zhuang, Dual-objective STORM reveals three-dimensional filament organization in the actin cytoskeleton. *Nat Methods* **9**, 185 (Feb, 2012).
27. R. Dominguez, K. C. Holmes, Actin structure and function. *Annu Rev Biophys* **40**, 169 (2011).
28. G. T. Dempsey, J. C. Vaughan, K. H. Chen, M. Bates, X. W. Zhuang, Evaluation of fluorophores for optimal performance in localization-based super-resolution imaging. *Nat Methods* **8**, 1027 (Dec, 2011).
29. T. Ikawa *et al.*, Molecular scale imaging of F-actin assemblies immobilized on a photopolymer surface. *Phys Rev Lett* **98**, (Jan 5, 2007).
30. A. G. York, A. Ghitani, A. Vaziri, M. W. Davidson, H. Shroff, Confined activation and subdiffractive localization enables whole-cell PALM with genetically expressed probes. *Nat Meth* **8**, 327 (04//print, 2011).
31. B. Huang, W. Q. Wang, M. Bates, X. W. Zhuang, Three-dimensional super-resolution imaging by stochastic optical reconstruction microscopy. *Science* **319**, 810 (Feb 8, 2008).
32. S. R. P. Pavani *et al.*, Three-dimensional, single-molecule fluorescence imaging beyond the diffraction limit by using a double-helix point spread function. *P Natl Acad Sci USA* **106**, 2995 (Mar 3, 2009).
33. G. Shtengel *et al.*, Interferometric fluorescent super-resolution microscopy resolves 3D cellular ultrastructure. *Proc Natl Acad Sci U S A* **106**, 3125 (Mar 3, 2009).
34. S. Abrahamsson *et al.*, Fast multicolor 3D imaging using aberration-corrected multifocus microscopy. *Nat Methods* **10**, 60 (Jan, 2013).
35. C. Rotsch, K. Jacobson, M. Radmacher, Dimensional and mechanical dynamics of active and stable edges in motile fibroblasts investigated by using atomic force microscopy. *P Natl Acad Sci USA* **96**, 921 (Feb 2, 1999).
36. A. Colom, I. Casuso, F. Rico, S. Scheuring, A hybrid high-speed atomic force–optical microscope for visualizing single membrane proteins on eukaryotic cells. *Nat Commun* **4**, (07/16/online, 2013).
37. Y. F. Dufrene, D. Martinez-Martin, I. Medalsy, D. Alsteens, D. J. Muller, Multiparametric imaging of biological systems by force-distance curve-based AFM. *Nat Methods* **10**, 847 (Sep, 2013).
38. S. H. Shim *et al.*, Super-resolution fluorescence imaging of organelles in live cells with photoswitchable membrane probes. *P Natl Acad Sci USA* **109**, 13978 (Aug 28, 2012).
39. S. A. Jones, S.-H. Shim, J. He, X. Zhuang, Fast, three-dimensional super-resolution imaging of live cells. *Nat Meth* **8**, 499 (06//print, 2011).
40. A. Slade, S. C. Minne, Time-Resolved Nanometer Scale AFM Imaging of Antimicrobial Peptide Activity on Live Escherichia coli Cells. *Microscopy and Microanalysis* **20**, 2074 (2014).
41. D. E. Ingber, Cellular mechanotransduction: putting all the pieces together again. *Faseb J* **20**, 811 (May, 2006).
42. Y. X. Wang, J. Y. J. Shyy, S. Chien, Fluorescence proteins, live-cell imaging, and mechanobiology: Seeing is believing. *Annu Rev Biomed Eng* **10**, 1 (2008).
43. U. Endesfelder *et al.*, Multiscale Spatial Organization of RNA Polymerase in *Escherichia coli*. *Biophys J* **105**, 10 (2013).
44. N. Olivier, D. Keller, P. Gonczy, S. Manley, Resolution Doubling in 3D-STORM Imaging through Improved Buffers. *Plos One* **8**, (Jul 17, 2013).
45. K. I. Mortensen, L. S. Churchman, J. A. Spudich, H. Flyvbjerg, Optimized localization analysis for single-molecule tracking and super-resolution microscopy. *Nat Methods* **7**, 377 (May, 2010).
46. J. R. Janesick, in *pie Press Monograph*. (SPIE Publications, Bellingham, WA, 2007).

47. M. Ovesny, P. Krizek, J. Borkovec, Z. K. Svindrych, G. M. Hagen, ThunderSTORM: a comprehensive ImageJ plug-in for PALM and STORM data analysis and super-resolution imaging. *Bioinformatics* **30**, 2389 (Aug 15, 2014).
48. X. Zhou *et al.*, Mechanical crack propagation drives millisecond daughter cell separation in Staphylococcus aureus. *Science* **348**, 574 (2015).
49. E. C. Hett, M. C. Chao, L. L. Deng, E. J. Rubin, A Mycobacterial Enzyme Essential for Cell Division Synergizes with Resuscitation-Promoting Factor. *PLoS Pathog* **4**, (2008).
50. J. M. Monteiro *et al.*, Cell shape dynamics during the staphylococcal cell cycle. *Nature Communications* **6**, (2015).
51. N. R. Thanky, D. B. Young, B. D. Robertson, Unusual features of the cell cycle in mycobacteria: Polar-restricted growth and the snapping-model of cell division. *Tuberculosis* **87**, 231 (5//, 2007).
52. A. Takade, K. Takeya, H. Taniguchi, Y. Mizuguchi, Electron Microscopic Observations of Cell Division in Mycobacterium vaccae V1. *Microbiology* **129**, 2315 (1983).
53. J. L. Dahl, Electron microscopy analysis of Mycobacterium tuberculosis cell division. *FEMS Microbiology Letters* **240**, 15 (2004).
54. I. Santi, N. Dhar, D. Bousbaine, Y. Wakamoto, J. D. McKinney, Single-cell dynamics of the chromosome replication and cell division cycles in mycobacteria. *Nature Communications* **4**, (2013).
55. E. C. Hett, E. J. Rubin, Bacterial Growth and Cell Division: a Mycobacterial Perspective. *Microbiology and Molecular Biology Reviews* **72**, 126 (2008).
56. S. Vijay, D. Anand, P. Ajitkumar, Unveiling unusual features of formation of septal partition and constriction in mycobacteria - an ultrastructural study. *Journal of Bacteriology* **194**, 702 (2011).
57. R. P. Edwards, ELECTRON-MICROSCOPE ILLUSTRATIONS OF DIVISION IN *MYCOBACTERIUM LEPRAE*. *J. Med. Microbiol.* **3**, 493 (1970).
58. S. F. Conti, M. E. Gettner, ELECTRON MICROSCOPY OF CELLULAR DIVISION IN ESCHERICHIA COLI. *J Bacteriol* **83**, 544 (Mar, 1962).
59. V. Dupres *et al.*, Nanoscale mapping and functional analysis of individual adhesins on living bacteria. *Nat Meth* **2**, 515 (07//print, 2005).
60. P. D. Odermatt *et al.*, High-Resolution Correlative Microscopy: Bridging the Gap between Single Molecule Localization Microscopy and Atomic Force Microscopy. *Nano letters* **15**, 4896 (Aug 12, 2015).
61. K. J. Kieser, E. J. Rubin, How sisters grow apart: mycobacterial growth and division. *Nature Reviews Microbiology* **12**, 550 (2014).
62. A. H. Eskandarian *et al.*, Inherited cell-surface wave-troughs mark future division sites in mycobacteria. *Nature*, (2016).
63. C. Jani *et al.*, Regulation of Polar Peptidoglycan Biosynthesis by Wag31 Phosphorylation in Mycobacteria. *BMC Microbiology* **10**, 327 (2010).
64. C.-M. Kang, S. Nyayapathy, J.-Y. Lee, J.-W. Suh, R. N. Husson, Wag31, a homologue of the cell division protein DivIVA, regulates growth, morphology and polar cell wall synthesis in mycobacteria. *Microbiology* **154**, 725 (2008).
65. C. Carel *et al.*, <italic>Mycobacterium tuberculosis</italic> Proteins Involved in Mycolic Acid Synthesis and Transport Localize Dynamically to the Old Growing Pole and Septum. *Plos One* **9**, e97148 (2014).
66. C. Hoffmann, A. Leis, M. Niederweis, J. M. Plitzko, H. Engelhardt, Disclosure of the mycobacterial outer membrane: Cryo-electron tomography and vitreous sections reveal the lipid bilayer structure. *Proceedings of the National Academy of Sciences* **105**, 3963 (2008).
67. B. Zuber *et al.*, Direct Visualization of the Outer Membrane of Mycobacteria and Corynebacteria in Their Native State. *Journal of Bacteriology* **190**, 5672 (2008).
68. X. Meniche *et al.*, Subpolar addition of new cell wall is directed by DivIVA in mycobacteria. *P Natl Acad Sci USA* **111**, E3243 (07/21, 2014).
69. W. Zhang, G. Ferguson, S. Tatic-Lucic, in *Micro Electro Mechanical Systems, 2004. 17th IEEE International Conference on.(MEMS)*. (IEEE, 2004), pp. 741-744.
70. L. G. Monahan, A. T. Liew, A. L. Bottomley, E. J. Harry, Division site positioning in bacteria: one size does not fit all. *Frontiers in microbiology* **5**, (2014).

71. G. E. Fantner, R. J. Barbero, D. S. Gray, A. M. Belcher, Kinetics of antimicrobial peptide activity measured on individual bacterial cells using high-speed atomic force microscopy. *Nat Nanotechnol* **5**, 280 (Apr, 2010).
72. Y. F. Dufrêne, Towards nanomicrobiology using atomic force microscopy. *Nature Reviews Microbiology* **6**, 674 (2008).
73. J. Männik, M. W. Bailey, Spatial coordination between chromosomes and cell division proteins in Escherichia coli. *Frontiers in microbiology* **6**, (2015).
74. Y. Wu, R. C. Sims, A. Zhou, AFM resolves effects of ethambutol on nanomechanics and nanostructures of single dividing mycobacteria in real-time. *Physical Chemistry Chemical Physics* **16**, 19156 (2014).
75. D. Trojanowski *et al.*, Choreography of the Mycobacterium Replication Machinery during the Cell Cycle. *mBio* **6**, e02125 (2015).
76. I. Santi, J. D. McKinney, Chromosome Organization and Replisome Dynamics in Mycobacterium smegmatis. *Mbio* **6**, e01999 (2015).
77. Y. F. Dufrêne, Atomic force microscopy in microbiology: new structural and functional insights into the microbial cell surface. *MBio* **5**, e01363 (2014).
78. A. Touhami, M. H. Jericho, T. J. Beveridge, Atomic force microscopy of cell growth and division in Staphylococcus aureus. *Journal of bacteriology* **186**, 3286 (2004).
79. Z. Li, M. J. Trimble, Y. V. Brun, G. J. Jensen, The structure of FtsZ filaments in vivo suggests a force-generating role in cell division. *The EMBO journal* **26**, 4694 (2007).
80. A. Möll, S. Schlimpert, A. Briegel, G. J. Jensen, M. Thanbichler, DipM, a new factor required for peptidoglycan remodelling during cell division in Caulobacter crescentus. *Molecular microbiology* **77**, 90 (2010).
81. A. Fleurie *et al.*, MapZ marks the division sites and positions FtsZ rings in Streptococcus pneumoniae. *Nature* **516**, 259 (Dec 11, 2014).
82. J. Lutkenhaus, S. Pichoff, S. Du, Bacterial cytokinesis: from Z ring to divisome. *Cytoskeleton* **69**, 778 (2012).
83. K. C. Huang, K. S. Ramamurthi, Macromolecules that prefer their membranes curvy. *Molecular microbiology* **76**, 822 (2010).
84. G. Laloux, C. Jacobs-Wagner, How do bacteria localize proteins to the cell pole? *J Cell Sci* **127**, 11 (2014).
85. K. S. Ramamurthi, S. Lecuyer, H. A. Stone, R. Losick, Geometric cue for protein localization in a bacterium. *Science* **323**, 1354 (2009).
86. T. G. Bernhardt, P. A. De Boer, SlmA, a nucleoid-associated, FtsZ binding protein required for blocking septal ring assembly over chromosomes in E. coli. *Molecular cell* **18**, 555 (2005).
87. B. Singh *et al.*, Asymmetric growth and division in Mycobacterium spp.: compensatory mechanisms for non-medial septa. *Molecular microbiology* **88**, 64 (2013).
88. Q. Sun, W. Margolin, Effects of perturbing nucleoid structure on nucleoid occlusion-mediated toporegulation of FtsZ ring assembly. *Journal of bacteriology* **186**, 3951 (2004).
89. Y. Wakamoto *et al.*, Dynamic persistence of antibiotic-stressed mycobacteria. *Science* **339**, 91 (2013).
90. B. W. Erickson, S. Coquoz, J. D. Adams, D. J. Burns, G. E. Fantner, Large-scale analysis of high-speed atomic force microscopy data sets using adaptive image processing. *Beilstein journal of nanotechnology* **3**, 747 (2012).
91. E. N. Arwert, E. Hoste, F. M. Watt, Epithelial stem cells, wound healing and cancer. *Nat Rev Cancer* **12**, 170 (03//print, 2012).
92. S. I. Grivennikov, F. R. Greten, M. Karin, Immunity, Inflammation, and Cancer. *Cell* **140**, 883 (3/19/, 2010).
93. M. Herfs, P. Hubert, P. Delvenne, Epithelial metaplasia: adult stem cell reprogramming and (pre)neoplastic transformation mediated by inflammation? *Trends in Molecular Medicine* **15**, 245 (6//, 2009).
94. M. Karin, Nuclear factor-[kappa]B in cancer development and progression. *Nature* **441**, 431 (05/25/print, 2006).
95. S. Tu *et al.*, Overexpression of Interleukin-1β Induces Gastric Inflammation and Cancer and Mobilizes Myeloid-Derived Suppressor Cells in Mice. *Cancer Cell* **14**, 408 (11/4/, 2008).

96. S. Wu *et al.*, A human colonic commensal promotes colon tumorigenesis via activation of T helper type 17 T cell responses. *Nat Med* **15**, 1016 (09//print, 2009).
97. M. Quante *et al.*, Bile Acid and Inflammation Activate Gastric Cardia Stem Cells in a Mouse Model of Barrett-Like Metaplasia. *Cancer Cell* **21**, 36 (1/17/, 2012).
98. N. Barker *et al.*, Crypt stem cells as the cells-of-origin of intestinal cancer. *Nature* **457**, 608 (01/29/print, 2009).
99. G. Driessens, B. Beck, A. Caauwe, B. D. Simons, C. Blanpain, Defining the mode of tumour growth by clonal analysis. *Nature* **488**, 527 (08/23/print, 2012).
100. A. K. Shenoy *et al.*, Transition from Colitis to Cancer: High Wnt Activity Sustains the Tumor-Initiating Potential of Colon Cancer Stem Cell Precursors. *Cancer Research* **72**, 5091 (October 1, 2012, 2012).
101. L. Boulter *et al.*, Macrophage-derived Wnt opposes Notch signaling to specify hepatic progenitor cell fate in chronic liver disease. *Nat Med* **18**, 572 (04//print, 2012).
102. K. Taniguchi *et al.*, A gp130-Src-YAP module links inflammation to epithelial regeneration. *Nature* **519**, 57 (03/05/print, 2015).
103. M. Di Piazza, Craig S. Nowell, U. Koch, A.-D. Durham, F. Radtke, Loss of Cutaneous TSLP-Dependent Immune Responses Skews the Balance of Inflammation from Tumor Protective to Tumor Promoting. *Cancer Cell* **22**, 479 (10/16/, 2012).
104. M. Aragona *et al.*, A Mechanical Checkpoint Controls Multicellular Growth through YAP/TAZ Regulation by Actin-Processing Factors. *Cell* **154**, 1047 (8/29/, 2013).
105. M. S. Samuel, M. F. Olson, Actomyosin contractililty: Force power drives tumor growth. *Cell Cycle* **10**, 3409 (2011/10/15, 2011).
106. J. D. Humphrey, E. R. Dufresne, M. A. Schwartz, Mechanotransduction and extracellular matrix homeostasis. *Nature reviews. Molecular cell biology* **15**, 802 (Dec, 2014).
107. M. J. Paszek *et al.*, Tensional homeostasis and the malignant phenotype. *Cancer Cell* **8**, 241 (9//, 2005).
108. K. R. Levental *et al.*, Matrix Crosslinking Forces Tumor Progression by Enhancing Integrin Signaling. *Cell* **139**, 891 (11/25/, 2009).
109. C. Bonnans, J. Chou, Z. Werb, Remodelling the extracellular matrix in development and disease. *Nature reviews. Molecular cell biology* **15**, 786 (12//print, 2014).
110. T. McHedlidze *et al.*, Interleukin-33-Dependent Innate Lymphoid Cells Mediate Hepatic Fibrosis. *Immunity* **39**, 357 (8/22/, 2013).
111. S. S. Aceves, S. J. Ackerman, Relationships Between Eosinophilic Inflammation, Tissue Remodeling, and Fibrosis in Eosinophilic Esophagitis. *Immunology and Allergy Clinics of North America* **29**, 197 (2//, 2009).
112. Z. Zhu *et al.*, Pulmonary expression of interleukin-13 causes inflammation, mucus hypersecretion, subepithelial fibrosis, physiologic abnormalities, and eotaxin production. *The Journal of Clinical Investigation* **103**, 779 (1999).
113. J. T. Daniels, J. K. G. Dart, S. J. Tuft, P. T. Khaw, Corneal stem cells in review. *Wound Repair and Regeneration* **9**, 483 (2001).
114. J. T. Daniels *et al.*, Limbal epithelial stem cell therapy. *Expert Opinion on Biological Therapy* **7**, 1 (2007/01/01, 2007).
115. F. Majo, A. Rochat, M. Nicolas, G. A. Jaoude, Y. Barrandon, Oligopotent stem cells are distributed throughout the mammalian ocular surface. *Nature* **456**, 250 (11/13/print, 2008).
116. L. Liang, H. Sheha, J. Li, S. C. G. Tseng, Limbal stem cell transplantation: new progresses and challenges. *Eye* **23**, 1946 (12/19/online, 2008).
117. C. M. Samson, C. Nduaguba, S. Baltatzis, C. S. Foster, Limbal stem cell transplantation in chronic inflammatory eye disease. *Ophthalmology* **109**, 862 (5//, 2002).
118. N. A. McNamara, M. Gallup, T. C. Porco, Establishing PAX6 as a Biomarker to Detect Early Loss of Ocular Phenotype in Human Patients With Sjögren's SyndromePAX6 as a Biomarker in Sjögren's Syndrome. *Investigative Ophthalmology & Visual Science* **55**, 7079 (2014).
119. Y.-T. Chen *et al.*, Immune profile of squamous metaplasia development in autoimmune regulator-deficient dry eye. *Molecular Vision* **15**, 563 (2009).

120. Y.-T. Chen *et al.*, Interleukin-1 receptor mediates the interplay between CD4+ T cells and ocular resident cells to promote keratinizing squamous metaplasia in Sjogren's syndrome. *Lab Invest* **92**, 556 (04//print, 2012).
121. S. Vauclair *et al.*, Corneal Epithelial Cell Fate Is Maintained during Repair by Notch1 Signaling via the Regulation of Vitamin A Metabolism. *Developmental Cell* **13**, 242 (8/7/, 2007).
122. S. Demehri *et al.*, Notch-Deficient Skin Induces a Lethal Systemic B-Lymphoproliferative Disorder by Secreting TSLP, a Sentinel for Epidermal Integrity. *PLoS Biol* **6**, e123 (2008).
123. A. Dumortier *et al.*, Atopic Dermatitis-Like Disease and Associated Lethal Myeloproliferative Disorder Arise from Loss of Notch Signaling in the Murine Skin. *Plos One* **5**, e9258 (2010).
124. J. Guinea-Viniegra *et al.*, Differentiation-induced skin cancer suppression by FOS, p53, and TACE/ADAM17. *The Journal of Clinical Investigation* **122**, 2898 (2012).
125. A. Murthy *et al.*, Notch Activation by the Metalloproteinase ADAM17 Regulates Myeloproliferation and Atopic Barrier Immunity by Suppressing Epithelial Cytokine Synthesis. *Immunity* **36**, 105 (1/27/, 2012).
126. H. B. Schonthaler, J. Guinea-Viniegra, E. F. Wagner, Targeting inflammation by modulating the Jun/AP-1 pathway. *Annals of the Rheumatic Diseases* **70**, i109 (March 1, 2011, 2011).
127. R. L. Eckert *et al.*, AP1 transcription factors in epidermal differentiation and skin cancer. *Journal of skin cancer* **2013**, (2013).
128. S. Wurm *et al.*, Terminal epidermal differentiation is regulated by the interaction of Fra-2/AP-1 with Ezh2 and ERK1/2. *Genes & development* **29**, 144 (2015).
129. S. Chappaz, L. Flueck, A. G. Farr, A. G. Rolink, D. Finke, Increased TSLP availability restores T-and B-cell compartments in adult IL-7–deficient mice. *Blood* **110**, 3862 (2007).
130. M. Omori-Miyake, S. F. Ziegler, Mouse models of allergic diseases: TSLP and its functional roles. *Allergology International* **61**, 27 (2012).
131. M. Kuraguchi *et al.*, Adenomatous polyposis coli (APC) is required for normal development of skin and thymus. *PLoS Genet* **2**, e146 (2006).
132. K. Miyoshi *et al.*, Activation of β-catenin signaling in differentiated mammary secretory cells induces transdifferentiation into epidermis and squamous metaplasias. *Proceedings of the National Academy of Sciences* **99**, 219 (2002).
133. M. Mukhopadhyay *et al.*, Dkk2 plays an essential role in the corneal fate of the ocular surface epithelium. *Development* **133**, 2149 (2006).
134. N. Harada *et al.*, Intestinal polyposis in mice with a dominant stable mutation of the β-catenin gene. *The EMBO journal* **18**, 5931 (1999).
135. S. Dupont *et al.*, Role of YAP/TAZ in mechanotransduction. *Nature* **474**, 179 (2011).
136. L. Azzolin *et al.*, YAP/TAZ incorporation in the β-catenin destruction complex orchestrates the Wnt response. *Cell* **158**, 157 (2014).
137. J. P. Iredale, Models of liver fibrosis: exploring the dynamic nature of inflammation and repair in a solid organ. *Journal of Clinical Investigation* **117**, 539 (2007).
138. W. A. Carey, G. D. Taylor, W. B. Dean, J. D. Bristow, Tenascin-C deficiency attenuates TGF-β-mediated fibrosis following murine lung injury. *American Journal of Physiology-Lung Cellular and Molecular Physiology* **299**, L785 (2010).
139. P. K. Naik *et al.*, Periostin promotes fibrosis and predicts progression in patients with idiopathic pulmonary fibrosis. *American Journal of Physiology-Lung Cellular and Molecular Physiology* **303**, L1046 (2012).
140. I. C. Lawrance *et al.*, Cellular and molecular mediators of intestinal fibrosis. *J Crohns Colitis*, (2014).
141. E. Sziksz *et al.*, Fibrosis related inflammatory mediators: role of the IL-10 cytokine family. *Mediators of inflammation* **2015**, (2015).
142. M. C. Kullberg *et al.*, TGF-β1 production by CD4+ CD25+ regulatory T cells is not essential for suppression of intestinal inflammation. *European journal of immunology* **35**, 2886 (2005).
143. N. Kenyon, R. Ward, G. McGrew, J. A. Last, TGF-β1 causes airway fibrosis and increased collagen I and III mRNA in mice. *Thorax* **58**, 772 (2003).
144. B. Wang *et al.*, Suppression of microRNA-29 expression by TGF-β1 promotes collagen expression and renal fibrosis. *Journal of the American Society of Nephrology* **23**, 252 (2012).
145. P. C. Fulkerson, C. A. Fischetti, M. E. Rothenberg, Eosinophils and CCR3 regulate interleukin-13 transgene-induced pulmonary remodeling. *The American journal of pathology* **169**, 2117 (2006).

146. B. Eyden, The myofibroblast: phenotypic characterization as a prerequisite to understanding its functions in translational medicine. *Journal of cellular and molecular medicine* **12**, 22 (2008).
147. O. De Wever, P. Demetter, M. Mareel, M. Bracke, Stromal myofibroblasts are drivers of invasive cancer growth. *International journal of cancer* **123**, 2229 (2008).
148. S.-L. Lin, T. Kisseleva, D. A. Brenner, J. S. Duffield, Pericytes and perivascular fibroblasts are the primary source of collagen-producing cells in obstructive fibrosis of the kidney. *The American journal of pathology* **173**, 1617 (2008).
149. J. Huelsken, R. Vogel, B. Erdmann, G. Cotsarelis, W. Birchmeier, β-Catenin controls hair follicle morphogenesis and stem cell differentiation in the skin. *Cell* **105**, 533 (2001).
150. A. K. Indra *et al.*, Temporally-controlled site-specific mutagenesis in the basal layer of the epidermis: comparison of the recombinase activity of the tamoxifen-inducible Cre-ERT and Cre-ERT2 recombinases. *Nucleic acids research* **27**, 4324 (1999).
151. F. Radtke *et al.*, Deficient T cell fate specification in mice with an induced inactivation of Notch1. *Immunity* **10**, 547 (1999).
152. A. Behrens *et al.*, Impaired postnatal hepatocyte proliferation and liver regeneration in mice lacking c-jun in the liver. *The EMBO journal* **21**, 1782 (2002).
153. H. Oshima, A. Rochat, C. Kedzia, K. Kobayashi, Y. Barrandon, Morphogenesis and renewal of hair follicles from adult multipotent stem cells. *Cell* **104**, 233 (2001).
154. J. L. Hutter, J. Bechhoefer, Calibration of atomic-force microscope tips. *Review of Scientific Instruments* **64**, 1868 (1993).
155. H. Hertz, Ueber die Beruehrung fester elastischer Koerper. *Journal fuer die reine und angewandte Mathematik* **92**, 156 (1881).